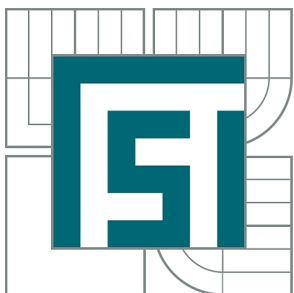


VYSOKÉ UČENÍ TECHNICKÉ V BRNĚ

BRNO UNIVERSITY OF TECHNOLOGY



FAKULTA STROJNÍHO INŽENÝRSTVÍ  
ÚSTAV FYZIKÁLNÍHO INŽENÝRSTVÍ

FACULTY OF MECHANICAL ENGINEERING  
INSTITUTE OF PHYSICAL ENGINEERING

# GRAFENOVÝ FOTODETEKTOR VYUŽÍVAJÍCÍ PLAZMONICKÝCH EFEKTŮ

GRAPHENE PHOTODETECTOR BASED ON PLASMONIC EFFECTS

DIPLOMOVÁ PRÁCE

MASTER'S THESIS

AUTOR PRÁCE

AUTHOR

Bc. MATĚJ HORÁČEK

VEDOUCÍ PRÁCE

SUPERVISOR

prof. RNDr. TOMÁŠ ŠIKOLA, CSc.

BRNO 2015



Vysoké učení technické v Brně, Fakulta strojního inženýrství

Ústav fyzikálního inženýrství

Akademický rok: 2014/2015

## **ZADÁNÍ DIPLOMOVÉ PRÁCE**

student(ka): Bc. Matěj Horáček

který/která studuje v **magisterském navazujícím studijním programu**

obor: **Fyzikální inženýrství a nanotechnologie (3901T043)**

Ředitel ústavu Vám v souladu se zákonem č.111/1998 o vysokých školách a se Studijním a zkušebním řádem VUT v Brně určuje následující téma diplomové práce:

### **Grafenový fotodetektor využívající plazmonických efektů**

v anglickém jazyce:

### **Graphene photodetector based on plasmonic effects**

Stručná charakteristika problematiky úkolu:

Grafen a plazmonika jsou jedny z nejintenzivněji studovaných oborů současné fyziky, například kvůli jejich možnému uplatnění v oblasti fotovoltiky, fotoelektroniky či biodetekce. Úkolem studenta bude použití právě kombinace grafenu a plazmonických nanostruktur pro vytvoření fotodetektoru. V tomto zařízení bude grafenu použito jako fotoaktivní vrstvy a plazmonické nanostruktury (konkrétně zlaté nanotyčinky) budou sloužit ke zvýšení účinnosti vytvořeného fotodetektoru. Dále bude provedena detailní studie interakce elektromagnetického záření se systémem grafen – zlatá nanotyčinka, konkrétně bude sledováno chování optického absorpčního píku systému.

Cíle diplomové práce:

1. Provedení rešeršní studie.
2. Popis interakce elektromagnetického záření s grafenem a plazmonickými nanostrukturami.
3. Studie chování plazmonických struktur na grafenovém substrátu.
4. Příprava a charakterizace grafenového fotodetektoru s užitím plazmonických nanostruktur.

## ABSTRACT

Two rich and vibrant fields of investigation - graphene and plasmonics - strongly overlap in this work, giving rise to a novel hybrid photodetection device. The intrinsic photoresponse of graphene is significantly enhanced by placing the gold nanorods exhibiting unique anisotropic localized surface plasmon resonances on the graphene surface. The reported enhanced photoresponse of graphene is caused by the redistribution of localized surface plasmons in the nanoparticles into graphene. The exact underlying energy redistribution mechanism is thoroughly studied by a single particle scattering spectroscopy monitoring the particle plasmon linewidth as a function of the number of underlying graphene layers. The obtained extraordinary plasmon broadening for nanoparticles placed on graphene suggests the contribution of a novel energy redistribution channel attributed to the injection of hot electrons from gold nanorods into graphene.

## KEYWORDS

graphene, plasmonics, photodetection, LSPR, plasmon damping, gold nanorod, hot electrons, single particle scattering spectroscopy

## ABSTRAKT

Tato práce se zabývá vývojem nového hybridního zařízení pro fotodetekci, jehož princip se opírá o dvě velmi významné a aktuální oblasti současného vědeckého výzkumu – grafen a plazmonika. Vlastní odezva grafenu na dopadající světelné záření je v tomto zařízení značně zvýšena umístěním zlatých nanotyčinek na povrch grafenu, vykazujících jedinečnou optickou odezvu danou lokalizovanými povrchovými plazmony. Tato zvýšená fotoelektrická reakce je způsobena redistribucí energie oscilujících elektronů v nanočástici do grafenové vrstvy. Konkrétní mechanismus redistribuce energie je studován pomocí rozptylové spektroskopie jednotlivých částic, kde je zkoumán vliv počtu grafenových vrstev pod nanočásticí na rozšíření rezonančního píku. Mimořádně velké rozšíření rezonančního píku pro částice položené na grafen naznačuje přítomnost nebývalého procesu tlumení plazmonické rezonance. Toto neobvyklé tlumení je připsáno přenosu horkých elektronů ze zlaté nanotyčinky do grafenové vrstvy.

## KLÍČOVÁ SLOVA

grafen, plazmonika, fotodetekce, LSPR, tlumení plazmonu, zlaté nanotyčinky, horké elektrony, rozptylová spektroskopie jednotlivých částic

HORÁČEK, Matěj *Graphene photodetector based on plasmonic effects*: master's thesis. Brno: Brno University of Technology, Faculty of Mechanical Engineering, Ústav fyzikálního inženýrství, 2015. 96 p. Supervised by prof. RNDr. Tomáš Šíkola, CSc.

## DECLARATION

I declare that I have elaborated my master's thesis on the theme of "Graphene photodetector based on plasmonic effects" independently, under the supervision of the master's thesis supervisor and with the use of technical literature and other sources of information which are all quoted in the thesis and detailed in the list of literature at the end of the thesis.

As the author of the master's thesis I furthermore declare that, concerning the creation of this master's thesis, I have not infringed any copyright. In particular, I have not unlawfully encroached on anyone's personal copyright and I am fully aware of the consequences in the case of breaking Regulation § 11 and the following of the Copyright Act No 121/2000 Vol., including the possible consequences of criminal law resulted from Regulation § 152 of Criminal Act No 140/1961 Vol.

Brno .....

.....

(author's signature)

## Acknowledgment

I would like to thank my supervisor **prof. Tomáš Šikola** for his inspiring comments, proofreading of this thesis and the opportunity to study abroad he gave me. My thank also belongs to **dr.ir. Cees F.J. Flipse.**, who kindly introduced me such an interesting project and allowed me to become an equal member of his group. Concerning this work my deepest thanks goes to **dr. Peter Zijlstra**, who has always been around to help me with experiments, to discuss the obtained results and together with **Emiel Visser** to spend the Thursday evenings. *Proost!*

I thank people who helped me with the preparation of samples, experiments and simulations, namely: **Marco van der Sluis, Wijnand Dijkstra, Igor Iezhokin, Ameneh Najafi, Calvin Kha, Rostislav Váňa, Michal Kvapil** and **Lukáš Břínek**. My gratitude also belongs to all members of Department of Physical Engineering (BUT), Molecular Materials and Nanosystems (TU/e) and Molecular Biosensing for Medical Diagnostics (TU/e) who were always ready and enthusiastic to help.

Dále bych rád vyslovil mé srdečné poděkování celé mé rodině, bratrovi, sestře a oběma rodičům za jejich neutuchající podporu a lásku. Velké díky také patří všem, kteří mi byli i přes obrovskou dálku nablízku.

Thank you, Dankjewel, Děkuji.

Matěj Horáček

# CONTENTS

<b>Introduction</b>	<b>1</b>
This thesis . . . . .	2
<b>1 Graphene</b>	<b>4</b>
1.1 Electronic properties of graphene . . . . .	4
1.2 Optical properties of graphene . . . . .	7
1.3 Generation of photocurrent in graphene . . . . .	8
1.3.1 Photovoltaic effect . . . . .	11
1.3.2 Photothermoelectric effect . . . . .	11
<b>2 Localized surface plasmons</b>	<b>13</b>
2.1 Optical properties of a bulk metal . . . . .	13
2.1.1 Experimental bulk dielectric function of gold . . . . .	15
2.2 Optical properties of metal nanoparticles . . . . .	16
2.2.1 Mie theory . . . . .	19
2.2.2 Quasi-static approximation . . . . .	19
2.3 Optical properties of gold nanorods . . . . .	21
2.3.1 Gold nanorods in quasi-static approximation . . . . .	22
2.3.2 Gold nanorod properties calculated by FDTD simulations . . . . .	23
2.4 Coupling between graphene and gold nanoparticles . . . . .	24
2.4.1 Dielectric interaction . . . . .	25
2.4.2 Hot carriers interaction . . . . .	26
<b>3 Sample preparation</b>	<b>27</b>
3.1 Growth of epitaxial graphene . . . . .	27
3.2 Exfoliating of graphene . . . . .	29
3.2.1 Flake thickness determination . . . . .	30
3.3 Gold nanorods . . . . .	32
3.4 Deposition of gold nanorods . . . . .	32
3.4.1 Glass functionalization . . . . .	33
3.4.2 Spin-coating deposition . . . . .	35
3.4.3 Deposition from bulk solution upon coverslip immersion . . . . .	36
3.4.4 Transfer of gold nanorods onto graphene . . . . .	41
<b>4 Photodetection</b>	<b>44</b>
4.1 Characterization of prepared systems . . . . .	46
4.2 Photoresponse measurements . . . . .	47

<b>5</b>	<b>Gold nanorod interaction with graphene</b>	<b>53</b>
5.1	Finite-difference time-domain simulations . . . . .	53
5.2	White-light single particle scattering spectroscopy . . . . .	58
5.2.1	Apparatus configuration . . . . .	60
5.3	Gold nanorod interaction with epitaxial graphene . . . . .	62
5.3.1	Optical properties of silicon carbide . . . . .	64
5.4	Layer-dependent study . . . . .	66
<b>6</b>	<b>Conclusion</b>	<b>73</b>
	Suggestions for future research . . . . .	74
	<b>Bibliography</b>	<b>76</b>
	<b>List of abbreviations</b>	<b>87</b>
	<b>Appendix</b>	<b>88</b>
	Appendix A - Sample preparation: The protocols . . . . .	88
	Mechanical exfoliation of graphene - tips & tricks . . . . .	88
	Protocol of gold nanorods deposition using spin-coating . . . . .	89
	Protocol of gold nanorods deposition from bulk solution upon cover- slip immersion . . . . .	90
	Protocol of gold nanorods transfer onto graphene . . . . .	91
	Appendix B - Solar spectrum . . . . .	92
	Appendix C - The refractive index library . . . . .	93
	Appendix D - FDTD simulations: The computing system description . . . . .	96

# INTRODUCTION

Graphene is a one atomic-layer thick two dimensional crystal composed of carbon atoms arranged into a hexagonal lattice. Its discovery dates back to 2004, when Geim and Novoselov from the University of Manchester successfully isolated the graphene layer from a bulk graphite, which triggered its intense research. Graphene shows a multitude of striking properties like excellent tensile strength, extraordinarily high carrier mobility or zero bandgap. That makes it an extremely attractive material for various applications ranging from electronics to chemical sensing, including the photodetection. The latter one takes a unique property of graphene to create several photoexcited carriers by an only one absorbed photon.

Graphene shows up a spectrally flat absorption of light of  $\sim 2.3\%$ , which is a quite high number when considering a graphene thickness of only one atom. Nevertheless, for the photodetection applications, this value is noticeably low. Therefore, the graphene intrinsic light absorption needs to be enhanced to ensure the effective and sensitive photodetection. Such an enhancement can be realized by placing metallic nanostructures on the graphene surface showing the unique property of plasmon resonance creation.

By illuminating such a metallic nanostructure made of noble metals its conductive electrons interact with the incoming electromagnetic field, giving rise to their collective oscillation in the nanostructure, the so-called localized surface plasmon resonance. The resonance wavelength depends on the shape, size, orientation and the local environment of the particle, as well as the polarization of the incident light. These plasmons interact with the light leading to strong scattering and absorption of light by the nanoparticle. Moreover, due to the plasmon oscillations the electromagnetic field in the close vicinity of metallic nanoparticle is strongly enhanced and highly confined on a scale much smaller than the wavelength of incident light. The field of *plasmonics* is a rapidly growing and well-established research area, which covers various aspects of surface plasmons towards realization of a variety of plasmon-based devices, which application ranges from reconfigurable meta-surfaces to biological sensing, including also the opto-electronics.

The synergy of graphene and plasmonically active nanoparticles thus offers an opportunity to create an ultra-fast and super-sensitive photodetection device. Additionally to the enhanced graphene intrinsic absorption, the properties of plasmonic particles are transferred, making this hybrid conjugate behavior dependent on the wavelength of incoming light. The development of such a novel graphene / nanoparticle hybrid devices is currently the subject of tremendous research interest. The functionality and properties of such a hybrid device are determined by the transfer of energy between the localized surface plasmon in the metal nanoparticle and the

graphene. Despite the intensive research the exact underlying mechanism causing the energy redistribution in this system is not given yet. However, answering this fundamental question is necessary to fully understand and improve the devices using the graphene / nanoparticle conjugate to convert light into electricity and thus find its place as an application in the fields of photodetection and photovoltaics.

## **This thesis**

This work was done under the supervision of prof. RNDr. Tomáš Šikola, CSc. in close cooperation with Eindhoven University of Technology (TU/e). Here, author of this thesis became a member of the scientific research groups Molecular Materials and Nanosystems (M2N) and Molecular Biosensing for Medical Diagnostics (MBx). Most of the experiments later on published and discussed in this thesis were proceeded in the laboratories of these groups under thorough supervisions of dr. Peter Zijlstra and dr.ir. Cees F.J. Flipse.

In this thesis the necessary theory, experimental methods, numerical calculations and experimental results are discussed to achieve an efficient photodetection using a graphene photodetector based on plasmonic nanoparticles and to determine the underlying mechanism responsible for the interaction between graphene and plasmonic nanoparticles.

In Chapter 1 the brief introduction into graphene is given, focusing on its electronic and optical properties. The attention is paid mainly to the generation of photocurrent in graphene showing the extraordinary property of graphene - the carrier multiplication. In Chapter 2 the theoretical background for the optical behavior of plasmonic particles is given. The first section discusses the optical response of a bulk metal and the second one focuses on the optical properties of metal nanoparticles giving the emphasis on plasmon damping channels. Later on, the Mie and Rayleigh theories are introduced followed by the discussion of gold nanorod properties. The last section then discusses the possible interactions between gold nanoparticles and an underlying graphene substrate.

Chapter 3 deals with preparation of samples later used for experiments. The photodetection experiments are thoroughly discussed in Chapter 4, wherein the detailed description of prepared samples is given followed by measurements of photoresponse of the prepared devices. Chapter 5 treats the interaction of gold nanorods with graphene. The first section discusses the numerical calculations of the system, the second one describes microscopy and spectroscopy of gold nanoparticles. The

last two sections then deal with the white-light spectroscopy measurements of single particles on graphene in order to determine the particle plasmon damping pathways present in the system.

The final chapter of this thesis then concludes the obtained results, summarizes the work done in this thesis and finishes with an outlook on possible improvements and future applications.

# 1 GRAPHENE

Graphene is a two-dimensional crystal of carbon, meaning a single atomic layer of carbon atoms. Two-dimensional crystals have been studied on a theoretical level from the first half of the 20th century starting with work by Peierls [1] and Landau [2]. Both of them concluded that such materials are thermodynamically unstable (tend to decompose or segregate) due to thermal fluctuations preventing a long-range crystalline order at finite temperatures. Graphene itself, specifically its band structure, was described later in 1947 by Wallace [3].

In 2004 groundbreaking research was done by Andre Geim and Kostya Novoselov [4–6] from the University of Manchester. They successfully isolated graphene sheets using a mechanical exfoliation method. Geim and Novoselov were later (in 2010) awarded the Nobel Prize in Physics *”for groundbreaking experiments regarding the material graphene”*. In spite of Peierls’ and Landau’s theory two dimensional crystals were found to be stable enough due to the gentle warp of the crystal [7]. Graphene exhibits unique mechanical [8], electronic [6,9] and photonic [10,11] properties which attract a great interest in research and industry.

Here, in this chapter, the graphene electronical properties with emphasis on the doping effect are discussed. Later on, the optical properties of graphene are described followed by discussion dealing with photocurrent generation in graphene. In this last section the extraordinary property of graphene - the generation of hot carriers - is discussed to get basic insight into problematique of photodetection using graphene layers.

## 1.1 Electronic properties of graphene

The carbon atoms in graphene are arranged in a hexagonal honeycomb lattice due to  $sp^2$  covalent bonds. It is these  $sp^2$  bonds which are responsible for extraordinary properties of graphene. In graphene the carbon  $s$  and  $p$  in-plane orbitals ( $p_x$  and  $p_y$ ) are hybridized creating a strong covalent  $\sigma$ -bond between neighbouring carbon atoms. The  $sp^2$  bonds and their conformation are the nature of high mechanical strength of graphene. The unaffected out-of-plane  $p_z$  orbitals lead to the creation of  $\pi$  bonds which are responsible for the unique electronic properties of graphene.

The thickness of graphene  $d$  is assumed to be equal to the extension of the out-of-plane  $\pi$  orbitals [12], giving  $d \approx 3.4 \text{ \AA}$  [7]. The hexagonal structure of graphene, as shown in figure 1.1a, can be seen as a rhombic lattice with a basis of two crystallographically equivalent atoms A and B per unit cell. The lattice basal vectors  $\vec{a}_1$

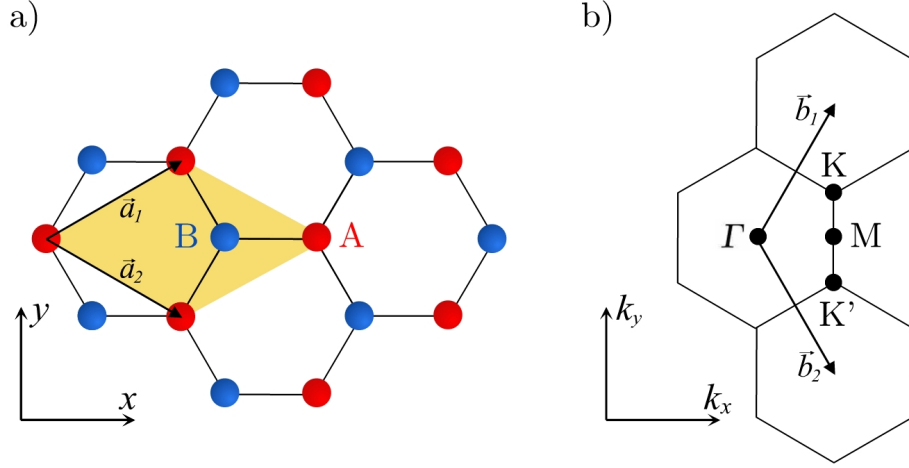


Fig. 1.1: a) Schematic image of the graphene honeycomb lattice in the real space, b) schematic picture of graphene reciprocal lattice. The designation A and B corresponds to the two crystallographically equivalent atoms belonging to unit cell of graphene,  $\vec{a}_1$  and  $\vec{a}_2$  are the lattice basal vectors,  $\vec{b}_1$  and  $\vec{b}_2$  are the reciprocal-lattice vectors.  $\Gamma$ , M, K and  $K'$  are high symmetry points of the reciprocal Brillouin zone,  $\Gamma$  corresponds to the centre of first Brillouin zone, M is the symmetry point at the halfway to another atom in the reciprocal lattice and K and  $K'$  are the Dirac points.

and  $\vec{a}_2$  [7] can be then written as

$$\vec{a}_1 = \frac{a}{2} (3, \sqrt{3}), \quad (1.1)$$

$$\vec{a}_2 = \frac{a}{2} (3, -\sqrt{3}), \quad (1.2)$$

where  $a = 1.42 \text{ \AA}$  is the distance between two neighboring carbon atoms in the lattice. The size of the basal vectors gives the lattice constant of graphene  $a_G = 2.46 \text{ \AA}$ . The reciprocal lattice of graphene is depicted in figure 1.1b, note that one hexagon corresponds to the Brillouin zone of graphene. The reciprocal-lattice vectors  $\vec{b}_1$  and  $\vec{b}_2$  are given by

$$\vec{b}_1 = 2\pi \frac{\vec{a}_2 \times \vec{n}}{|\vec{a}_1 \times \vec{a}_2|} = \frac{2\pi}{3a} (1, \sqrt{3}), \quad (1.3)$$

$$\vec{b}_2 = 2\pi \frac{\vec{n} \times \vec{a}_1}{|\vec{a}_1 \times \vec{a}_2|} = \frac{2\pi}{3a} (1, -\sqrt{3}), \quad (1.4)$$

where  $\vec{n}$  is the unit vector perpendicular to the plane defined by the vectors  $\vec{a}_1$  and  $\vec{a}_2$ .

The  $\pi$  electrons form valence and conduction bands and thus are responsible for the electronic properties of graphene. The valence and the conduction bands

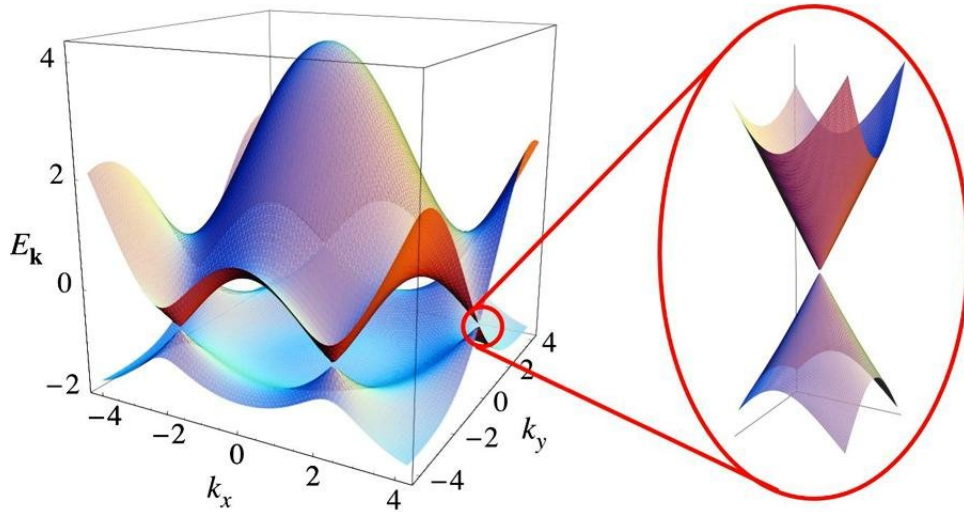


Fig. 1.2: Electronic dispersion relation in the graphene honeycomb lattice. The figure corresponds to first Brillouin zone of reciprocal space of graphene and the energy dispersion relation. In the zoom the energy bands close to one of the Dirac points are depicted. Adapted from [9].

of electrons in graphene honeycomb lattice touch at six points in reciprocal space (Fig. 1.2) – in the Dirac points (K, K') - making graphene a semiconductor with a zero bandgap. From figure 1.2 it is clear that the band structure has a conical shape in the vicinity of the Dirac points meaning that graphene exhibits a linear dispersion relation.

In the case of free-standing graphene with no defects the valence band is fully occupied and conduction band is completely empty. The Fermi energy of the system is therefore at the Dirac points (Fig. 1.3). The linear dispersion relation and the absence of bandgap provide an opportunity to tune the type and value of the conductivity in graphene. Tuning can be realized by shifting the Fermi energy for instance by applying a gate voltage [13,14], creating defects in the layer [9] or adsorbing atoms or molecules on the graphene surface [15,16]. By shifting the Fermi energy level below the Dirac points graphene becomes p-doped and by shifting the Fermi energy level above the Dirac points graphene becomes n-doped. The lowest conductivity of graphene appears when the Fermi energy level lies right at the Dirac point.

This behavior of graphene together with its extraordinarily high carrier mobility<sup>1</sup> give a rise of a new generation of electronic components ranging from the high-

<sup>1</sup>Graphene shows the highest reported carrier mobility from known materials  $\mu \approx 4 \cdot 10^4 \text{ cm}^2\text{V}^{-1}\text{s}^{-1}$  [17] at room temperature and even  $\mu \approx 2 \cdot 10^5 \text{ cm}^2\text{V}^{-1}\text{s}^{-1}$  at temperatures close to absolute zero [17].

frequency transistors [18] to the ultra-sensitive graphene based chemical sensors enabling sensing of a single atom [16]. Moreover, currently the attention is paid to highly sensitive graphene photodetectors enabling detection of a single photon [11]. The corresponding optical properties of graphene are discussed in following section.

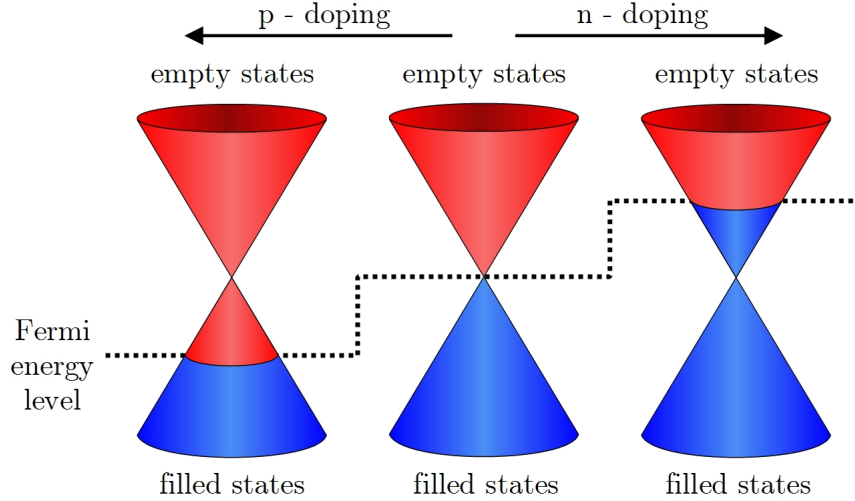


Fig. 1.3: Schematic picture of the type and value of graphene conductivity as a function of the Fermi energy level.

## 1.2 Optical properties of graphene

The adjustment of the Fermi energy level of graphene has a profound effect on the optical properties. The reason is straightforward, optical transitions are allowed only between occupied and unoccupied states. In case of undoped graphene the Fermi energy level lies at the Dirac points allowing the interband optical transitions with any possible energy. This in principle leads to a strong absorption of the incoming radiation.

Despite being only one atom-layer thick, graphene is found to absorb a relatively significant fraction of incident light  $A = 2.3 \pm 0.1 \%$  and shows negligible reflectance  $R < 0.1 \%$  [19]. Therefore the absorbance of graphene corresponds roughly to  $1 - T$ , where  $T$  is transmittance. The optical transmittance is spectrally flat in the visible or near-infrared part of spectrum [19,20] and which is also true when other graphene layers are added. The dependence of light transmittance on the number of graphene layers was calculated and experimentally verified by Zhu *et al.* [21]. This dependence is described by the following equation:

$$T = \left(1 + \frac{1.13\pi\alpha}{2}N\right)^{-2} \longrightarrow N = \frac{2}{1.13\pi\alpha} (\sqrt{T} - T), \quad (1.5)$$

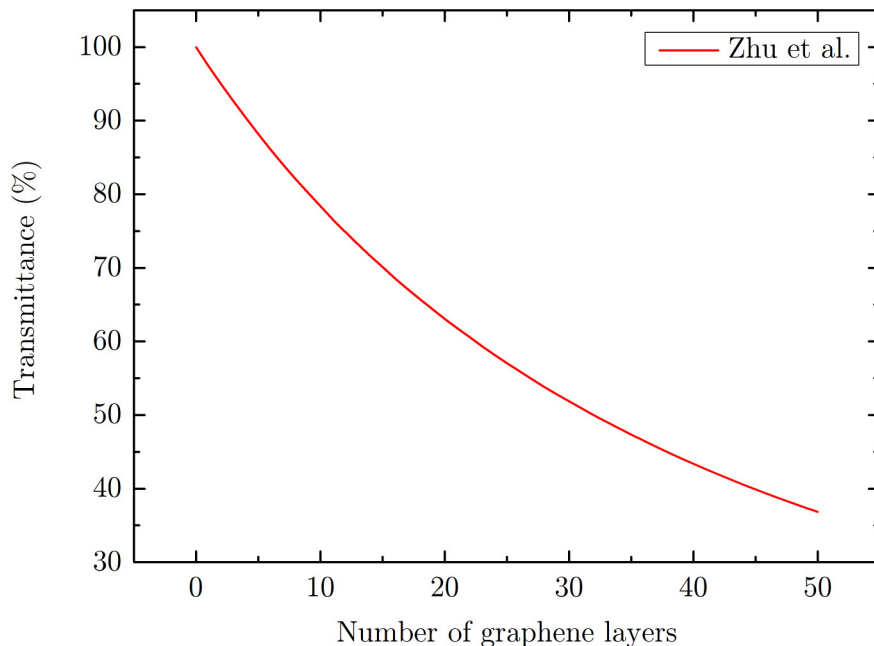


Fig. 1.4: The light transmittance through the graphene / graphite as a function of the number of graphene layers. The dependence is given by equation 1.5 derived and verified by Zhu *et al.* [21].

where  $T$  is the transmittance of light,  $\alpha = e^2/hc \approx 1/137$  is the fine-structure constant and  $N$  is the number of graphene atomic layers. The corresponding graph is shown in figure 1.4.

To get further insight into graphene interaction with light the wavelength dependent optical constants of graphene need to be known. Although it is difficult to measure the optical constants of a single layer of atoms, Weber *et al.* [22] determined the complex dielectric function and thus complex refractive index by spectroscopic ellipsometry measurements (Fig. 1.5). However, these optical constants are not fully reliable because graphene is a strongly anisotropic medium, where the optical constants are different in in-plane and out-of-plane directions. Nevertheless, this data gives trustworthy spectral results even when a simple Fresnel model is applied. Moreover, these data will be later used for numerical simulations described and discussed in detail in section 5.1.

### 1.3 Generation of photocurrent in graphene

Due to the absence of a bandgap graphene can absorb light and convert it into a photocurrent over a wide range of the electromagnetic spectrum, from ultraviolet

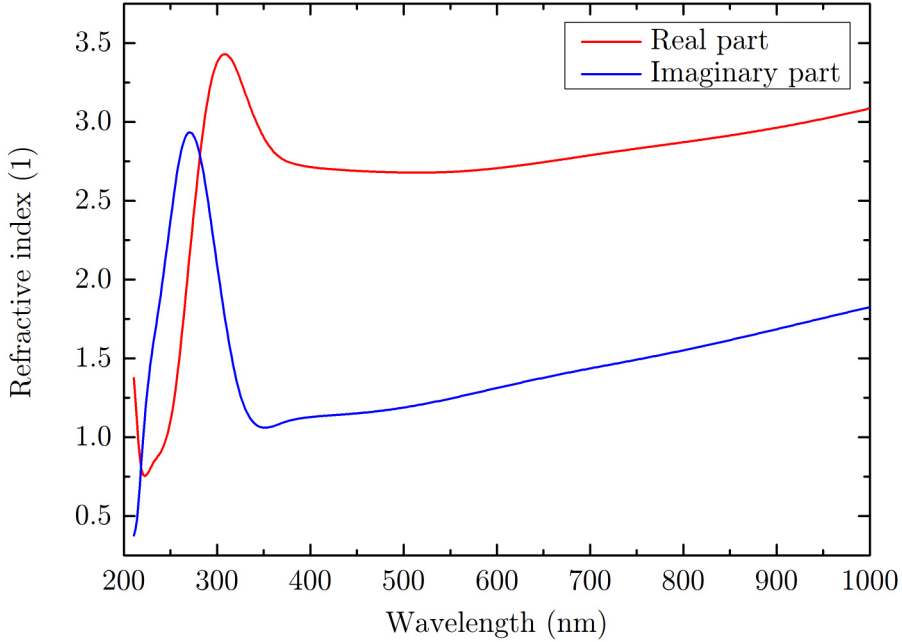


Fig. 1.5: Complex refractive index of graphene measured by spectroscopic ellipsometry [22].

to visible and infrared regimes [10]. However, the mechanism of photocurrent generation in graphene is still debated in literature. There are two competing channels responsible for the origin of the photoresponse: the photothermoelectric and the photovoltaic effect, both described in detail later in the text. Importantly graphene offers the opportunity to create multiple electron-hole pairs when absorbing a single photon, resulting into a phenomenon called *carrier multiplication* [23].

The incident photon is absorbed and generates an initial electron-hole pair which then relaxes into non-equilibrium hot carriers with a temperature higher than that of the lattice [24,25] (Fig. 1.6a). The expression *hot carrier* means that the electron or hole possesses an excess energy (higher than thermal energy) compared to the Fermi energy level of the system.

The processes enabling redistribution of primary photoexcited carriers into a hot carrier distribution are: Auger-like processes, electron-electron scattering, electron-phonon scattering and optical phonon emission (Fig. 1.6b). One can distinguish two types of the Auger-like processes, both the Auger recombination and the impact ionization occurs especially in the case of undoped graphene [23,27,28]. During the Auger recombination an electron is scattered from the conduction band into the valence band (1), while the corresponding energy is transferred to another electron.

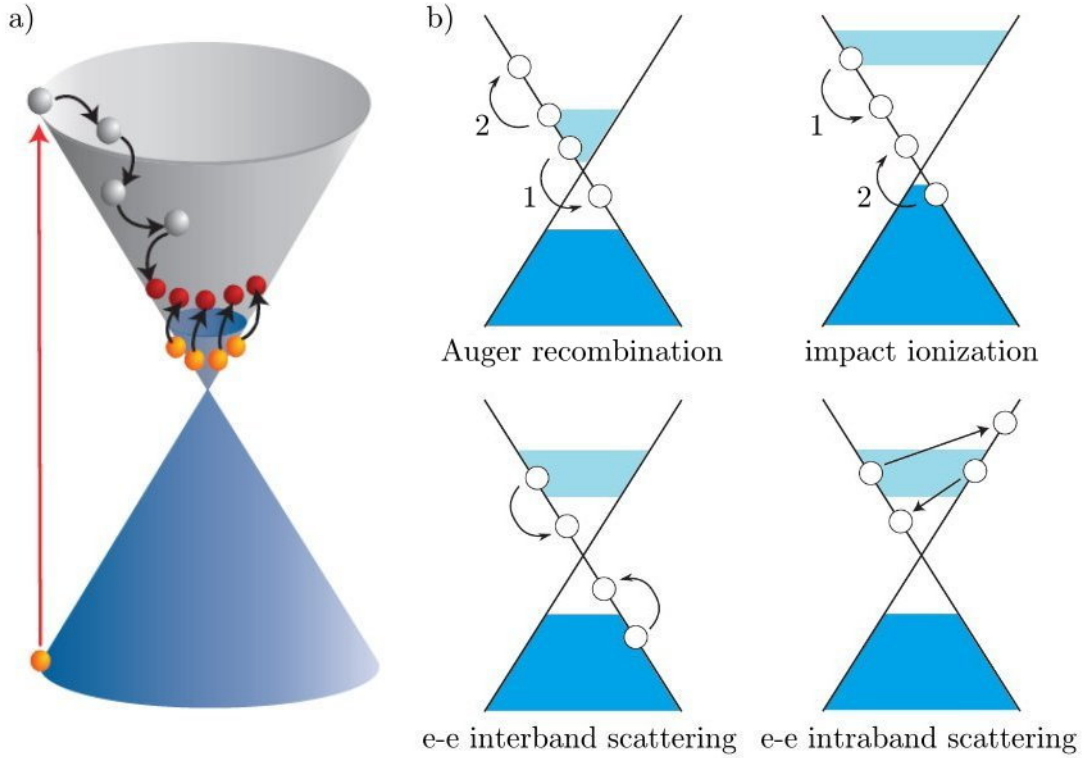


Fig. 1.6: The carrier multiplication in graphene: a) Schema of initial photon absorption and subsequent energy relaxation resulting in creation of hot carriers distribution. The figure is adapted from [26]. b) Schematics of possible energy redistribution processes: Auger recombination, impact ionization, electron-electron (e-e) interband and electron-electron intraband scattering. Note that all these processes occur also for holes.

This second electron is then brought to an energetically higher state within the conduction band (2). The opposite and also more probable Auger-like process is the impact ionization [23,27]. Here an electron relaxes to an energetically lower state (1) inducing the excitation of an electron from the valence band into the conduction band (2) resulting in an increase of the hot carrier density. Both processes also occur for holes in an analogous way. The third possible energy relaxation process of photoexcited carriers is the electron-electron scattering. Unlike the Auger-like processes the probability of Coulombic scattering is much higher, especially in the case of doped graphene [24–26, 29]. The Coulomb-induced scattering events occur for both interband and intraband transitions leading to a significant increase of the carrier density. Again, these relaxation processes occur also for holes.

Other phenomena of hot carrier relaxation is electron-phonon scattering and optical phonon emission [23, 27]. These processes transfer the energy of photoexcited carriers into the lattice. Nevertheless, the energy redistribution from photoexcited

carriers to the lattice is extremely inefficient [29] resulting in the quenching of the electron-phonon scattering and the optical phonon emission channels. Due to this bottleneck the carrier density is distinctly enhanced and its temperature stays hotter than that of lattice for a few picoseconds [26, 30–34]. Eventually the hot carrier distribution relaxes to equilibrium with the lattice particularly by electron-hole recombination.

Once the enhanced hot carrier distribution is established, the charge carriers can be directed towards contacts to yield the photocurrent due to either the photothermoelectric or the photovoltaic effect or their combination. The following sections describe these two effects.

### 1.3.1 Photovoltaic effect

In most of photo-sensitive device types and configurations the photoresponse is governed by the photovoltaic effect. The electron-hole pairs created by absorbing photons are separated by a built-in field established inside the system. These free carriers, both the electrons and the holes, then contribute to the photocurrent. The presence of the internal electric field capable of separating the light induced electron-hole pairs is crucial for the function and properties of devices. The efficiency of exciton separation is proportional to the electric potential step  $\Delta V$  across the system.

The built-in field in the graphene layer can be established by direct doping by atoms or molecules [15, 16], contacting of graphene with metal contacts [35, 36] or by applying a gate voltage [13, 14]. The photovoltaic nature of the photocurrent in graphene is supported especially by earlier works dealing with a photocurrent response in the vicinity of graphene-metal contacts [13, 14, 37–39]. The latest work [40] also supports the photovoltaic effect in graphene but only as a contribution to the total photocurrent.

### 1.3.2 Photothermoelectric effect

On the other hand, there is a plenty of publications [24, 26, 40–45] dealing with the photo-thermoelectric effect as a source of the photocurrent generated in graphene. The photothermoelectric effect results from the local heating of a junction between two different materials by an incident light. The strength of the thermoelectric effect is described by Seebeck coefficient and can be written as:

$$I = \frac{s_1 - s_2}{R} \Delta T, \quad (1.6)$$

where  $I$  is the electric current,  $s_1$  and  $s_2$  are the Seebeck coefficients of the two materials,  $R$  is the electrical resistance of a device and  $\Delta T$  is the temperature

difference. In case of graphene the temperature difference is established by the local creation of hot carriers with temperature  $T_{\text{HC}}$  giving

$$\Delta T = T_{\text{HC}} - T_0, \quad (1.7)$$

where  $T_0$  is the temperature of the lattice. The photocurrent is further governed by the Seebeck coefficients. The Seebeck coefficient is determined by the formula derived by Mott [46]:

$$s = -\frac{\pi^2 k_{\text{B}}^2 T_{\text{HC}}}{3e} \frac{1}{\sigma} \frac{d\sigma}{d\mu}, \quad (1.8)$$

where  $k_{\text{B}}$  is the Boltzmann constant,  $e$  the elementary charge,  $\sigma$  the conductivity and  $\mu$  the chemical potential. Equation 1.8 shows a dependence of the Seebeck coefficient on conductivity and chemical potential. This can be fully exploited in the case of graphene, where both can be easily tailored by the proper formation of doping profile created in graphene. This behavior of the Seebeck coefficient in graphene was calculated [25] and measured [25, 47] giving a good agreement with formula 1.8.

Due to the existence of hot carrier distribution in graphene the temperature difference in equation 1.6 is nonzero. Therefore the difference in the Seebeck coefficients of differently doped areas of graphene is a crucial parameter for the creation of photocurrent by the photothermoelectric effect. The experimental work by Gabor *et al.* [24] shows that the photothermoelectric nature of graphene intrinsic photoresponse dominates over the photovoltaic effect at temperatures ranging from room temperature down to 10 K. Moreover, according to the theoretical calculation by Song *et al.* [25] the ratio between the photocurrents governed by photo-thermoelectric and photovoltaic effects is estimated to be  $15 \sim 20$  showing more significant contribution to photocurrent in graphene caused by photo-thermoelectric effect.

No matter the nature of photocurrent generation in graphene, the graphene layers exhibit spectrally flat light absorption of light of only  $\sim 2.3\%$  [19]. This value is considerably low for photodetection applications and therefore its significant enhancement needs to be provided. This can be done by placing optimized plasmonic nanostructures on the graphene surface. Under resonant excitations such plasmonic nanostructures are capable to focus the electromagnetic radiation into nanometric areas and thus provide strong electric field enhancements resulting in increasing absorption and thus enhanced harvesting of a photocurrent generated in graphene. Moreover, the plasmonic structures give an opportunity to modify the optical response by designing both their shape and the size. The following chapter focuses on such a plasmonic gold structures and discusses their properties and interaction with graphene.

## 2 LOCALIZED SURFACE PLASMONS

Gold crystals were prepared in a colloidal solution for the first time by Faraday in 1857 [48]. Since that, many of their interesting and complex properties were discovered and researched. The most striking one is a collective oscillation of conduction electrons in the crystal, so-called localized surface plasmon arising from the interaction of electrons with electromagnetic fields. Interestingly, these plasmons can be theoretically described by using classical electrodynamics based on Maxwell's equations and solid state physics. The theory of electrodynamics describes the interaction of both electric and magnetic fields with a matter. However, certain material properties, like the dielectric function, can not be calculated from the electrodynamics theory and thus appear in the formulas as input parameters. Therefore, the solid state physics comes in and together with electrodynamics is able to describe the physical phenomena taking place in small metal crystals.

In this chapter the optical properties of a bulk metal and metal nanoparticles are discussed. First, the Drude model describing the optical response of a bulk metal is introduced followed by correlation of this model with experimental data for bulk gold. The optical properties of metal nanoparticles are discussed with emphasis on the plasmon damping channels and the scattering and absorption of light by nanoparticles are described using the Mie and Rayleigh theory. Later on, the attention is paid to the optical properties of gold nanorods. In the last section of this chapter the coupling between gold nanocrystals and graphene is discussed phenomenologically.

### 2.1 Optical properties of a bulk metal

In 1900 Drude proposed a model describing the optical response of bulk metals [49]. The Drude model considers the electrons in a metal as a gas of independent, point-like particles which are able to move freely through the material in between collisions. These electron collisions are incorporated into the model by assuming a relaxation time  $\tau$  of free electrons have between two collisions. The idea of the free electron gas in the metal can be used when only the conduction electrons contribute to the optical properties. For gold this model is applicable only for the wavelengths above 700 nm, below this threshold the contribution of internal bounded electrons to optical properties become significant.

The response of a dielectric medium to electromagnetic waves is described by the dielectric function  $\varepsilon(\omega)$ , also called permittivity, defined in terms of the electric field  $\vec{E}$ , polarization  $\vec{P}$  and displacement  $\vec{D}$  [50]:

$$\vec{D} = \varepsilon_0 \vec{E} + \vec{P} = \varepsilon \varepsilon_0 \vec{E}, \quad (2.1)$$

where  $\varepsilon_0$  is the permittivity of vacuum. Thus, the dielectric function can be derived as follows. The equation of motion for a free electron considering the damping  $\gamma_0 = 1/\tau$  caused by electron collisions is [51]

$$m \frac{\partial^2 \vec{x}}{\partial t^2} + m\gamma_0 \frac{\partial \vec{x}}{\partial t} = -e\vec{E}, \quad (2.2)$$

where  $m$  is the electron mass,  $\vec{x}$  is the deviation from the equilibrium position and  $e$  is the charge of electron. When  $\vec{x}$  and  $\vec{E}$  are supposed to have a harmonic time dependence  $e^{-i\omega t}$ , the solution of equation 2.2 is of the form [51]

$$\vec{x}(t) = \frac{e}{m\omega(\omega + i\gamma_0)} \vec{x}(E). \quad (2.3)$$

Conduction free electrons are displaced by an external electric field  $\vec{E}$  with respect to a lattice consisting of positively charged ions and hence the material becomes polarized. Considering the dipole moment of one electron  $\vec{p} = -e\vec{x}$  and assuming the density of free electrons  $n$ , we can obtain the polarization [51]

$$\vec{P}(t) = n\vec{p}(t) = -ne\vec{x}(t) = -\frac{ne^2}{m\omega(\omega + i\gamma_0)} \vec{E}(t). \quad (2.4)$$

Substituting the relation 2.4 for  $\vec{P}(t)$  in equation 2.1 gives the dielectric function [51]

$$\varepsilon(\omega) = 1 - \frac{\omega_p^2}{\omega(\omega + i\gamma_0)}, \quad (2.5)$$

where  $\omega_p^2 = \sqrt{ne^2/\varepsilon_0 m}$  is the plasma frequency.

To take into account the quantum mechanical properties and the non-harmonic behavior of electron caused by the presence of band gaps, we replace the free electron mass  $m$  by an effective mass  $m^*$  defined as  $m^* = \frac{\hbar^2}{d^2\epsilon/dk^2}$ , where  $\epsilon$  is the electron energy. Basically, it means that electron accelerated upon an external electric field with respect to an ion lattice behaves like a free electron with an effective mass instead of its natural mass  $m$ . Therefore, the final expression for the dielectric function is then given by [51]

$$\varepsilon(\omega) = \varepsilon_\infty - \frac{ne^2}{\varepsilon_0 m^*} \frac{1}{\omega(\omega + i\gamma_0)} = \varepsilon_\infty - \frac{\omega_p^2}{\omega(\omega + i\gamma_0)}, \quad (2.6)$$

where the plasma frequency is newly given by  $\omega_p^2 = \sqrt{ne^2/\varepsilon_0 m^*}$ . The quantity  $\varepsilon_\infty$  corresponds to the high-frequency term, which occurs due to the interband and core transitions of electrons.  $\varepsilon_\infty$  is reduced to 1 for metals, where only the conduction electrons contribute to the optical response. The equation 2.6 is in literature often referred as the Drude-Sommerfeld model.

The dielectric function given by both the Drude model (Eqn. 2.5) and the Drude-Sommerfeld model (Eqn. 2.6) is obviously a complex function. Therefore, it can be expressed in form [52]

$$\varepsilon(\omega) = \varepsilon'(\omega) + i\varepsilon''(\omega), \quad (2.7)$$

where  $\varepsilon'(\omega) = \text{Re}\{\varepsilon(\omega)\}$  is the real part of the complex dielectric function and  $\varepsilon''(\omega) = \text{Im}\{\varepsilon(\omega)\}$  is its imaginary part. However, the optical properties of materials can be also described in form of the complex refractive index  $N(\omega)$ , which can be written in a similar form as the complex dielectric function [52]

$$N(\omega) = n(\omega) + ik(\omega), \quad (2.8)$$

where  $n(\omega) = \text{Re}\{N(\omega)\}$  is the real part of the complex refractive index and  $k(\omega) = \text{Im}\{N(\omega)\}$  is its imaginary part also called the extinction coefficient. The complex dielectric function and the complex refractive index are connected together by the following equations making these two quantities completely interchangeable for description of material optical properties [52]

$$N(\omega) = \sqrt{\varepsilon(\omega)}, \quad (2.9)$$

$$\varepsilon' = n^2 - k^2, \quad (2.10)$$

$$\varepsilon'' = 2nk, \quad (2.11)$$

$$n = \sqrt{\frac{\varepsilon'}{2} + \frac{1}{2}\sqrt{\varepsilon'^2 + \varepsilon''^2}}, \quad (2.12)$$

$$k = \frac{\varepsilon''}{2n}. \quad (2.13)$$

### 2.1.1 Experimental bulk dielectric function of gold

The Drude-Sommerfeld model described by equation 2.6 gives good reliable results for low energies, but the model does not take into account the complex electronic structure of metals resulting from their bound electrons. This leads to large deviations at higher energies (still corresponding to the visible part of spectrum). In noble metals, such as gold or silver, the high energy deviations are mainly caused by interband transitions, i.e. the electron excitations from the d-bands into the conduction band [53]. It is not trivial to incorporate these contributions into the free-electron model and hence the experimentally measured values of the dielectric function are often used for calculations.

The most often used experimental data for the dielectric function of gold was measured by Johnson and Christy [54]. They obtained the results by measuring the transmission and reflectance of clean metal films in high vacuum. The dielectric function of gold as measured by Johnson and Christy [54] together with the

calculated Drude-Sommerfeld model (Eqn. 2.6) are shown in figure 2.1. The real part of Drude-Sommerfeld dielectric function fits nicely to the measured values. However, the imaginary part is only well approximated by this model at energies below  $\sim 1.8$  eV (corresponding to wavelengths above  $\sim 700$  nm), at higher energies the interband transitions contributions become significant resulting into large deviations from the Drude-Sommerfeld model.

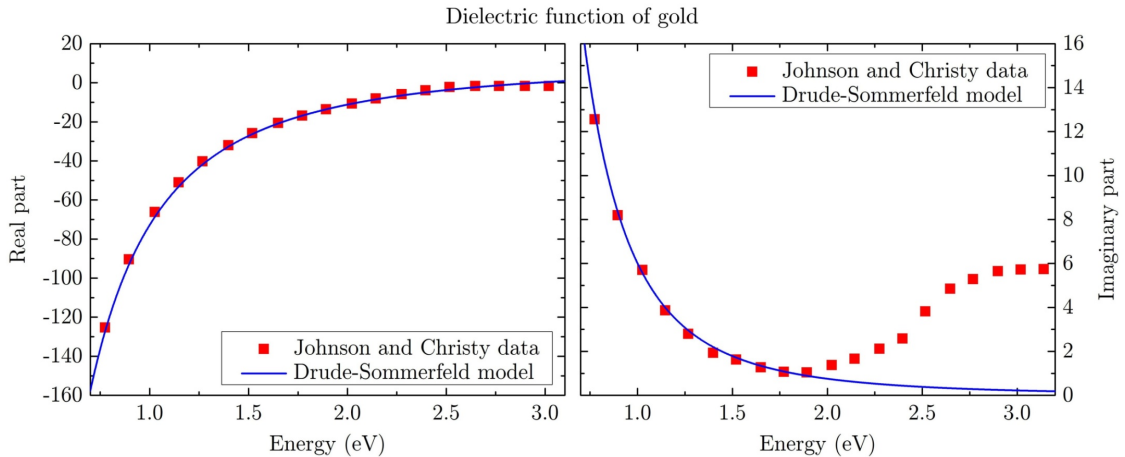


Fig. 2.1: The real (left) and imaginary (right) part of the complex dielectric function  $\epsilon$  of gold as measured by Johnson and Christy [54] and the dielectric function calculated using the Drude-Sommerfeld, the parameters used in equation 2.6 are  $\omega_p = 9.1$  eV,  $\gamma_0 = 73$  meV and  $\epsilon_\infty = 9.5$  [55].

## 2.2 Optical properties of metal nanoparticles

Plasmons, the collective oscillations of conduction electrons, are the most spectacular property of metal nanoparticles. By creation of a plasmon in a particle the extraordinary optical properties appears giving strong light absorption, scattering and field enhancement in the close vicinity of the particle. These properties are strongly determined by the particle shape and dimensions giving rise, for example, to the vivid colour of their colloidal solution. In following text the discussion dealing with the optical properties of metallic nanoparticles is performed starting with the corrections to the dielectric function of nanoparticles.

In the case of nanoparticles the degrees of freedom are decreased comparing to bulk materials resulting in creation of extra damping channels. The additional damping is caused mainly by two factors: the surface scattering and the radiation damping. The surface-induced scattering increases the oscillation damping due to extra collisions between the electrons and the particle surface. Thus, this channel

becomes significant for very small nanoparticles and its value is inversely proportional to their dimensions [53]. On the other hand the radiation damping occurs due to plasmon resonant modes coupling to the applied electromagnetic field resulting in dipole creation and subsequent light radiation [55]. This damping channel is expressive for large volumes and for spherical nanoparticles becomes dominant for radii larger than 80 nm.

Due to these extra damping channels, the correction of the dielectric function for nanoparticles needs to be done. The corrected dielectric function is given by [55]:

$$\varepsilon(\omega) = \varepsilon_{\text{JC}} + \frac{\omega_{\text{p}}^2}{\omega(\omega + i\gamma_0)} - \frac{\omega_{\text{p}}^2}{\omega(\omega + i\gamma)}, \quad (2.14)$$

where the second term in the Drude-Sommerfeld dielectric function (Eqn. 2.6) is subtracted from the experimental dielectric function determined by Johnson and Christy  $\varepsilon_{\text{JC}}$  [54] and is replaced by a term with the corrected damping factor  $\gamma$ . The corrected damping factor is given by [55]:

$$\gamma = \gamma_0 + \gamma_{\text{S}} + \gamma_{\text{R}} = \frac{1}{\tau} + A \frac{v_{\text{F}}}{\lambda_{\text{eff}}} + 2\kappa V, \quad (2.15)$$

where  $\gamma_0$  is the contribution of bulk gold,  $\gamma_{\text{S}} = A \frac{v_{\text{F}}}{\lambda_{\text{eff}}}$  is the surface-scattering term and  $\gamma_{\text{R}} = 2\kappa V$  is the term corresponding to radiation damping [55, 56]. Moreover,  $v_{\text{F}}$  is the Fermi velocity,  $\lambda_{\text{eff}}$  the mean free path of conduction electrons in the nanoparticle dependent on the dimensions of the particle (see below),  $A$  and  $\kappa$  are empirical constants and  $V$  is the volume of the particle. Coronado and Schatz [57] showed the mean free path is given by  $4V/S$ , where  $V$  is the particles volume and  $S$  its surface area. The constant  $A$  is of the order of unity [56] and  $\kappa = (5.5 \pm 1.5) \cdot 10^{-7} \text{ fs}^{-1} \text{ nm}^{-3}$  [53, 55]. Equation 2.15 clearly shows the surface scattering is dominant for small nanoparticles (small term  $\lambda_{\text{eff}}$ ) and the radiation damping is then dominant for larger particles (due to the large term  $V$ ).

In general, the plasmon damping is caused by energetic losses and results in a finite the width of the plasmon resonance  $\Gamma$ . The decay of the excited electron population may occur by both radiative and non-radiative processes as schematically shown in figure 2.2. The radiative decay channel is the energy relaxation by transformation of plasmons into photons and thus occurs for instance through the scattering or luminiscence. On the other hand, in the non-radiative decay the collective oscillation dephases due to electron-electron scattering resulting in an electron-hole pair formation. These electrons are excited into empty states in the conduction band. If the initial states of these excited electrons are located in the conduction band, the corresponding electrons transitions are called intraband. On the other hand the electron excitations from the d-bands are called interband. In

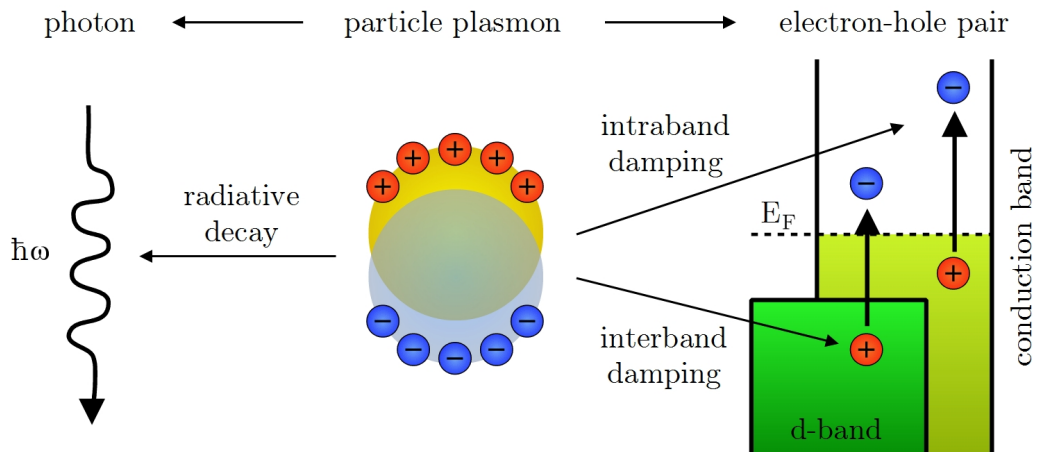


Fig. 2.2: Schematic representation of the particle plasmon damping channels in noble-metal nanoparticles. The decay can be either radiative or non-radiative. During the radiative decay a photon is emitted and the non-radiative decay occurs via excitation of electron-hole pairs either by intraband transition (within the conduction band) or the interband transition (from the d-band into the conduction band).

the case of non-radiative decay channel the energy is after plasmon excitation also transferred into the lattice through electron-phonon coupling giving the heating of the lattice [58].

Interband, intraband and radiation damping channels are the most important contributors to the particle plasmon dephasing. The non-radiative channels are dominant over the radiation damping for small nanoparticles, whereas the radiative decay becomes larger for bigger nanoparticles since the scattering cross section is proportional to square of volume [58]. The interband damping channel is suppressed for low energies, for gold the threshold energy value can be estimated from the dielectric function measured by Johnson and Christy [54] giving the value of  $\sim 1.8$  eV.

When a gold nanoparticle is illuminated by an electromagnetic wave the radiation penetrates into the material. The corresponding penetration depth can be easily determined [59] by using the data obtained by Johnson and Christy [54] giving values of  $30 \sim 40$  nm for the optical wavelengths. This value is comparable to the dimensions of nanoparticles resulting thus in full penetration of the incident light into the particle. This leads to a collective displacement of conduction electrons with respect to the immobile positively charged gold ions in the particle. The positive and negative charges attract each other giving rise to a restoring force. By combination of this restoring force and the mass of electrons a spring-mass system is created and its harmonic oscillations are generated. This collective oscillation of the conduction

electrons in a metal nanoparticle is called a localized surface plasmon resonance (LSPR) or a particle plasmon.

The plasmons in a metal nanoparticle can be described as a damped harmonic oscillator with an external driving force, which is an incident electric field. Therefore, the frequency spectrum of the excited LSPR is a Lorentzian lineshape characterized by the position of the maximum, the eigenfrequency  $\omega_0$ , and the full width at half maximum (FWHM)  $\Delta\omega$ . In the energy units the FWHM is called the plasmon resonance width or the linewidth  $\Gamma$  and it is given by  $\Gamma = \hbar\Delta\omega$ . Considering the mentioned quantities, the Lorentzian frequency spectrum of LSPR can be written as follows

$$E(\omega) = \frac{E_0}{2\pi} \frac{\frac{\Gamma}{2\hbar}}{(\omega - \omega_0)^2 + \left(\frac{\Gamma}{2\hbar}\right)^2}, \quad (2.16)$$

where  $E$  is the electric field present in the nanoparticle and  $E_0$  is the amplitude of the electric field component of incident electromagnetic wave. Equation 2.16 clearly shows the presence of large oscillation amplitudes when the frequency of the incident light is in resonance with the plasmon frequency, even for small incident light amplitudes.

### 2.2.1 Mie theory

In 1908 Mie published a theory [60] providing an analytical solution for the scattering and the absorption of light by a metal sphere, spheroid or ellipsoid. This theory is derived from Maxwell's equations within use of the appropriate boundary conditions resulting in final application of a multipole expansion of electromagnetic fields. A thorough description of the Mie theory can be for example found in Bohren and Huffamn [51]. The Mie theory enables one to calculate the electromagnetic field inside and outside of the spherical particle of any dimension with a great precision. However, the Mie theory is rather complex. Therefore, in the regime where the particle size is much smaller than the wavelength, a straightforward quasi-static approximation is generally preferred. Here, in this thesis, the attention is only paid to such small nanoparticles and, therefore, this quasi-static approximation, which is the first-order approximation of the Mie theory, can be used.

### 2.2.2 Quasi-static approximation

A metal nanoparticle upon an electromagnetic field act as an oscillating dipole at the plasmon frequency due to its alternating surface charges (Fig. 2.3) resulting thus in absorption and scattering of the incident light. Both, the scattering and

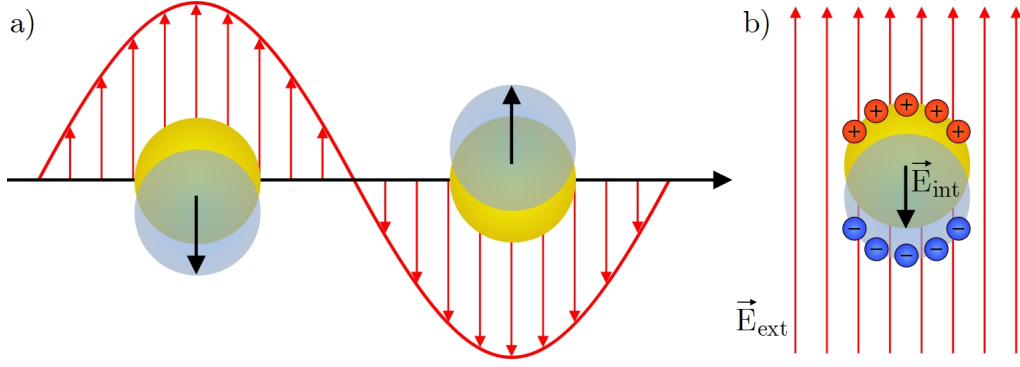


Fig. 2.3: a) Oscillation of an electron "cloud" in a spherical nanoparticle caused by an external oscillating electric field. b) The charge separation in a nanosphere considering the quasi-particle approximation. Here, the external electric field  $\vec{E}_{\text{ext}}$  constant over the whole particle volume induces a restoring electric field  $\vec{E}_{\text{int}}$  inside the sphere.

the absorption, can be relatively simply calculated for particles much smaller than the wavelength of the incident light by a simplified Mie theory called quasi-static approximation (sometimes also referred as the Dipole approximation or Rayleigh theory).

In this situation the external electric field has the same phase over the whole nanoparticle volume, similarly to electrostatics. Therefore, the illuminated particles in the quasi-static approximation behaves like an oscillating dipole and the field outside of the nanoparticle can be described as a superposition of the external field and the field of the point dipole localized in the geometrical center of the nanoparticle.

The scattering and absorption of the light caused by a particle is quantified by the optical scattering  $\sigma_{\text{sca}}(\omega)$  and absorption  $\sigma_{\text{abs}}(\omega)$  cross sections, which are defined as  $P_{\text{sca}}(\omega) = I_0(\omega) \cdot \sigma_{\text{sca}}(\omega)$  and  $P_{\text{abs}}(\omega) = I_0(\omega) \cdot \sigma_{\text{abs}}(\omega)$ . Here the  $P_{\text{sca}}(\omega)$  and  $P_{\text{abs}}(\omega)$  are the power of the scattering and the absorption respectively, and  $I_0$  is the incident light intensity. The total attenuation of the light beam by a nanoparticle is then given by the extinction cross section  $\sigma_{\text{ext}} = \sigma_{\text{sca}} + \sigma_{\text{abs}}$ .

The optical cross sections of a metal nanosphere can be easily calculated from the polarizability  $\alpha$ , which for a sphere is given by the Clausius-Mossotti relation [51]:

$$\alpha_{\text{sphere}} = 3\epsilon_0 V \frac{\epsilon(\omega) - \epsilon_m}{\epsilon(\omega) + 2\epsilon_m}, \quad (2.17)$$

where  $\epsilon_0$  is the vacuum permittivity,  $V$  is the volume of the nanoparticle and  $\epsilon(\omega)$  and  $\epsilon_m$  are the dielectric functions of the metal and surrounding medium, respectively. The optical cross sections are then obtained with the following expressions for the absorption cross section  $\sigma_{\text{abs}}$ , given by [51]:

$$\sigma_{\text{abs}} = \frac{k}{\epsilon_0} \text{Im} \{ \alpha \}, \quad (2.18)$$

and for the scattering cross section  $\sigma_{\text{sca}}$  [51]:

$$\sigma_{\text{sca}} = \frac{k^4 |\alpha|^2}{6\pi\epsilon_0^2}, \quad (2.19)$$

where  $k = 2\pi/\lambda$  is the wave number of light in the surrounding medium.

Here, we have shown the theoretical description of behavior of nanosphere being illuminated by light within the quasi-static approximation. Later in the following text, the description of elongated particles, such as nanorods, in terms of the quasi-static approximation will be discussed. But, at first let us give some introduction into the issue of gold nanorods.

## 2.3 Optical properties of gold nanorods

Elongation of originally spherical plasmonic nanoparticles causes lowering of their geometrical symmetry resulting in an enrichment of their plasmonic properties. Therefore, gold nanorods exhibit anisotropic plasmon responses to the incident light illumination. There are two independent LSPR modes present in a nanorod, the longitudinal and the transversal mode. The first one corresponds to the collective oscillation of conduction electrons along the nanorod long axis and the latter mode is associated with electron oscillations in directions perpendicular to the nanorod axis [58, 61]. Both modes are dipolar resonances for nanorods smaller than approximately 100 nm in length and thus can be efficiently excited by external plane waves [62].

The nanorod transversal LSPR mode corresponds to a LSPR of spherical particle. Therefore, the position of transversal mode is located nearby the position of gold spheres' LSPR  $\lambda_T \sim 520$  nm [58, 61]. On the other hand, the longitudinal LSPR is located at the red side of the transversal one and its direct position is determined mainly by the aspect ratio<sup>1</sup> of the nanorod [63, 64]. By increasing the nanorod aspect ratio the longitudinal mode position red-shifts almost linearly (Fig. 2.4a) followed by an increase of the corresponding peak intensity (Fig. 2.4b). Unlike the longitudinal LSPR, the transversal mode is not affected by aspect ratio changes giving almost constant values for both the position (Fig. 2.4c) and the peak intensity [63, 64]. The increase of the peak intensity showed in figure 2.4c is caused by the increasing gold nanorod volume used in calculations [64].

Both plasmonic modes present in gold nanorods suffer from the energy losses caused by various damping channels discussed in detail in section 2.2. However, an interesting feature arises from the behavior of the longitudinal LSPR. By increasing the gold nanorod aspect ratio and the subsequent red-shifting of the longitudinal

---

<sup>1</sup>The aspect ratio is defined as a ratio between the length and the diameter of the rod.

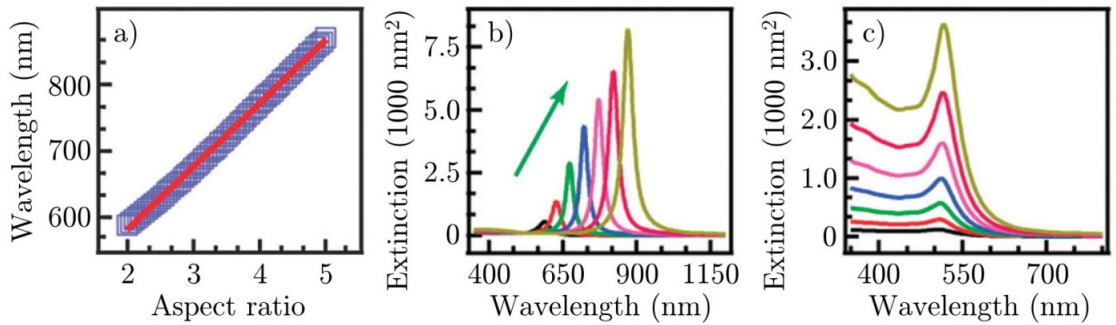


Fig. 2.4: Plasmonic properties of gold nanorods: a) The longitudinal LSPR position as a function of the aspect ratio of nanorod. b) Red-shifting and intensity increasing of the longitudinal LSPR peak with the increasing the aspect ratio of a gold nanorod and c) a nearly constant peak position and linewidth of transversal LSPR mode. The increasing of intensity here is caused by increasing of gold nanorod volume in performed calculations. The pictures are taken from references [61,64] and edited.

mode position the LSPR band gets away from the gold interband transition area. That results in reduction of damping channel caused by the interband transitions and almost its quenching for rods with the high aspect ratio [58,61].

The closing of the interband transition damping channel results in an extremely strong electric near-field enhancement in the nanorod vicinity for the longitudinal LSPR [64]. The largest amplitudes are then present at the regions with high curvatures, such as the two end of the nanorod [64]. These effects make the longitudinal LSPR of gold nanorods extremely sensitive to the changes in refractive index of surroundings, enabling for example photosensing of even a single molecule [65].

### 2.3.1 Gold nanorods in quasi-static approximation

In paragraph 2.2.2 the analytical solution of light scattering and absorption by a metal sphere using a quasi-static approximation was given. However, the Rayleigh theory enables one to get analytical results also for elongated particles satisfying the condition of particle dimensions much smaller than the wavelength of incident light. However, the nanorod needs to be approximated by a *cigar-shaped* ellipsoid.

The elongated particles have an anisotropic polarizability and therefore a geometrical factor  $L_i$  is incorporated into the polarizability equation. The polarizability  $\alpha_i$  in a field along one of its three principal axes  $i$  is given by [51]:

$$\alpha_i = \varepsilon_0 V \frac{\varepsilon(\omega) - \varepsilon_m}{\varepsilon_m + L_i (\varepsilon(\omega) - \varepsilon_m)}, \quad (2.20)$$

where the  $L_i$  depends on the particle geometry. For a considered ellipsoid, where the

semi-axes follow the relation  $a > b = c$ . The geometrical factors are given as [51]:

$$L_1 = \frac{1 - e^2}{e^2} \left( \frac{1}{2e} \ln \left[ \frac{1 + e}{1 - e} \right] - 1 \right) \quad \text{and} \quad L_{2,3} = \frac{1 - L_1}{2}, \quad (2.21)$$

where  $i = 1$  is for the polarization of the incoming field along the long axis and  $i = 2, 3$  for the polarization along the two short axes. The ellipsoid eccentricity  $e$  is given by  $e = \sqrt{1 - b^2/a^2}$ . Note, that for spherical particle the geometrical factors  $L_{\text{sphere}}$  are all equal to  $1/3$  and thus equation 2.20 is reduced into the form of equation 2.17 corresponding to a polarizability of the sphere.

Nevertheless, the analytical solution of optical cross sections given by quasi-static approximation suffers from the shape approximation done for nanorod by assuming it as the ellipsoid. The exact shape of nanorods used in our experiments is a spherically capped cylinder. Moreover, the difference in shapes results in a different volume  $V$  of the nanoparticle giving real larger cross sections for spherically capped cylinders. Therefore, the calculation of scattering cross sections of gold nanorod is performed in this thesis numerically using the finite-difference time-domain (FDTD) method applicable for various shapes and nanostructures.

### 2.3.2 Gold nanorod properties calculated by FDTD simulations

The FDTD method has become one of the most widely used methods for solving Maxwell's equations in structures of complex geometries [66, 67]. FDTD is a grid-based differential numerical modeling method based on discretization of Maxwell's equations in space and time domains. To implement the FDTD solution of Maxwell's equations, a computational mesh has to be first designed. The computational mesh is composed of individual domains which basically is the physical region over which the simulation is performed. Then, both the electric and the magnetic fields are determined at every point of mesh and the process is repeated over and over again until the desired transient or steady-state electromagnetic field behavior is fully evolved [66, 67]. The computed system is determined by specifying the material of each mesh cell. Typically, the material is either free-space (air), metal, or dielectric and can be fully specified by either the dielectric function or the refractive index of a material acting here as an input parameter.

In this thesis the FDTD calculations are done using commercial software *Lumerical* [66]. The proper discussion about the used calculation configuration, data processing and obtained data reliability is given in section 5.1. Here, the example of the scattering spectra and electric field distribution around and inside of a gold nanorod for both LSPRs are shown in figure 2.5. The obtained results correspond

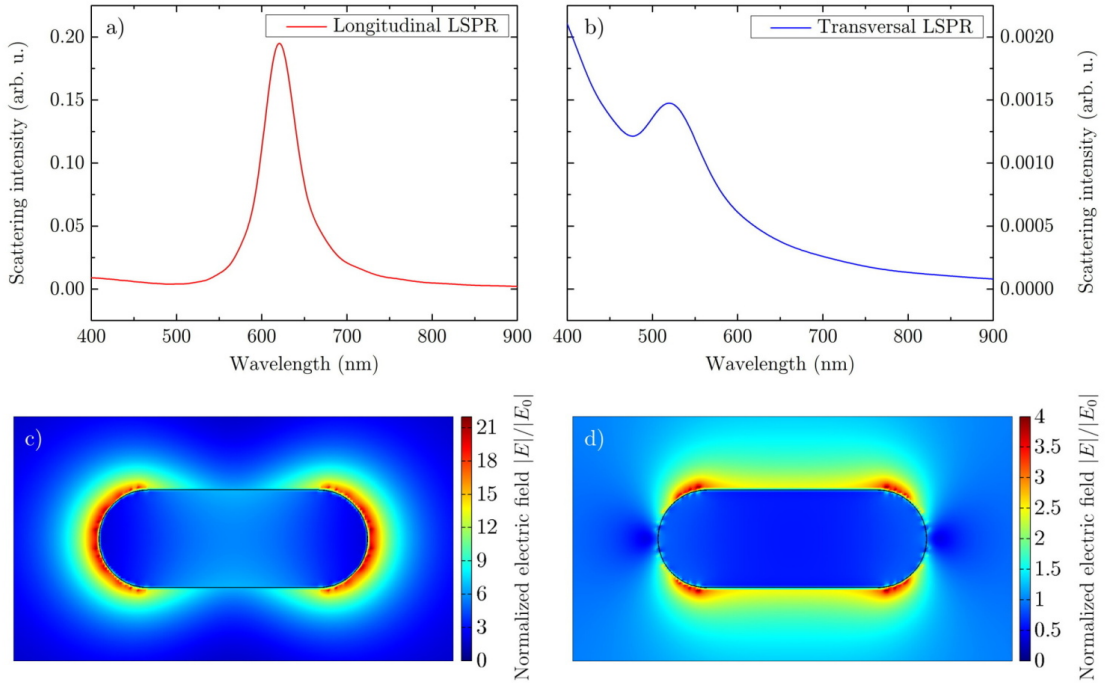


Fig. 2.5: FDTD calculations for scattering intensity and electric field distribution for a gold nanorod with the aspect ratio 2.75, diameter 40 nm and length 110 nm in vacuum illuminated by plane wave: a) Longitudinal LSPR with a peak position of  $\lambda_L = 621$  nm, b) transversal LSPR with a peak position of  $\lambda_T = 523.9$  nm. The normalized electric field enhancement around the nanorod for the longitudinal c) and the transversal d) LSPR bands. Gold was characterized from the experimental data measured by Johnson and Christy [54].

to a spherically capped cylindrical gold nanorod with the aspect ratio 2.75 and diameter 40 nm located in vacuum. As the input material data for gold, the dielectric function measured by Johnson and Christy [54] was used.

## 2.4 Coupling between graphene and gold nanoparticles

Localized surface plasmons have finite lifetimes after which they decay either radiatively by emitting a photon or non-radiatively via intraband or interband transitions resulting in generation of electron-hole pairs. By placing a nanoparticle showing up LSPRs onto a substrate, an additional plasmon damping channel is created [58, 61]. In this section, the effect of underlying graphene substrate on plasmonic nanoparticle behavior is discussed.

The energy of LSPR oscillating in nanoparticle is redistributed into graphene sheet causing a broadening of the LSPR peak. Surprisingly, graphene, the one atom thick carbon layer ( $d \approx 3.4 \text{ \AA}$ ), contributes to the plasmon damping significantly [68, 69]. According to literature there are two plasmon damping channels causing the plasmon energy redistribution into graphene: the classical dielectric interaction between the nanoparticle and the underlying graphene and the injection of the hot electrons generated by illuminated particle into the graphene. Both effects are in detail discussed in following paragraphs.

### 2.4.1 Dielectric interaction

The presence of the underlying substrate brings a symmetry breaking of the dielectric environment surrounding the nanoparticle. The enhanced electric field in the particle vicinity also penetrates into the underlying substrate causing the electrical field enhancement in the substrate. The excitation of LSPRs in the metal nanocrystal results into induction of image charges in the underlying substrate [58]. These image charges then interact with the free electron cloud oscillating in the particle and thus affects the dynamic behavior causing the hybridization in the nanoparticle. That results either in red or blue shifting of the particle plasmon position determined mainly by the real part of the substrate refractive index. Moreover, the result is the creation of an additional plasmon damping channel determined especially by the imaginary part of refractive index of the substrate. In the case of metallic substrates, the LSPRs excited in the particle can strongly couple with propagating plasmons at the metal substrate surface additionally to the image charge induction effect [58, 61].

In the case of graphene the enhanced electric field caused by the illuminated particle penetrates in graphene where enhances the excitation of carriers. These excited carriers then can create a dipole oscillations antiparallel to that of present in the particle. This antiparallel image dipole then reduces the internal field in the nanoparticle resulting in the particle plasmon shift and broadening of which amplitudes are then determined by the complex refractive index of the graphene (Fig. 1.5) and its effective thickness ( $\approx 3.4 \text{ \AA}$ ).

The work done by Niu *et al.* [70] supports the idea of electromagnetic field coupling between plasmonic nanoparticles and underlying graphene. Here the red shift of the LSPR wavelength was reported, however no peak broadening was discussed [70].

## 2.4.2 Hot carriers interaction

However, the recent work done by Hoggard *et al.* [69] shows a significant particle plasmon broadening, when the particle is placed on graphene. The value of this broadening is significantly higher than expected from the classical dielectric interaction and thus attributed to another interaction effect between the nanoparticle and the graphene - the hot electrons injection from the particle into the graphene. Some hot electrons generated in the particle conductively couple with the graphene resulting in their transfer into the graphene layer [71] giving the enhancement of carrier density in graphene and therefore shifting of the Dirac point position [72, 73]. On the other hand the conductive coupling also perturbs the oscillating electron cloud in nanoparticle, which might cause a shift and broadening of the plasmon resonance.

To remind, the term "*hot carriers*" corresponds to the case when the energy difference between the excited electron or hole and the Fermi energy level is bigger than the energies of relevant thermal excitations. In general, the excitation of a particle plasmon, with associated near-field enhancement, results also in generation of hot carriers [74]. At the birth of each photogenerated hot carrier is a photon absorption event. Therefore, the number of hot electrons generated by a particle closely follows its absorption spectrum with some oscillations originated from the discreteness of the electronic levels of the nanoparticle [75]. The hot carriers are especially generated in the regions of the particle where the field enhancement is large [74, 75]. Thus, by increasing the particle size the number of generated hot carriers is enhanced. However, only a small fraction of generated hot carriers can escape out of the particle, because the ejection process competes with very fast carrier relaxation processes [75]. Nevertheless, the injection of excited hot carriers into surrounding materials has been already reported by several works [76–78]. Anyway, from the particle plasmon point of view, the generation of hot carriers acts as an additional damping channel broadening the intrinsic linewidth of LSPR peaks [76].

For a gold nanoparticle placed on a graphene, the formation of a purely conductive coupling plasmon damping channel was reported in works done by Hoggard *et al.* [69] and Dejarnette *et al.* [71]. Moreover, the conductive coupling effect for the graphene has been also supported by work done Konstantatos *et al.* [79] showing the hole transfer from illuminated quantum dots into graphene.

However, the interaction of a plasmonic particle with graphene is most likely determined by a combination of both effects the dielectric interaction and the hot carriers injection. The combination of these effects has been supported by several publications [72, 73, 76]. In chapter 5, the experiments focusing on the gold nanorod interaction with graphene and attempting to distinguish between possible interaction pathways will be discussed.

### 3 SAMPLE PREPARATION

In this chapter the preparation of samples will be discussed. First, we describe the growth of epitaxial graphene on silicon carbide (Section 3.1). This is followed by a description of the mechanical exfoliation of graphene (Section 3.2), and the thickness measurement technique (Paragraph 3.2.1). Graphene layers prepared by these procedures will then serve as a substrate for gold nanorods. The gold nanoparticles can be directly deposited from their colloidal solutions on graphene according to the procedure developed by Quintana *et al.* [80]. However, this method was not used in this work as it is not straightforward and, consequently, it leads to deterioration of graphene electronic properties. Therefore, a different approach for gold nanorods deposition was chosen (Chapter 3.4). First, gold nanorods were deposited onto a glass substrate and later on transferred onto graphene.

#### 3.1 Growth of epitaxial graphene

The epitaxial growth of graphene by thermal decomposition of silicon carbide is based on annealing of the SiC substrate at high temperatures leading to evaporation of silicon atoms from the surface [81]. The vapor pressure of silicon is higher in comparison with carbon at a given temperature, enabling silicon atoms to evaporate layer-by-layer while carbon atoms form the graphene layer. There are more than 200 crystallographic configurations of SiC, but for the graphene growth by thermal decomposition 4H-SiC(0001) and 6H-SiC(0001) polytypes are the most appropriate ones. It is worth mentioning, that in this thesis the epitaxial graphene growth is performed on the Si-terminated face of SiC.

The graphene growth was carried out in a home-made furnace of the M2N group at TU/e [82]. After inserting SiC wafers ( $5 \times 5 \text{ mm}^2$ ) into the furnace the degassing of samples was done at a temperature of 825 °C in vacuum. The process of graphene growth consists of two steps (Fig. 3.1). The first step is the etching of a SiC substrate at 1550 °C in hydrogen atmosphere at a pressure of 1000 mbar. This step removes surface defects and impurities. During the hydrogen etching, an oxide layer and several layers of SiC are etched away, leaving the wafer surface atomically smooth and reconstructed into highly uniform terraces. The orientation of terraces and their width depend on the mis-orientation cutting angle with respect to the (0001) crystallographic plane.

The second step is a graphene growth itself (Fig. 3.1). During the growth, the etched SiC wafers are annealed at high temperature either in an vacuum or in argon atmosphere. In the case of annealing in vacuum the resulting graphene samples have low uniformity and contain lots of defects randomly distributed over the surface. The

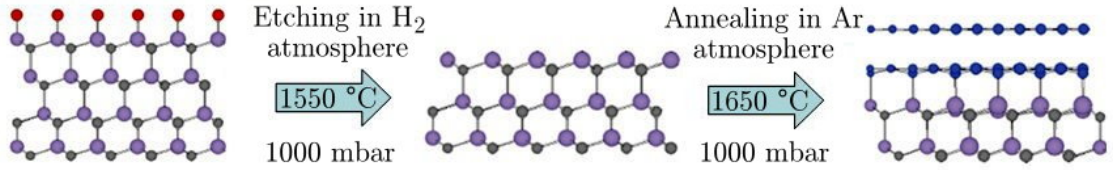


Fig. 3.1: The schematic illustration of the epitaxial graphene growth on a SiC substrate by thermal annealing. Hydrogen etching of SiC results in removing several SiC layers and the oxide layer. Then, graphene is grown on the top of etched SiC by annealing in argon atmosphere. Gray, violet, red and blue spheres indicate carbon, silicon, oxygen and carbon atoms forming graphene, respectively. Taken from [83].

quality of epitaxial graphene can be significantly improved by performing the annealing step at a high pressure in an argon atmosphere. The presence of argon results in the lowering of the silicon evaporation rate, therefore the growth temperature can be increased up to 1650 °C. The higher temperature enhances the diffusion of carbon atoms at the surface and therefore the surface is reconstructed before the graphene layer is finished. Hence, such samples exhibit remarkably improved morphology with wide, straight and continuous terraces of graphene [83–85].

During the growth process a buffer layer is formed in between the SiC substrate and the graphene layer (see the right part of figure 3.1). This buffer layer consists of an unfinished graphitic layer connected to the SiC substrate by several covalent bonds, but its important feature is the dangling bonds arising from the silicon atoms in first SiC layer and pointing directly into the graphene. These silicon dangling bonds act as a strongly localized scattering centers for carriers in graphene and thus heavily influence the electronic properties of epitaxial graphene [86].

The presence of graphene on the top of a silicon carbide wafer is verified by the Raman spectroscopy. In the case of epitaxial graphene on silicon carbide the Raman spectrum is significantly influenced by the underlying SiC. Therefore, the Raman spectra of SiC needs to be recorded separately and then subtracted from the measured spectrum of the epitaxial graphene [87]. Such a spectrum is depicted in figure 3.2. The measured spectras show graphene of a good quality which is apparent from the low intensity of the D-peak positioned at  $\sim 1340 \text{ cm}^{-1}$ . The intensity of this peak is related to the number of the defects in the graphene layer [88].

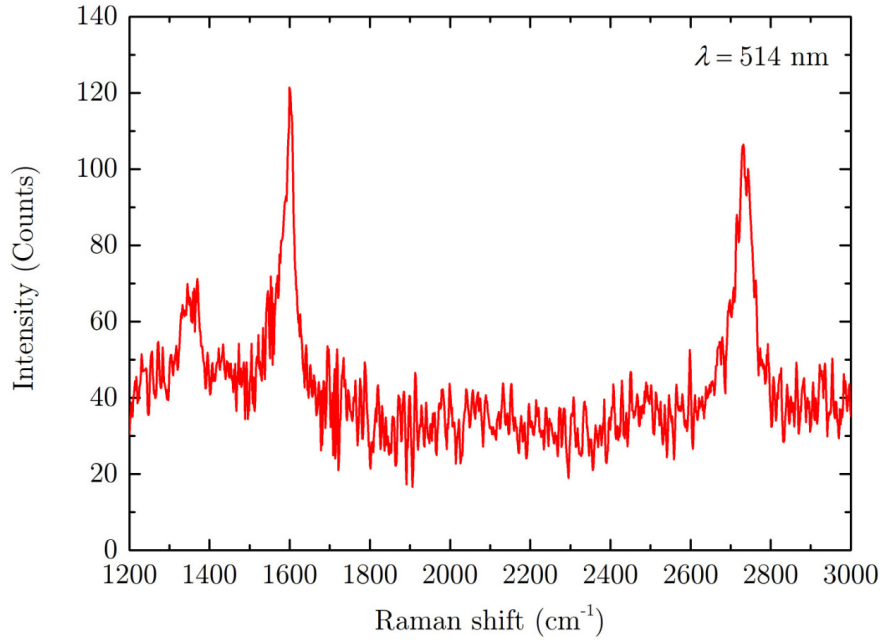


Fig. 3.2: Raman spectrum of pure epitaxial graphene grown on SiC. The measurement was performed by *Renishaw inVia* setup, using an excitation laser with the wavelength 514 nm and the integration time was 10 seconds. First the spectrum of graphene grown on SiC was recorded and subsequently the spectra from the SiC substrate was measured and subtracted from the former one, providing thus the Raman spectrum of pure epitaxial graphene.

## 3.2 Exfoliating of graphene

The second approach for graphene preparation used in this thesis is its mechanical exfoliation. This different method was introduced due to unexpected optical behavior of epitaxial graphene and silicon carbide in single particle scattering optical spectroscopy, discussed in detail in section 5.3. This method was developed by Geim and Novoselov during their groundbreaking experiments resulting into the graphene discovery [4–6]. They used a *Scotch* tape to gently peel off one atomic graphene layer from bulk graphite and then transferral it onto a different substrate. Due to ease of production, low cost and high quality of prepared graphene layers, the exfoliation of graphite is currently the most popular route to prepare graphene.

The exfoliation method entails the repeated peeling of small islands (called flakes) of graphene from highly oriented pyrolytic graphite (HOPG), using cellophane tape. By repetition of the peeling step, the graphite becomes thinner ideally resulting in one atomic-thick graphene layer. This method produces graphene flakes with a variety of layer numbers, where monolayers are in a great minority compared to

thicker ones. On the other hand the single graphene layers are most likely single-crystalline and show up high quality properties enabling to use them mostly for fundamental studies. The dimensions of flakes range in scale of tens micrometers. The big disadvantage of this method is that the prepared samples usually contain impurities from the adhesive tape. The protocol given for this graphene preparation method is given in Appendix A.

### 3.2.1 Flake thickness determination

Graphene is relatively straightforward to make, but not so easy to find. However, graphene can be quite easily visualized optically [89] due to its wavelength dependent complex refractive index (Fig. 1.5). When graphene is placed on the 300 nm thick SiO<sub>2</sub> layer on Si substrate, the graphene flakes become visible in white light illumination due to interference [89]. This method serves as a tool for finding promising single-atomic graphene flakes due to their characteristic color [89] and by measuring the contrast or reflection the number of layers up to 10 can be roughly determined [90]. Nevertheless, in this work it was impossible to measure the flake thickness by the interference because the flakes were directly deposited on opaque glass without any reflection layer.

Another optical method useful for determination of graphene thickness is Raman spectroscopy, which recently proved itself as a powerful tool for distinguishing graphene monolayers [88]. The graphene 2D Raman peak is sensitive to the number of graphene layers [88,91]. However, these measurements are extremely time consuming - for instance getting a Raman map of a flake with dimensions  $\sim 20 \times 80 \mu\text{m}^2$  requires more than 24 hours - and subsequent data processing relies on fitting many different peaks and parameters.

The measurement of optical transmittance through multilayer graphene in the visible spectrum provides a simple way to determine the number of graphene layers. There are several works dealing with graphene transmittance as a function of number of graphene layers both theoretical [92] and also experimental ones [19,21]. Nair *et al.* [19] argued that every single layer of graphene decreases the light transmittance by 2.3 %, resulting thus in a linear dependence of transmittance on number of graphene layers. This dependence was then corrected by Zhu *et al.* [21] as described by equation 1.5 and verified by various experiments [21].

The optical transmittance measurement serves as a simple, fast, highly reliable method enabling to determine many different graphene flakes on different places across the sample. This method relies only on a common optical microscope equipped with a reliable CCD camera to precisely measure the intensity of the transmitted light. Therefore, this setup was used in this work for the flake thickness determination

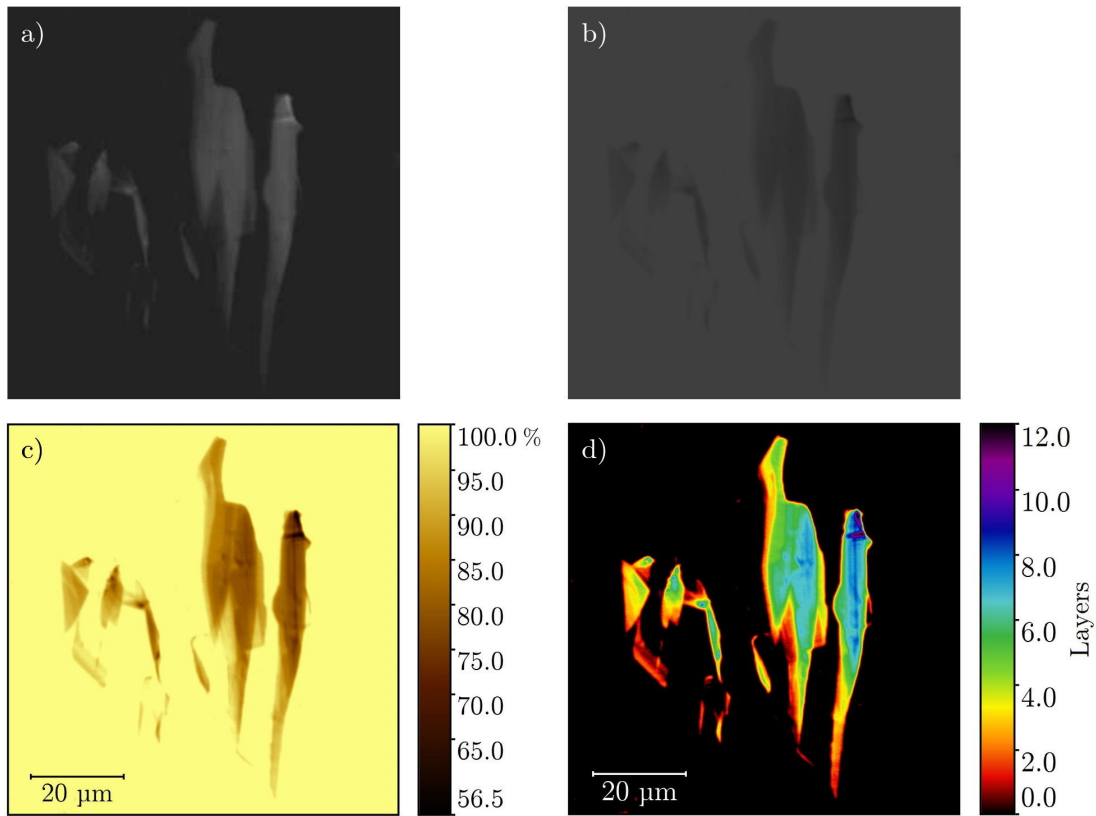


Fig. 3.3: The procedure of graphene flake thickness determination by measuring the optical transmittance through the flake. a) *Step 1*: identification of promising flake in the reflection illumination configuration. b) *Step 2*: recording of the light intensity profile of selected flake under the transmission illumination. c) *Step 3*: calculation of light transmittance map. d) *Step 4*: the number of graphene layers calculation from light transmittance using the equation 1.5.

and proceeded as follows: According to performed calculations using the Fresnel model the graphene flake contrast on BK7 glass substrate is noticeably higher for reflection illumination compared to transmission one. Hence, first the flakes suitable for further experiments were identified using reflection illumination (Fig. 3.3a) and their coordinates were written down for the following step. In this second step, the transmission illumination was used to record the light intensity map (Fig. 3.3b). Further, the intensity map was recalculated using a simple SPM data processing software to obtain the light transmittance map (Fig. 3.3c). In the last step the light transmittance through the graphene flake was recalculated using equation 1.5 to get a map with the number of graphene layers in the flake (Fig. 3.3d). Figure 3.3 shows the whole procedure of graphene flake thickness determination step by step.

### 3.3 Gold nanorods

In this thesis, three different types of gold nanorods are discussed, all of them grown by a seed-mediated method [93,94] and purchased from start-up companies [95,96]. These particles will be referred to in this thesis as NR-10-700 (*Nanopartz*, original name A12C-10-700), NR-20-700 and NR-40-650 (*NanoSeedz*), where NR is the abbreviation for the nanorod, the first number is the diameter of the rod in nm and the second one is the ensemble averaged longitudinal LSPR wavelength in nanometers. Parameters of the gold nanorods can be found in table 3.1. Since the seed-mediated growth yields gold nanorods with a size distribution, the parameters in table 3.1 corresponds to the average values over the nanorod ensembles.

Tab. 3.1: The parameters provided by the manufacturers of commercial gold nanorods used in this thesis [95,96].

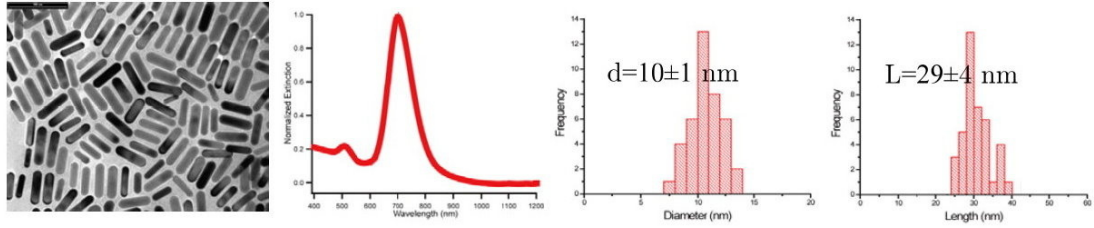
Name	Manufacturer	Diameter (nm)	Length (nm)	Aspect ratio	TP (nm)	LP (nm)
NR-10-700 (A12C-10-700)	<i>Nanopartz</i>	10	29	2.9	508	700
NR-20-700	<i>NanoSeedz</i>	20	51	2.5	512	700
NR-40-650	<i>NanoSeedz</i>	40	84	2.1	522	650

In figure 3.4 transmission electron microscopy (TEM) images of three mentioned nanorod samples, corresponding absorption spectra of nanorods in a colloidal solution and histograms of the size (diameter and length) distribution are shown. The nanoros sizes and longitudinal surface plasmon resonance are ensemble average, where each rod has an individual size and aspect ratio, which corresponds to a specific LSPR wavelength and peak linewidth. This distribution in size makes it essential to measure the spectras of single particles in gold nanorod - graphene interaction experiments (Chapter 5) to get reliable results.

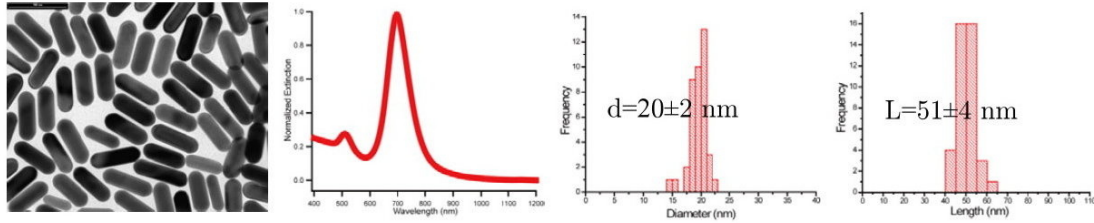
### 3.4 Deposition of gold nanorods

Direct functionalization of graphene by covalent linking to gold nanoparticles disrupts electronic states of graphene which is highly undesirable. We therefore took a different approach for immobilization of colloidal gold nanoparticles on graphene. At first the colloidal gold nanoparticles are deposited on a glass substrate and then subsequently transferred onto graphene. In the following sections this process is described.

NR-10-700



NR-20-700



NR-40-650

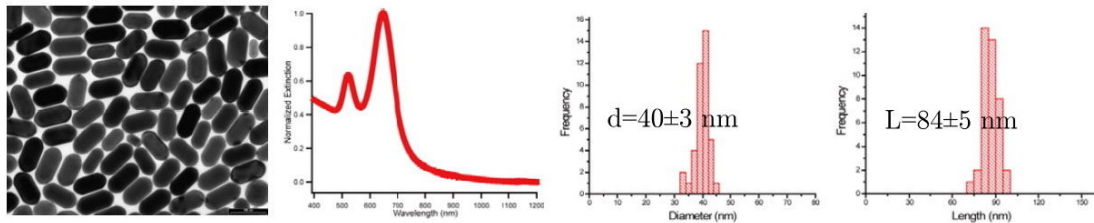


Fig. 3.4: TEM images, absorption spectras and length and width distributions of gold nanorods discussed in this thesis. Adapted from [95,96] and edited.

### 3.4.1 Glass functionalization

Gold nanorods prepared by the seed-mediated growth [94] are capped by a cetyltrimethylammonium bromide (CTAB) bilayer enabling further functionalization of nanorods and preventing them from clustering in the colloidal solution. Also, the presence of CTAB makes gold nanorods positively charged due to its ammonium groups pointing outwards [97]. Since gold nanorods are positively charged, the negative charge needs to be created on target substrate to enhance their deposition there. Therefore, glass appears itself as an ideal substrate because its surface can be easily chemically modified and also it is optically transparent and inexpensive. The negative charge on glass substrate can be created by applying UV/ozone treatment. This cure charges the surface of glass by creation of negatively charged -OH groups. These groups can then be used either for direct nanorods deposition or as a platform for creation of a self-assembled monolayer (SAM) of molecules with a thiol group that can covalently bind to the gold.

Molecules used for the SAM formation are thiosilane compounds [98], in case

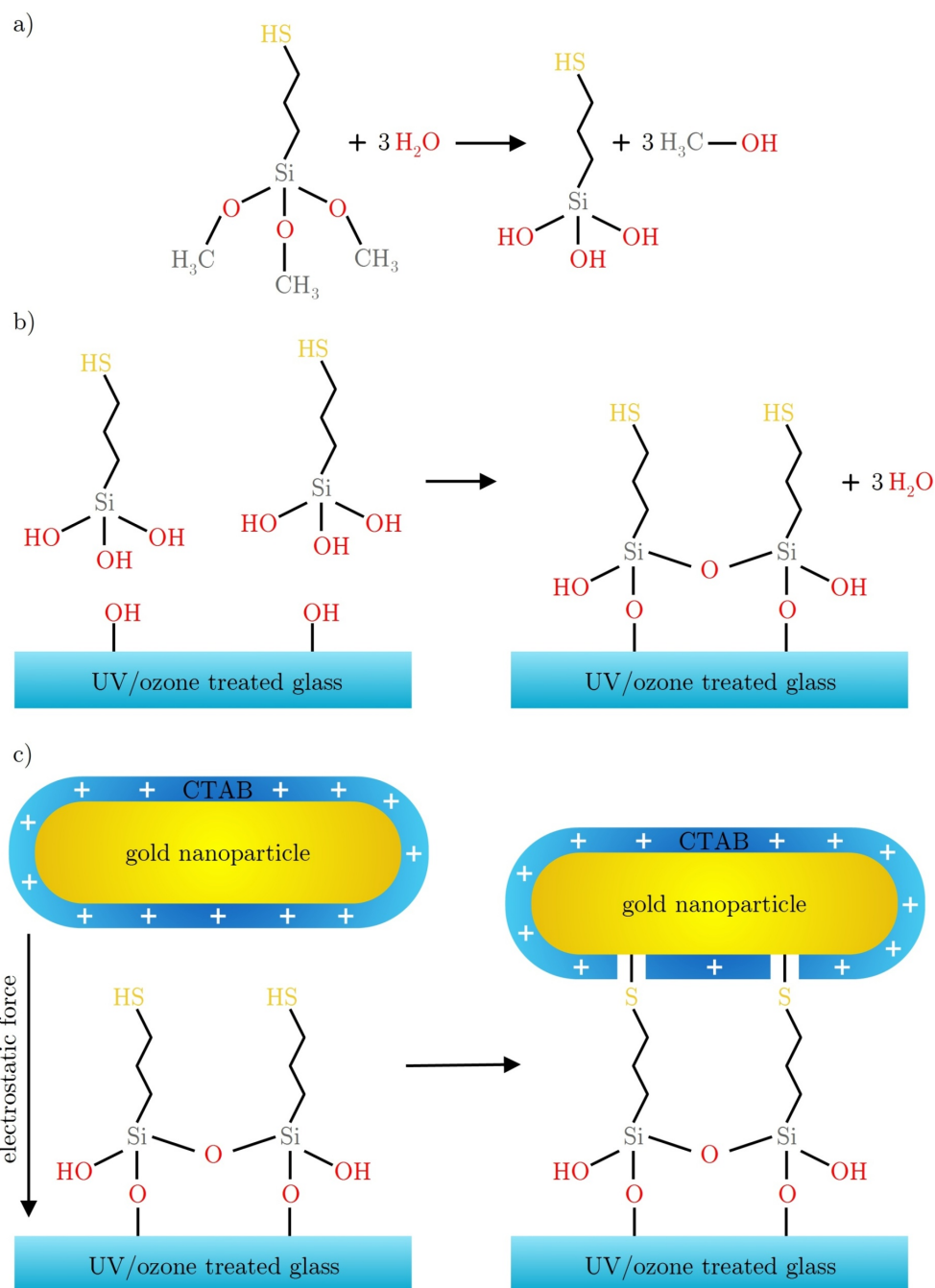


Fig. 3.5: The mechanism of gold nanorods immobilization from solution on a mercaptosilane-modified glass substrate. a) The activation of MPTMS by trace water molecules in ethanol, where the methoxy groups react with water to form hydroxyl groups. b) The hydroxyl groups of the activated MPTMS form covalent bonds with hydroxyl groups on the glass surface and neighbouring MPTMS molecules form a negatively charged SAM on the glass surface, where sulphur carries the net-negative charge. c) The gold nanoparticle is attracted towards the glass due to an electrostatic force between a positively charged CTAB capping layer and negative SAM on the glass surface. When close enough the thiol group of the covalently bound MPTMS binds to the gold nanoparticle (not to scale).

of this work (3-mercaptopropyl)trimethoxysilane (MPTMS), where the thiol group (-SH) carries a negative charge. The use of MPTMS ensures both the creation of negatively charged SAM electrostatically attracting gold nanorods and, when close enough, the thiol group binds covalently to the gold nanoparticles keeping them firmly in place [99].

The creation of MPTMS self-assembled monolayer is depicted in figure 3.5. The glass slides need to be cleaned thoroughly by UV/ozone treatment<sup>1</sup> to activate the hydroxyl (-OH) groups on the glass surface. The methoxy groups (-O-CH<sub>3</sub>) of the MPTMS are first activated when reacting with trace water molecules in the ethanol and thus form hydroxyl groups. The hydroxyl groups of the MPTMS bind to other MPTMS hydroxyl groups and to hydroxyl groups on the UV/ozone treated glass surface, forming a monolayer over the substrate surface.

The deposition of gold nanorods on MPTMS modified glass substrates was performed as follows: The glass slides 22 × 22 mm<sup>2</sup> (Menzel-Gläser) were sonicated in methanol for 20 minutes and blown dry with nitrogen. Then the UV/ozone treatment was used for 90 minutes to create hydroxyl groups on the glass surface. Immediately after UV/ozone cleaning the coverslips were incubated in a MPTMS ethanol solution to create negatively charged SAM. Afterwards, the glass slides were rinsed with methanol, sonicated in methanol for 20 minutes and blown dry with nitrogen. Finally, the gold nanorod colloidal solution was applied onto as-prepared mercaptosilane-modified glass slides.

There are several possible ways of gold nanorods deposition from a colloidal solution application on an as-prepared glass substrate. Here, in this thesis, two different possibilities are shown. The first one, enabling the fast deposition but giving a low gold nanorod coverage, is the spin-coating of the colloidal solution onto the glass substrate. The second one, giving high and controlled gold nanorod coverage on the glass substrate but unfortunately time-consuming is a direct full immersion of mercaptosilane-modified glass slides into the bulk colloidal solution. Both of these methods are thoroughly described in the following paragraphs.

### 3.4.2 Spin-coating deposition

For single-particle scattering microscopy described in chapter 5 low coverage of a glass substrate by particles is needed. For this purpose the separation between particles needs to be more than 1 μm allowing only one particle present in the focal

---

<sup>1</sup>Also the piranha treatment can be used for the creation of hydroxyl groups on the glass surface. Unlike the UV/ozone treatment, piranha treatment gives better and more uniform coverage of glass surface with hydroxyl groups. The big disadvantage of piranha is its hazards, which make working with piranha extremely dangerous.

spot of an objective. To achieve such a nanorod coverage a spin-coating drop of the gold nanorod colloidal solution onto mercaptosilane-modified glass coverslips is used. The spin-coating procedure typically produces the samples with well-dispersed gold nanoparticles with an average spacing varying between 2 and 10  $\mu\text{m}$  (the obtained spacing depends on wettability of the substrate, degree of silanization, nanoparticle concentration and spin-coating parameters) [58].

The deposition procedure protocol is given in Appendix A. After spin-coating each coverslip was rinsed with phosphate buffered saline (PBS) and distilled water to rinse off CTAB micelles and impurities. Additionally coverslips with already deposited gold nanorods were again treated by UV/ozone to get rid off the CTAB coating from gold nanorods. The gold nanorod deposition using spin-coating was applied on both the mercaptosilane-modified glass slides and only UV/ozone treated coverslips. Surprisingly, both substrates yielded a similar nanorod coverage. The experiments using samples without thiol compounds were carried out to avoid contamination of gold nanorods with any useless molecules covalently bounded to a gold nanorod.

### **3.4.3 Deposition from bulk solution upon coverslip immersion**

The photodetection experiments (Chapter 4) on the other hand need to be realized with graphene samples highly covered by nanoparticles. This can be achieved by a full immersion of MPTMS modified glass coverslips into the bulk colloidal solution. However, to get the desired coverage by nanoparticles, the optimization of the whole deposition procedure needed to be done. The parameters which could be optimized were: MPTMS concentration in an ethanol solution, immersion time in MPTMS ethanol solution, deposition time in gold nanorods colloidal bulk solution and concentration of CTAB in this solution. The UV-Vis spectras of prepared samples give us a reliable information about the coverage of glass slides by the nanoparticles by monitoring the absorption peak height. Therefore, this technique was further used during the process of parameterization.

We first varied the MPTMS concentration in ethanol with the aim to vary the density of thiol groups on the coverslip surface. The MPTMS concentration in ethanol was varied from 5 % to 20 %, namely 5 %, 10 % and 20 %. The results are shown in the figure 3.6. Note that the values of other parameters in this case were: immersion time in the MPTMS ethanol solution 15 minutes, concentration of CTAB in the bulk solution 0.15 mM and the deposition time 1 day. According to the shown results it is clear that the concentration of MPTMS in ethanol is not the crucial parameter of gold nanorod deposition. Therefore the concentration of 5 % MPTMS in the ethanol solution was selected for the final deposition protocol.

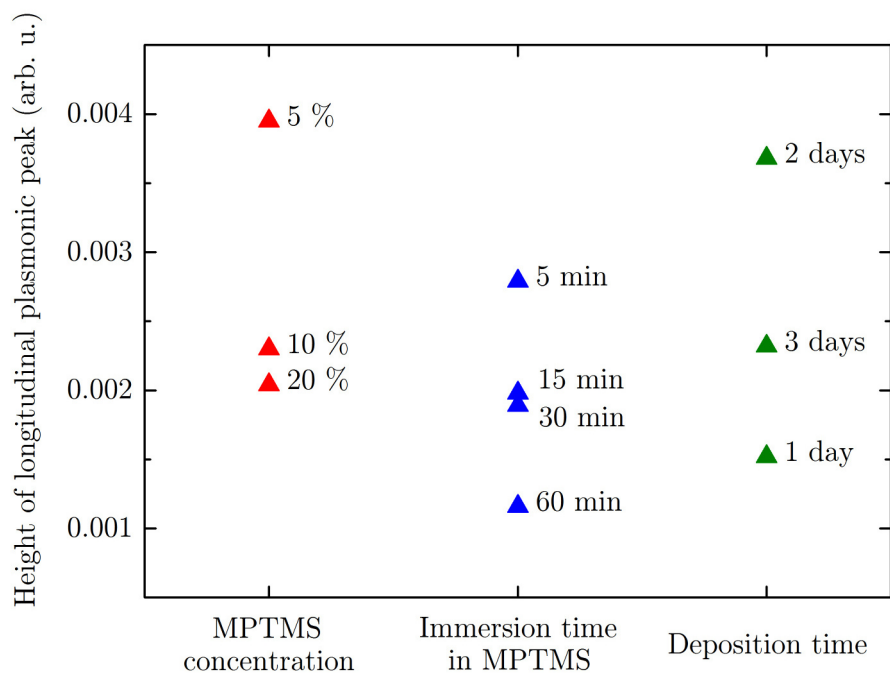


Fig. 3.6: Parameterization of gold nanorod deposition process: The height of the longitudinal plasmonic peak of gold nanorods extracted from UV-Vis spectra as a function of the MPTMS concentration in ethanol (red triangles), the immersion time in the MPTMS ethanol solution (blue triangles) and the deposition time in the gold nanorods bulk solution (green triangles). The values of other parameters in the case of varying the MPTMS concentration in ethanol were: immersion time in the MPTMS ethanol solution - 15 minutes, concentration of CTAB in the bulk solution - 0.15 mM and the deposition time - 1 day. Moreover in the case of varying the immersion time in the MPTMS ethanol solution the MPTMS concentration in ethanol was 10 %. In the case of varying the deposition time in the gold nanorod bulk solution: the MPTMS concentration in ethanol - 5 %, the immersion time in MPTMS the ethanol solution - 5 minutes and the concentration of CTAB in the bulk solution - 0.07 mM.

The next optimized parameter of gold nanorod deposition on glass is the immersion time of glass slides in the MPTMS ethanol solution. The immersion time was varied from 5 minutes up to 1 hour, namely 5, 15, 30, 60 minutes. The measured results can be seen again in figure 3.6. Again, one can clearly see almost no dependence of deposition efficiency on the varying of the immersion time in the MPTMS ethanol solution (Fig. 3.6). Anyway, the curve of immersion time of 5 minutes showed the best gold nanorods coverage of the sample. Therefore, the immersion time in the MPTMS ethanol solution was selected to be 5 minutes for the final deposition protocol.

The next optimizable parameter of gold nanorod deposition on mercaptosilane-modified glass slides was the deposition time during which the glass slides were immersed in the bulk colloidal solution. The time of deposition was varied namely 1, 2, 3 days. The values of other parameters were: the MPTMS concentration in ethanol 5%, the immersion time in the MPTMS ethanol solution 5 minutes and the concentration of CTAB in the bulk solution 0.07 mM. According to the previous text and other used parameters one would expect the efficiency of deposition to be determined only by the time during which the slides were immersed in the bulk solution. From figure 3.6 it is clear that this statement is far from the truth - the corresponding results show no clear dependence.

Another optimizable parameter was the CTAB concentration in the gold nanorod bulk colloidal solution. It is worth noting that the CTAB concentration parameter includes all CTAB molecules which cover the nanorods' surface and also all CTAB molecules and micelles freely dispersed in the bulk solution. The concentration of CTAB was varied from 5 mM to 0.03 mM, the values were namely: 5, 0.5, 0.15, 0.07 and 0.03 mM. The corresponding results can be seen in figure 3.7. The values of other parameters in this case were: MPTMS concentration in ethanol 5 %, the immersion time in MPTMS ethanol solution 5 minutes and the deposition time - 1 day.

From the measured UV-Vis absorption curves depicted in figure 3.7 one can clearly see that the CTAB concentration in the colloidal bulk solution is the crucial parameter for efficient gold nanorod deposition on mercaptosilane-modified glass substrates. The curves representing CTAB concentrations of 0.15 mM and 0.07 mM show clearly recognizable longitudinal plasmon peaks. However, for all the remaining curves there are no plasmon peaks at all. This is in agreement with a critical concentration of CTAB in gold nanorods bulk solution, which value is around 0.1 mM [100]. This means that for the CTAB concentration lower than  $\sim 0.1$  mM the gold nanorod tend to cluster. Such a clustering is observed for the curve of 0.03 mM CTAB concentration, where an enhanced absorption is present in the red part of the spectra. On the other hand there is no significant feature for the CTAB concentration of 5 mM and 0.5 mM. We believe that this behavior can be explained by the presence

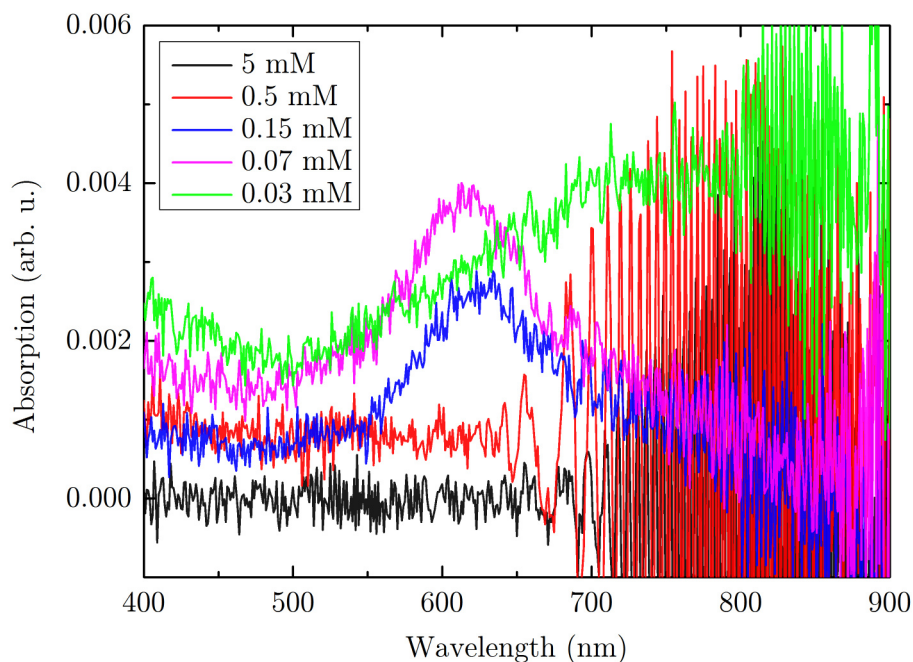


Fig. 3.7: UV-Vis spectras of deposited gold nanorods on glass slides: the dependence of the gold nanorod coverage of a glass slide on the CTAB concentration in a gold nanorod bulk solution. The CTAB concentration parameter includes all CTAB molecules which cover the nanorods surface and also all CTAB molecules and micelles freely dispersed in the bulk solution. The values of other parameters of gold nanorods deposition were: MPTMS concentration in ethanol - 5 %, the immersion time in MPTMS ethanol solution - 5 minutes and the deposition time - 1 day.

of freely dispersed CTAB molecules and micelles in the gold nanorod bulk solution. Most likely the thiol groups can not bind to the gold due to shielding caused by CTAB.

Therefore, the earlier reported independence of gold nanorod deposition efficiency on the deposition time can be explained by the presence of freely dispersed CTAB molecules and micelles in colloidal bulk solution. These molecules are attracted by the negatively charged SAM and create a shielding layer preventing the continuation of the gold nanorod deposition.

For enhancing the gold nanorod coverage of a glass substrate the disruption of formed the CTAB shielding layer on the substrate is necessary. This disruption can be done by rinsing the sample by a high ionic strength buffered solution, such a PBS. Such a rinsing with PBS causes washing off the electrostatically bound free CTAB molecules and micelles, but also only electrostatically bound nanorods. The

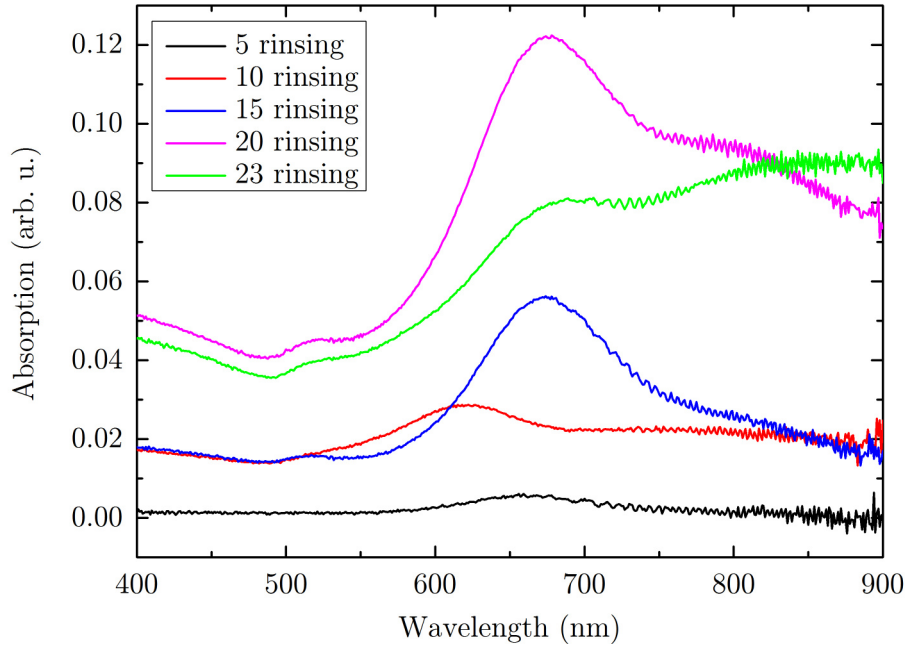


Fig. 3.8: Dependence of the gold nanorod coverage of mercaptosilane-modified glass slides on the number of rinsing cycles. The period between each rinsing was 20 minutes. This rinsing disrupts the CTAB shielding layer on the mercaptosilane-modified glass surface, enabling thus a further deposition of gold nanorods. Note that in the case of the red curve (10 rinsing) the old gold nanorods possessing a different position of the plasmon peak were used.

PBS residues were washed off by distilled water, this rinsing of glass coverslips was repeated every 20 minutes. The dependence of gold nanorods coverage on the number of rinsing cycles is depicted in figure 3.8. It is obvious that the density of coverage increases with the number of rinsing cycles.

Let us focus on figure 3.8: The green curve (23 rinsing) is a typical example of the sample with clustered nanorods, there is a clear evidence of enhanced absorption in the red part of spectrum. This feature, so significant for clustering, is present also in the case of the purple curve (20 rinsing) but not in such a big presence. In this case the plasmon peak is still significant showing that the clustering is not critical. Note that in the case of the red curve (10 rinsing) the different (old) gold nanorods possessing a different position of the plasmon peak were used. It was found that after  $\sim 15$  rinsing of slides the clustering started to appear. This can be explained by the decreasing of the CTAB concentration in the bulk colloidal solution due to the rinsing off free CTAB molecules from glass slides and subsequent lowering of

the CTAB concentration in bulk solution under the critical value ( $\sim 0.1$  mM), and thus the clustering of gold nanorods. To overcome a clustering of nanorods the bulk colloidal solution was fully exchanged after 12 rinsing steps of glass slides.

### 3.4.4 Transfer of gold nanorods onto graphene

Since the gold nanorods are effectively immobilized on the glass substrate, their transfer onto graphene needs to be performed. The method used in this work entails the covering of gold nanorods with poly(methyl methacrylate) (PMMA) and subsequent peeling-off this layer with gold nanorods from the source glass substrate. The peeling-off is achieved by immersing the PMMA structure into a basic solution (0.1 mM KOH in distilled water), wherein a slight hydrolyzation of PMMA occurs [101]. The peeled PMMA / gold nanorod layer then flows on the surface of liquid and can be transferred to a new target substrate, namely graphene. There the PMMA can be dissolved by organic solvents.

The PMMA layer was created on the gold nanorods-immobilized glass slides by spin-coating. Three different types of PMMA, different in the length of polymer chains, were tested - 995k PMMA, 120k PMMA and 15k PMMA. It was found the PMMA layer needs to have a desired thickness not to be torn during the immersion in KOH. The table 3.2 shows the minimal thicknesses of the PMMA film for the successful transfer of gold nanorods from the source glass substrate. These thicknesses were measured using the *Dektak XT* profilometer and were determined to be  $\sim 120$  nm for 995k PMMA and  $\sim 330$  nm for 120k PMMA. In the case of the 15k PMMA the created film was torn after immersion into KOH for every thicknesses up to 1  $\mu\text{m}$ . This could be caused by the short molecular chains of 15k PMMA, which are unable to create a sufficiently interwoven polymer network.

Tab. 3.2: The parameters of the gold nanorod transfer from the source glass slide onto atarget graphene substrate according to the used PMMA type.

PMMA type	Molecular weight thickness (Da)	Minimal film (nm)	Transfer efficiency
995k PMMA	995 000	$\sim 120$	60 %
120k PMMA	120 000	$\sim 330$	95 %
15k PMMA	15 000	$> 1000$	X

After spincoating the PMMA layer the sample was immersed in a KOH bath for 2 hours. After peeling-off the floating PMMA / gold nanorods layer was manually transferred into distilled water bath. There the layer was cleaned from remaining KOH for 1 hour. Then the PMMA / gold nanorods layer was transferred onto the

target substrate containing graphene. It was found that for the better stretching of PMMA / gold nanorods layer on the graphene surface the heating of the sample at 50 °C for 10 minutes was applied. Subsequently the PMMA was dissolved in acetone or chloroform [102] overnight. For single-particle scattering microscopy experiments described in chapter 5 another step was added into the transfer procedure. After peeling off the PMMA / gold nanorods layer in the KOH bath, the layer was transferred into a salt solution (NaCl - 1 M) bath to get rid of the remaining CTAB molecules from gold nanorods.

The efficiency of the transfer was determined by measuring the longitudinal absorption peak of the samples before and after the transfer. The corresponding values for both types of PMMA are also shown in table 3.2. The transfer process using 995k PMMA exhibits an efficiency of 60 %. This low number is most probably the consequence of the long polymer chains of 995k PMMA. These long molecules are unable to wrap around nanorods efficiently, thus a significant amount of gold nanorods is lost during the process. Therefore, the PMMA with shorter molecules should give better results because polymers should be better wrapped around the gold nanorods. Indeed, the measured transfer efficiency increases to 95 %. Thus the 120k PMMA was selected for the final protocol of the gold nanorod transfer from the glass source substrate onto a target graphene. The protocol for the transfer of gold nanorods onto graphene can be found in Appendix A.

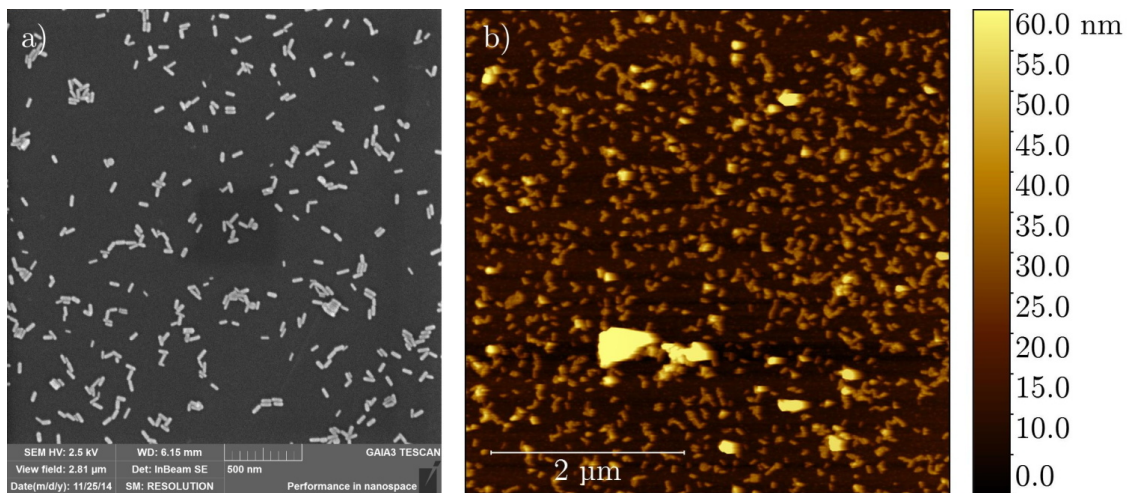


Fig. 3.9: a) SEM and b) AFM topography images of the gold nanorods transferred onto epitaxial graphene on silicon carbide. The SEM measurements were performed with assistance of Ing. Rostislav Váňa using the *TESCAN GAIA3* microscope. The AFM measurements were performed using *Veeco Nanoscope Multimode AFM* in the tapping mode using the highly doped silicon tips (*PPP-NCHR*) purchased from *Nanosensors Company*.

Just to give an information how the prepared epitaxial graphene samples with the gold nanorods on its surface looked like, a scanning electron microscope (SEM) and an atomic force microscopy (AFM) measurements were performed. The obtained results are shown in figure 3.9. The original gold nanorod sample was prepared according the above mentioned deposition method (Paragraph 3.4.3) and the number of the applied PBS rinsing cycles was 20 (purple curve in figure 3.8). These samples correspond to that ones which were later used for photodetection experiments performed and discussed in detail in the following chapter 4.

## 4 PHOTODETECTION

Various designs and architectures of photo-devices based on graphene have been already proposed. The simplest configuration is a metal-graphene-metal design, in which graphene is contacted with metal electrodes acting as the source and drain. This architecture is easy to fabricate because it does not rely on nanoscale lithography. In this configuration the device operates over a broad wavelength range as the interaction between light and matter is mainly determined by graphene itself.

Since the electrodes are fabricated from a metal, it is necessary to know how the metal presence affects the graphene. If metal gets into contact with graphene, there are two possible ways of bond creation between these two materials [35,36]. The first one is the chemical interaction, where the covalent bond between metal and graphene is established and thus perturbation of the graphene electronic structure is created. The second type of the interaction is the physisorption. Here the metal is bounded to graphene predominantly by van der Waals forces causing no graphene electronic state disruption. However, the work functions of graphene ( $W_G = 4.48$  eV [35]) and of most metals are different. It gives rise to an equilibrium charge transfer at the metal - graphene interface resulting in doping of the graphene sheet. In general, there is an electron transfer to (from) the metal pad causing the moving of the Fermi level downward (upward) from the graphene conical Dirac points. Therefore, this behavior can be viewed as a doping of graphene with holes (electrons).

The sign and magnitude of graphene doping depend on the type of metal. According to calculations performed in references [35,36] the doping of graphene layer caused by a physisorbed metal is n-type for Al, Ag, Cu and p-type for Au and Pt. The magnitudes of graphene doping caused by these metals are shown in table 4.1. To create a proper doping profile in graphene enabling efficient photocurrent creation and harvesting, at least two different metals need to be used for contacting. From table 4.1 one can clearly see that the most suitable combination of metals for electrodes is Al and Pt.

Tab. 4.1: Calculated work functions of the clean metal surfaces  $W_M$ , free-standing graphene and five metals with absorbed graphene  $W$ . In the last row the Fermi-level shifts  $\Delta E_F$  caused by interaction between metal and graphene are shown. The calculations were performed in [35, 36].

	<b>Graphene</b>	<b>Al</b>	<b>Ag</b>	<b>Cu</b>	<b>Au</b>	<b>Pt</b>
$W_M$ [eV]	-	4.22	4.92	5.22	5.54	6.13
$W$ [eV]	4.48	4.04	4.24	4.40	4.74	4.87
$\Delta E_F$ [eV]	-	-0.57	-0.32	-0.17	0.19	0.33

The configuration and the materials of electrodes are known, but the distance between the electrodes has to be determined. There are two competitive factors dealing with the distance between the electrodes: harvesting most of created carriers and covering the smallest possible area of graphene with electrodes. Considering the fact that almost no photocurrent is created under the metallic contacts [13,37,38] a proper trade-off between these factors should ensure the highest possible efficiency of the graphene photodetector.

The build-in field created by the metallic contacts extends approximately  $0.2 \sim 0.3 \mu\text{m}$  into the metal-free graphene [13]. On the other hand, the exciton diffusion length in highly doped graphene is approximately  $L_D \approx 15 \sim 70 \text{ nm}$  and for the low-doped graphene the exciton diffusion length can reach value a of  $L_D \approx 170 \text{ nm}$  at room temperature [13,103]. Once the exciton is separated into a free electron and hole, the electron mean free path in graphene is  $\lambda_e \approx 400 \sim 600 \text{ nm}$  at room temperature [3]. Therefore, these values limit the desirable distance between electrodes to the maximum value  $L \approx 1 \mu\text{m}$ .

However, the recent research has shown that the photocurrent in graphene is governed by the thermoelectric effect, as discussed earlier (Paragraph 1.3.2). This fact increases a possible value of the distance between the electrodes dramatically. Hot carriers are thermally decoupled from the graphene lattice over the length scale as large as  $\xi \approx 7 \mu\text{m}$  at room temperature [25]. Thus, if the light illuminates the center of the device (considering the focused light with a usual spot diameter of  $1 \mu\text{m}$ ), it gives the maximum possible distance between the electrodes  $L \approx 15 \mu\text{m}$ .

Metals are usually deposited by evaporation from a solid source in ultra-high vacuum. In laboratories of M2N the metal evaporator setup is located in nitrogen atmosphere. Therefore the oxygen-free environment allowed us to use the aluminum electrode and thus suppress its oxidation. Unfortunately, the evaporator did not allow us to deposit platinum, thus a different metal had to be used for the second electrode. According to table 4.1 gold was selected to create the p-doped region in the device. The deposition of electrodes was done using a homemade lithographic mask allowing us to fabricate the metal pads with a thickness of  $70 \text{ nm}$  separated from each other by  $15 \sim 20 \mu\text{m}$ . Note that the created distance between the fabricated electrodes was not homogeneous due to the frayed edges of the created electrodes.

The samples were prepared according to the procedures described in detail in chapter 3. The epitaxial graphene grown on silicon carbide was used for photodetection experiments. The gold nanorods were transferred onto graphene prior to the deposition of the metal electrodes. The electrodes were further contacted using a silver glue in the way preventing a direct contact between silver and graphene. Two different types of photodetectors were prepared: the bare graphene photode-

tector (Fig. 3a) and the graphene photodetector with gold nanorods on the top of graphene (Fig. 3b). Moreover the reference samples consisted of only silicon carbide with gold nanorods on its top and bare silicon carbide were fabricated.

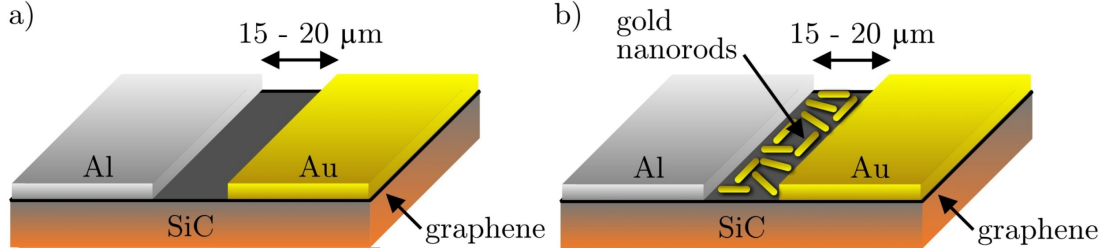


Fig. 4.1: Sample configurations: a) bare graphene photodetector, b) graphene photodetector with gold nanorods on its top. Pictures are not to scale.

## 4.1 Characterization of prepared systems

For understanding of the following photodetection experiments the description of fabricated systems is necessary. The interaction between the metals and graphene leads to a doping of graphene. The electrode made of gold shifts the level of Fermi energy in underlying graphene downwards from the conical point, resulting in a p-doping of 0.19 eV. In the case of the aluminum electrode the Fermi energy level in the underlying graphene sheet is shifted upwards, resulting in a n-doping of -0.57 eV.

Nevertheless, these values correspond to the free-standing graphene [35, 36], where the Fermi energy level is located right in the Dirac point, meaning the zero doping. In the case of epitaxial graphene the presence of the SiC substrate and the intermediate buffer layer causes shifting the Fermi energy level upwards from the conical point giving thus the n-doping of graphene by a value of -0.54 eV [104]. Thus, there are three differently doped regions of graphene in such system. The Fermi energy level is gradually aligned among these three areas and the doping profile is determined by an extension of the built-in field from metal pads into the graphene channel by a value of  $0.2 \sim 0.3 \mu\text{m}$  [13]. This system is depicted in figure 4.2a.

However, by placing gold nanorods onto the graphene surface the well defined system shown in figure 4.2a is significantly changed as depicted in figure 4.2b). The nanorods themselves locally dope graphene positively due to their gold nature. Unlike the gold contact, the nanoparticle does not cover the whole surface of graphene-related area and thus the doping is not homogeneous and it is strictly localized in nanorod surroundings. However, the n-doping in epitaxial graphene on SiC is mainly attributed to the presence of the buffer layer, namely to the silicon dangling bonds

pointing into the graphene sheet [86]. The doping caused by the dangling bonds is also strongly localized. The presence of gold nanorods in vicinity of such dangling bonds can effectively shield them and thus the n-doping of graphene is significantly decreased. However, there is another factor causing additional positive doping of graphene and that is the presence of PMMA residues left on the graphene surface due to the gold nanorod transfer [102].

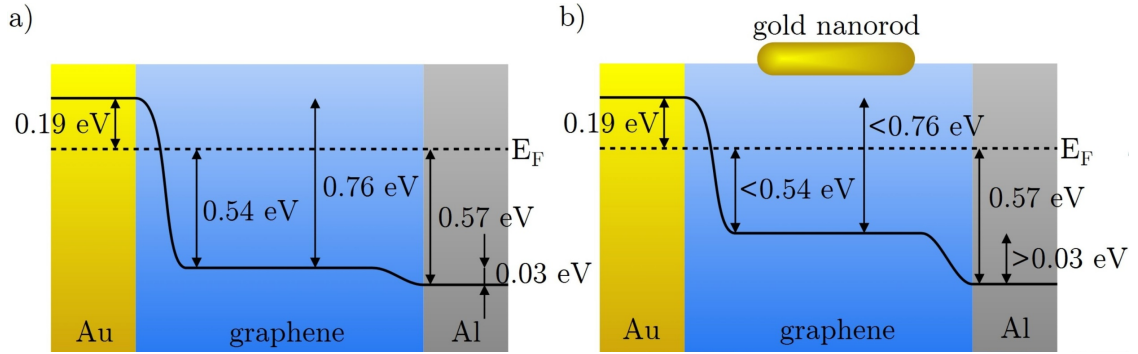


Fig. 4.2: Doping profile of the fabricated systems: a) Gold – epitaxial graphene – aluminum, b) gold – epitaxial graphene with gold nanorods on its top – aluminum. Note that the depicted metal-related regions do not mean the metal itself but the graphene lying under the metal.

## 4.2 Photoresponse measurements

The basic method for characterization of photo devices is the measurement of I-V curves. This method measures the electric current passing through a device as a function of bias voltage applied to device electrodes. To get the desired information about the device photoresponse the I-V measurements are first performed in a dark environment and later on under the illumination of the device. The difference between the current measured under the illumination and the dark current determines the photoresponse behavior of the device.

The I-V measurements carried out in this thesis were performed in a nitrogen atmosphere without any exposure of the samples to ambient conditions. The source of illumination simulated the solar spectrum AM 1.5 (see figure B.1 in Appendix B). First, the I-V measurements of the control samples were performed. The samples consisted of contacted silicon carbide with and without gold nanorods on its surface, both provided with Al and Au electrodes. In both cases only the electrical noise was detected. Therefore, the contribution from the SiC substrate to the photocurrent was ruled out. The obtained I-V measurement results of a graphene photodetector without and with gold nanorods on the top of graphene are shown in figures 4.3

and 4.4, respectively. The measurements were carried out for two distinct wiring configurations of electrodes. In both figures 4.3 and 4.4 the first wiring configuration (upper parts of figures) corresponds to the grounded aluminum electrode and the bias voltage applied to the gold electrode. In the second wiring configuration (lower parts of figures 4.3 and 4.4) the gold electrode is grounded and the bias voltage is applied to the aluminum one. The both samples showed significantly distinct behavior for the different wiring configurations.

First, the I-V measurement results of the bare graphene photodetector (Fig. 4.3) are discussed. The grounded electrode defines the position of the Fermi energy level of the system (see insets of figure 4.3). For the dark measurement related to the grounded aluminum electrode the bias voltage applied on the gold electrode started at -1 V and was increasing. For negative bias voltages the current in the photodetector had to flow through the localized states in graphene causing quite high resistance and, hence, a small slope of the curve was observed. The current started to flow partially through the delocalized states of the system when the applied bias voltage reached the value  $\sim 0.03$  V corresponding to the difference between the value of doping in bare graphene and the doping value of graphene under the aluminum electrode. This led to a decrease of device resistance and thus to an increase of the curve slope. However, even for the bias voltage higher than  $\sim 0.03$  V there was still a part of the device (area under the gold electrode), where the localized states were present. These localized states were fully overcome when the applied bias voltage reached the value  $\sim 0.8$  V. This value corresponds to the difference between the values of graphene doping under the gold pad and that of graphene under the aluminum electrode. Above the bias voltage of  $\sim 0.8$  V the current started to flow only through the delocalized states in the whole device and the resistance was thus abruptly reduced resulting in precipitously increased curve slope.

As for the illuminated device the shape of the I-V curve was significantly changed. The illumination of the bare graphene photodetector caused the creation of hot carrier distribution (of both holes and electrons) in the whole device. These hot carriers are simply the delocalized states. Therefore, the current was able to flow through these delocalized states in the whole device for every value of the applied bias voltage. Hence, the resistance in the device was constant for the whole bias voltage range and also significantly lower than the lowest reported resistance in the dark current measurement.

In the case of the second wiring configuration (the gold electrode grounded, bias voltage applied to the aluminum electrode) the behavior was drastically changed compared to the dark current curve of the grounded aluminum electrode. From the lower part of the figure 4.3 one can clearly see the resistance of the measured dark current was constant for all the values of the applied bias voltage. This behavior is

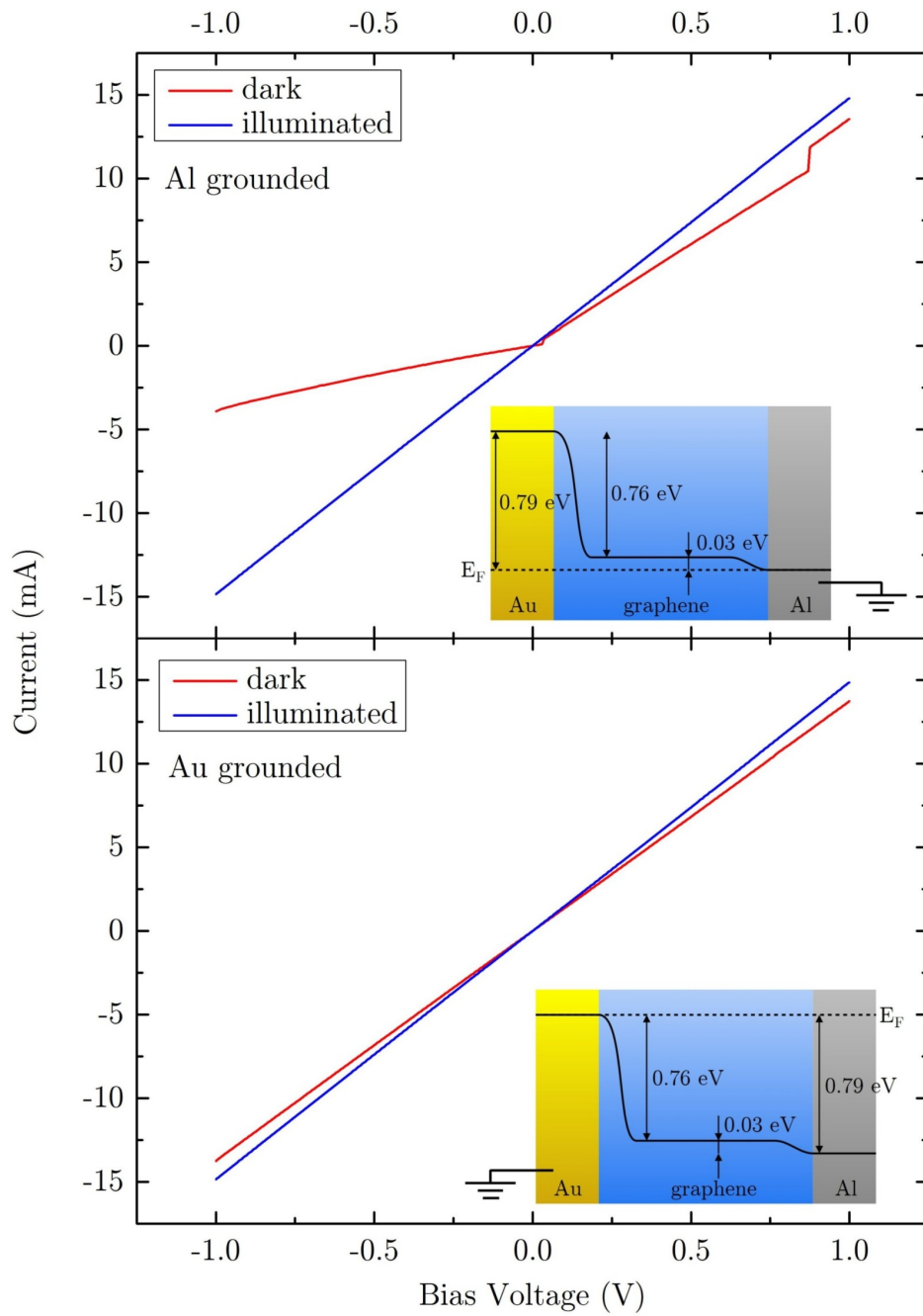


Fig. 4.3: I-V characterization of the bare graphene photodetector for different wiring configurations of electrodes. In the upper part of the figure the results measured in the grounded aluminum electrode configuration (see the inset) are depicted. In the lower part of the figure the measurement results for the grounded gold electrode configuration (see the inset) are shown.

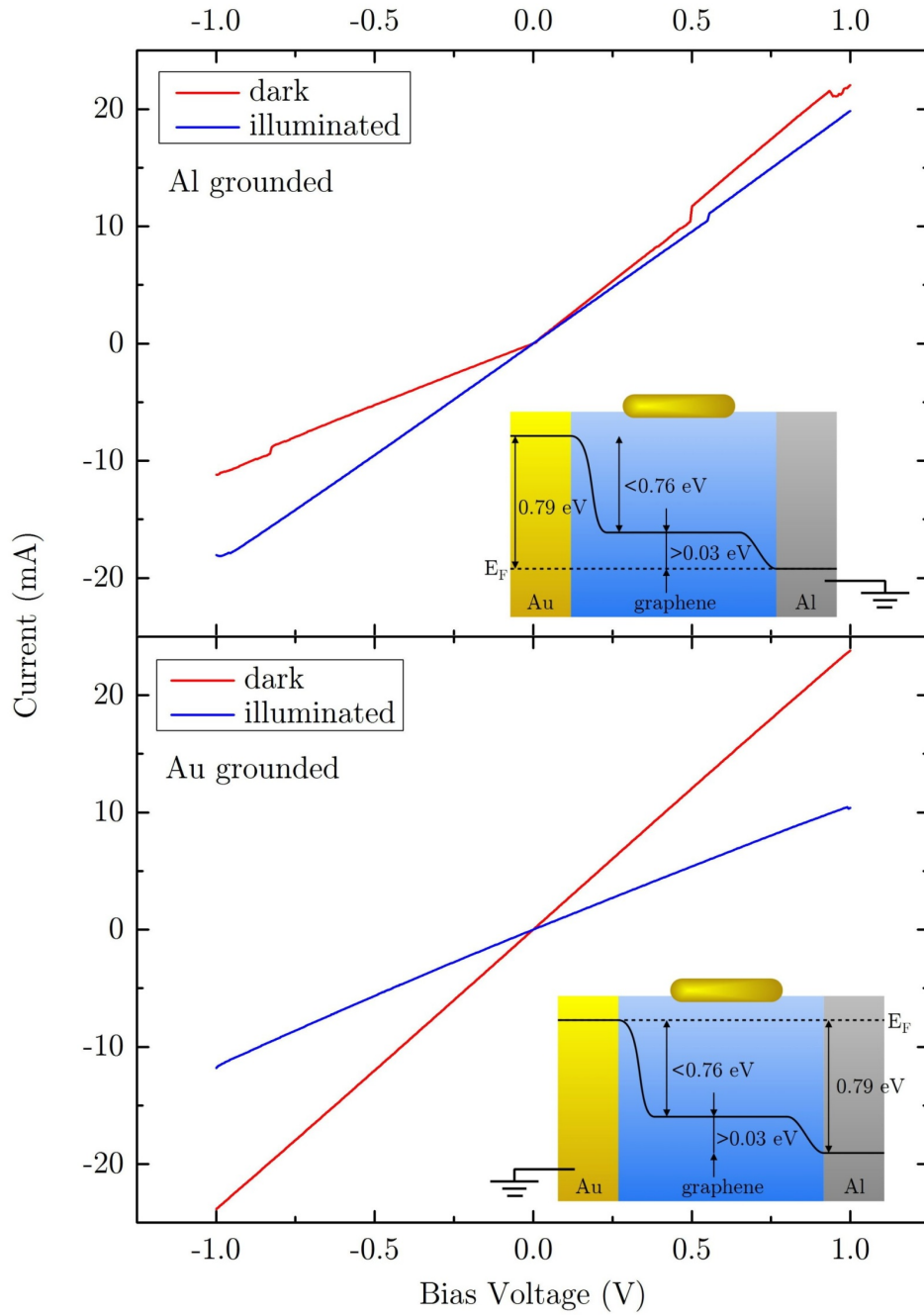


Fig. 4.4: I-V characterization of the prepared graphene photodetector with the gold nanorods placed on its top for different wiring configurations of electrodes. Again, the upper part of the figure corresponds to the results measured in the grounded aluminum electrode configuration (see the inset) and the lower part of the figure shows the measurement results for grounded gold electrode configuration (see the inset).

attributed to the current flow through the delocalized states almost for all the bias voltage values. The reason for missing a resistance step change at a bias voltage of  $-0.79$  V is unclear. The measured I-V curve corresponding to the illuminated device for the gold grounded configuration was completely same as in the case of the aluminum grounded configuration. Therefore, the explanation is also the same. That is the presence of the hot carrier distribution in the graphene created by incident light.

In the following part the I-V measurements of the graphene photodetector with gold nanorods are discussed. If one compares the measurements for both samples and for both wiring configurations depicted in figures 4.3 and 4.4, the dark current curves for the graphene photodetector with gold nanorods shows lower resistance than curves corresponding to the bare graphene photodetector. This feature can be attributed to the effective shielding of the silicon dangling bonds present in the buffer layer by the gold nanoparticles. The silicon dangling bonds are important sources of carrier scattering events in bare epitaxial graphene [86] and thus their shielding results in the lowering of the device resistance.

The results of I-V measurements of the graphene photodetector with the gold nanorods for both wiring configuration are shown in figure 4.4. The dark current curve for the grounded aluminum electrode again showed the complex behavior. However, due to the faintly defined system the step changes of the measured dark current could not be exactly assigned. Nevertheless, the device resistance for the negative bias voltage values was higher due to the bigger amount of the localized states which the current must flow through compared to the positive values of the bias voltage, where the bigger amount of the delocalized states occurs.

The illuminated graphene photodetector with gold nanorods in the grounded aluminum configuration showed the positive photoresponse for the negative bias voltages and the negative photoresponse for the positive bias voltages (compared to the slope of the dark current curve). Due to the presence of gold nanorods on the top of the graphene layer and their acting plasmonic effects the significantly higher amount of hot carriers was created. Based on the only occurrence of the localized states before illumination, these enhanced hot carriers (the number of which was lower for the negative bias voltages compared to the positive once) caused the positive photoresponse. For the positive bias voltage values the delocalized states were present in graphene even before illumination. Therefore, in the illuminated device the amount of hot carriers was drastically enhanced, so that the Coulombic interactions and scattering events became noticeably more probable. That resulted in an increase of the resistance in the device compared to the dark current measurements, giving the negative photoresponse of the device.

In the case of the grounded gold electrode configuration the behavior of dark

current was again different compared to the grounded aluminum electrode configuration. The slope of the dark current curve and corresponding resistance were again constant for all the values of the applied bias voltage as also reported for the bare graphene photodetector in this configuration. The reason for this behavior was again the fact that the current flow only through the delocalized states almost for all bias voltages.

The illuminated graphene photodetector with gold nanorods in the grounded gold electrode configuration showed the noticeable negative photoresponse for all the measured values of bias voltage. Even in the case of no illumination the significant amount of the delocalized states was present in the system for all bias voltage values. Therefore, due to the gold nanorods plasmonic effects arising after the device illumination the amount of the delocalized carriers was drastically enhanced. Therefore, the Coulombic interactions and scattering events again became the processes influencing the current flow in the device significantly. Hence, the resistance of the device drastically increased in comparison with the dark measurement.

The I-V measurements reported here showed significant photoresponses, especially when the gold nanorods were present. Also the different results for the different wiring configurations of the fabricated devices were reported. Therefore, the graphene photodetector with gold nanorods on its surface and the gold electrode grounded proved to be the best combination of the device and corresponding wiring configuration for light detection. This device configuration showed a linear behavior of photoresponse with the growing applied bias voltage. In addition, a negligible photocurrent generated at zero bias voltage was found for both devices in every wiring configuration.

In general, for understanding the graphene photodetectors performance reported here the creation and presence of hot carriers in graphene is necessary. However, to fully understand the behavior of the graphene photodetector based on gold nanorods, the wavelength dependent measurements of photoresponse should be performed in a future research. This experiment could prove that the photoresponse enhancement reported for devices with gold nanorods results from their plasmonic properties.

Generally, the enhanced photoresponse of the system consisting of gold nanorods and graphene motivates in further research on photodetection using graphene and metal nanoparticles conjugates. Particularly, the mechanism responsible for the enhancement of graphene photoresponse when the plasmonically active nanostructures are placed on its top should be studied. The following chapter 5 deals with this challenging task using both the simulations and the experimental approach.

## 5 GOLD NANOROD INTERACTION WITH GRAPHENE

When the nanoparticles made of noble metals are illuminated, they exhibit the collective oscillations of conduction electrons in particles, the so-called localized surface plasmon resonances. These LSPRs have finite lifetimes after which they decay either non-radiatively or radiatively. By adding the underlying substrate the symmetry of the system is broken and thus a new plasmon damping channel is established. However, when considering the whole system the substrate-related damping channel can be seen as a way of energy redistribution from a generated particle plasmon into the substrate.

In the case of the graphene substrate two ways of energy redistribution are discussed in literature: the dielectric interaction between the nanoparticle and the underlying graphene, and the injection of hot electrons generated in the particle into the graphene sheet, both are phenomenologically described in section 2.4. However, none of these effects is clearly refuted or confirmed by a direct experiment.

These energy redistribution channels appear in the particle spectra as an additional broadening of the plasmonic peak. Therefore, single particle spectroscopy can serve as a useful tool to monitor these processes. Moreover, by proper designing a single particle scattering spectroscopy-experiment it can be even possible to distinguish between these two mentioned effects. Anyway, due to the lack of relevant publications dealing with the nature of interaction between plasmonic structures and underlying graphene, the complex approach including calculations and experiments both attempting to find new perspectives and insights into the problem was performed.

In the following sections and paragraphs a proper discussion dealing with the gold nanorod interaction with graphene is given. First, the FDTD calculations of the system consisted of a gold nanorod and variety of substrates are performed (Section 5.1), followed by a short introduction into single particle scattering spectroscopy method and description of the used experimental setup (Section 5.2). Later on, single particle scattering spectroscopy performed both for epitaxial (Section 5.3) and exfoliated graphene (Section 5.4) is presented and discussed.

### 5.1 Finite-difference time-domain simulations

In order to estimate shifts of localized surface plasmon peaks and their broadening changes resulting from placing a gold nanorod on graphene or other corresponding

substrates, the calculation using finite-difference time-domain method were done. As already mentioned in paragraph 2.3.2, the FDTD method is a grid-based numerical method solving the discretized Maxwell's equations in space and time domains [66, 67].

The FDTD calculations were performed using the commercial software *Lumerical* [66]. Either the refractive index or the dielectric function serve as input parameters describing the material optical properties. In this thesis the following materials act in both experiments and calculations: gold, borosilicate glass (BK7), silicon carbide (6H-SiC), graphene and its three-dimensional form - graphite (HOPG). The refractive index data used for gold were measured by Johnson and Christy [54] (Fig. 2.1 or Fig. C.1 in Appendix C), for the BK7 glass the input data were obtained from the company *Schott* [105] (Fig. C.2 in Appendix C). As the input refractive index data of SiC those obtained from measurements done by Singh *et al.* [106] were used (Fig. 5.6). The refractive index data used for graphene and graphite were taken from Weber *et al.* [22] (Fig. 1.5) and Djurišić *et al.* [107] (Fig. C.5 in Appendix C), respectively. All of these materials then act in simulations as an effective media. The configuration and thorough description of computational systems are given in Appendix D.

However, the issue is how to model the graphene layer in FDTD calculations, because this method is not exactly appropriate for ultrathin layers. Graphene is only the one-atom-thick layer having a thickness of  $\approx 3.4 \text{ \AA}$  and anisotropic optical properties in in-plane and out-of-plane directions being approximated by an isotropic complex refractive index *et al.* [22] (Fig. 1.5). Moreover, the graphene layers in FDTD simulations need to be assumed as 1 nm thick to achieve efficient computing [108–110]. This is indeed significant difference compared to the real graphene thickness. Hence, all these approximations of the real graphene layer need to be kept in mind during the data evaluation.

In order to get insight into the gold nanorod behavior when placed on graphene and other substrates the calculations were performed for an increasing gold nanorod volume at a fixed aspect ratio of 2.75. The attention was paid only to the behavior of the longitudinal LSPR peak of these gold nanorods. The calculated dependences of gold nanorod LSPR peak positions and linewidths on the particle volume are shown in figure 5.1. Note that in the notation used here the volume of the nanorod is characterized by its diameter.

The calculated results (Fig. 5.1a) show the effect of retardation on the longitudinal LSPR wavelength. The retardation causes a red shift of the LSPR peak, especially for larger volumes, where the nanorod length is not small anymore compared to the wavelength of incident light. This means that the phase of the electric field is not constant over the length of the nanorod, resulting in a decrease in the

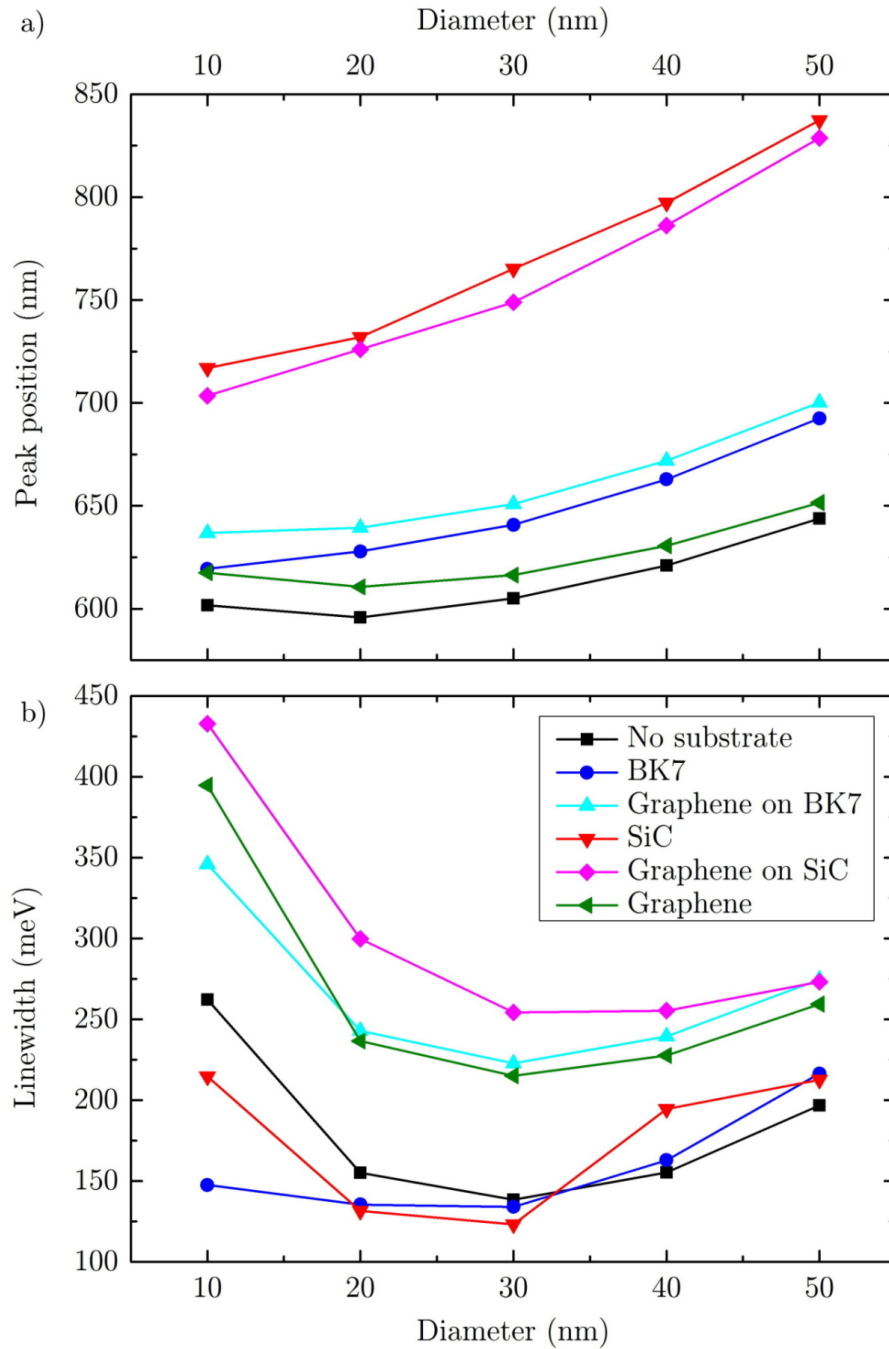


Fig. 5.1: FDTD calculations for scattering of a gold nanorod with the given aspect ratio 2.75 as a function of the particle volume for various underlying substrates. The volume of the particle is in this plot referred to the diameter of nanorod. a) Position of a gold nanorod longitudinal plasmonic peak and the corresponding linewidth of the peak b) as a functions of the particle diameter.

restoring force and thus in a redshift of the resonance wavelength [51]. This is a volume effect, thus upon its increasing, the redshift due to retardation increases. This behavior is reported for all estimated systems suggesting that none of the probed substrates does have an unusual effect on the gold nanorod LSPR peak position. The obtained offsets of the plasmon positions corresponding to the different substrates from the bare nanorod LSPR peak positions are given by the values of the real part of the refractive index of specific substrate materials.

Now, let us focus on the nanorod LSPR linewidth dependence on the particle volume shown in figure 5.1b. The obtained results for all the examined systems show clear contributions of the particle plasmon damping channels earlier discussed in detail in section 2.2. The radiative damping channel broadens the plasmon resonance for large particle volumes (more than about 50 nm in diameter), whereas the surface-induced broadening becomes noticeable for small sizes ( $< 10$  nm in diameter). Thus the minimum in plasmon broadening occurs at an effective diameter of about 30 nm [53,58]. However, the results obtained for systems containing graphene shows a considerably higher linewidth magnitudes for all the reported particle volumes. This suggests the presence of strong coupling between the gold nanorod and underlying graphene.

The electric near-field distribution in close vicinity of the nanoparticle can give a useful information about the optical properties of examined systems. Here, the electric near-field distributions were recorded in order to visualize the penetration of electric near-field into the underlying graphene and other substrates of interest. The examined system consisted of the gold nanorod with the aspect ratio 2.5 and diameter 20 nm, earlier described in section 3.3 where named NR-20-700. The electric field in close vicinity of the nanorod was calculated for nanorod longitudinal resonant frequency illumination and the obtained results are plotted in term of normalized electric field to the incident illumination giving the enhancement of the electric field. The results of performed calculations for the gold nanorod on different underlying substrates are shown in figure 5.2.

The obtained results clearly show the enhancement of the electric field in the vicinity of the gold nanorod for the longitudinal LSPR. The enhancement of the electric field is highest at the nanorod tips and decays exponentially into the surroundings. Thus, when the underlying substrate is present the enhanced electric field penetrates into the substrate. Moreover, the presence of a substrate results in the creation of *hot spots* with extremely large electric field enhancements, mainly determining the plasmon interaction with the substrate [61].

Importantly, the simulated systems containing graphene show a higher electric field above and under the graphene than that inside the layer. This behavior suggests the enhanced absorption in the graphene layer further supported by the gold

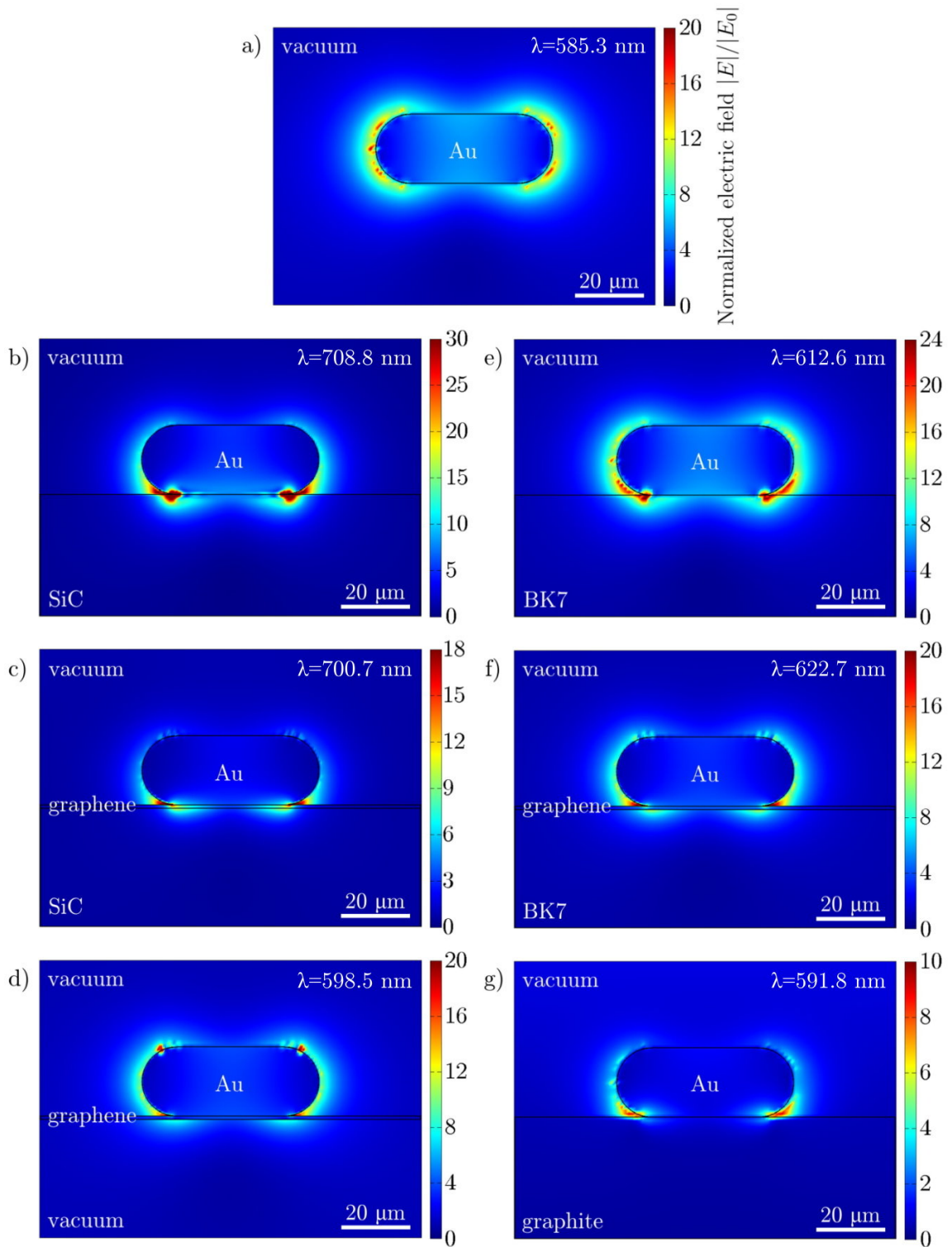


Fig. 5.2: FDTD calculations of electric near-field enhancement for a gold nanorod placed on variety of substrates: a) gold nanorod in vacuum without any substrate, b) on silicon carbide, c) on graphene laid on silicon carbide, d) on bare graphene layer in vacuum, e) on BK7 glass, f) on graphene on BK7 glass, and g) on graphite (HOPG).

nanorod behavior on graphite, where the significant electric field damping compared to the other substrates is reported. However, this graphene behavior is not found for graphene on silicon carbide. That can be explained by the refractive index data used for SiC suffering from the missing imaginary part (Fig. 5.6). The optical properties of silicon carbide are in detail discussed later in paragraph 5.3.1. However, there is a question for the future research, how much and in what way is the light absorption in graphene affected by its substrate.

The performed FDTD calculations serve only as a tool to give supporting informations, but not the reliable results due to the fact, that too many approximations and assumptions are involved. Therefore, the calculated spectra are not correlated and compared with the results obtained from the following experiments. Anyway, the obtained results give us an idea how the gold nanorods behave on the examined substrates. This knowledge thus can be used in single-particle scattering experiments discussed and performed in the following section.

## 5.2 White-light single particle scattering spectroscopy

Far-field optical techniques are used to study the spectral properties of gold nanorods under white-light illumination. The spectras of single nanorods are recorded to estimate the longitudinal LSPR peak shifts and broadenings due to the presence of the underlying graphene substrate. These measurements are performed to determine the particle plasmon damping when the particle is placed on graphene and thus to distinguish between the electromagnetic field coupling damping channel and the hot carrier injection damping channel, both discussed earlier in section 2.4. The nanorods are measured one by one due to their distribution in size and thus the statistics considering the Gaussian size distribution can be applied, resulting in reliable and precise results for a given nanorods ensemble.

The scattering microscopy techniques deal with the filtering of incident light and thus recording only the signal corresponding to the scattering. There is a variety of optical setups and configurations useful for a single-particle detection [58], the choice of which is dependent on the used sample. In this work the single-particle white-light scattering microscopy experiments were performed with the *Nikon Ti/e* microscope adapted for white-light scattering and with an *Acton SPi* spectrometer from the *Princeton Instruments* company. The output port of the microscope can be switched to either an electron multiplying charge coupled device (EMCCD) camera (Andor iXon<sup>EM</sup> + 885), which is used to find the location of a specific nanorod, the spectra of which is to be measured, or to the spectrometer to measure the white-

light spectrum of the selected nanorod. Moreover, the microscope is equipped with a movable stage enabling the movement of a sample within the micrometer scale precision using the computer interface. The used microscope setup enables us to illuminate a sample from different directions, making the setup a useful tool for single particle scattering spectroscopy. The specific illumination configuration used for experiments performed in this thesis depended on the sample of interest discussed in detail in paragraph 5.2.1.

Regardless of the used illumination configuration the output of the EMCCD camera gives the image consisted of a few bright diffraction spots on dark background. The measured samples were prepared in order to have only single-particles on a substrate surface without any conjugates of particles. However, there still is a certain probability of creation of such clusters. Therefore, arises the problem that has to be encountered, the diffraction-limited spots can not belong to a single particle, but to a cluster of two or more gold nanorods. They do not give a reliable information about plasmon and, therefore, these spectras from clustered particles need to be filtered out. The easiest way how to do it is a close look at the measured spectras. The clusters can be recognized when the spectrum is asymmetrical, extremely broad or more peaks are visible. Two typical examples of such cluster spectra are shown in figure 5.3.

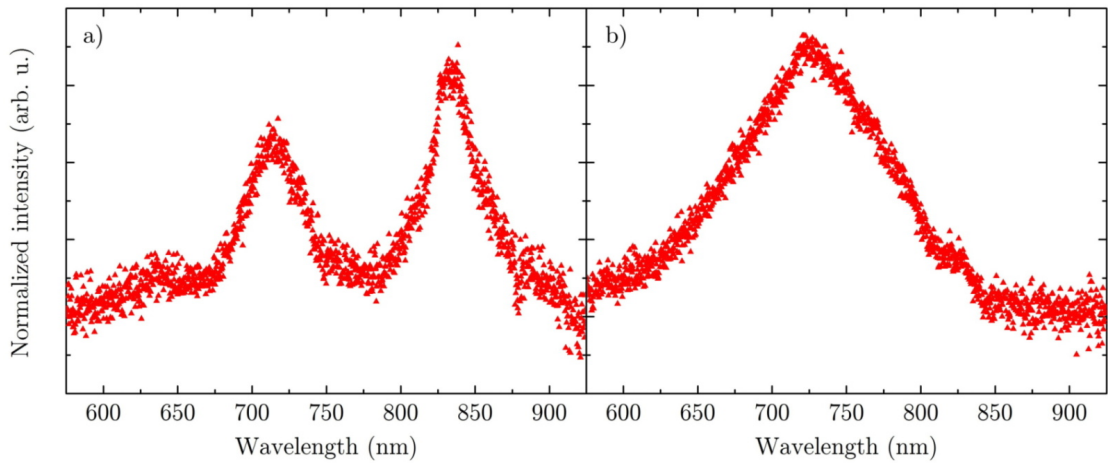


Fig. 5.3: Two examples of spectra of clustered particles. a) The spectrum of two particles with two corresponding longitudinal LSPRs. b) The spectrum of two or even more clustered nanoparticles with too broad linewidth.

### 5.2.1 Apparatus configuration

Single particle white-light scattering microscopy can be realized by several measurement setups which differ mainly in illumination approach [58]. The type of the used illumination scheme depends on the properties of the sample of our interest. Here, in this thesis, two different groups of samples were studied and thus two different illumination approaches provided. The first group of the samples was represented by gold nanorods placed on epitaxial graphene grown on silicon carbide and other corresponding substrates (Section 5.3). The scattering spectroscopy of these nanoparticles was realized in the dark-field configuration (Fig. 5.4a). The second group of the samples corresponded to gold nanorods on exfoliated graphene flakes placed on borosilicate glass (BK7) and related samples (Section 5.4). These samples were measured in the total internal reflection (TIR) configuration (Fig. 5.4b).

In the dark-field configuration the sample was illuminated under a high incident angle. The incoming light is then reflected by a substrate according to Snell's law. That results in situation when only the light scattered by a gold nanorod is collected by an objective lens with low numerical aperture ( $NA$ ) and thus the resulting microscope image is provided in the dark-field mode. Both the illumination and detection angles have to be chosen carefully to make sure that no direct light enters the objective. This can be controlled by adjusting the angle of incident light and by a proper selection of the used objective, namely its  $NA$ . For the experiments done within the dark-field illumination (Section 5.3), the *Plan Apo VC 20x DIC N2* objective with  $NA = 0.75$  was used. It is worth noting that the used microscope allows one to increase the magnification of the objective twice resulting in the final magnification of 40 times.

Though the microscopy using the dark-field illumination scheme gives dark-field images of the gold nanorods, there is still some undesirable background signal. Moreover, the scattering microscopy experiments performed with the group of samples representing by gold nanorods on exfoliated graphene flakes (Section 5.4) are also carried out within small nanorods NR-10-700 and NR-20-700. The scattering cross section is proportional to the volume squared (Eqn. 2.19), and thus the scattering signal intensity can vanish in background. Therefore, the different illumination scheme giving a high ratio between the scattering signal and the background noise needs to be applied for the experiments described in section 5.4. The illumination configuration fulfilling this requirement is the total internal reflection scheme.

The plasmons of the gold nanorods are excited in a total internal reflection microscopy (TIRM) setup by an evanescent field created by total internal reflection of light. The scheme of the illumination configuration using TIR is shown on figure 5.4b. The white light source illuminates the glass prism placed at the top of

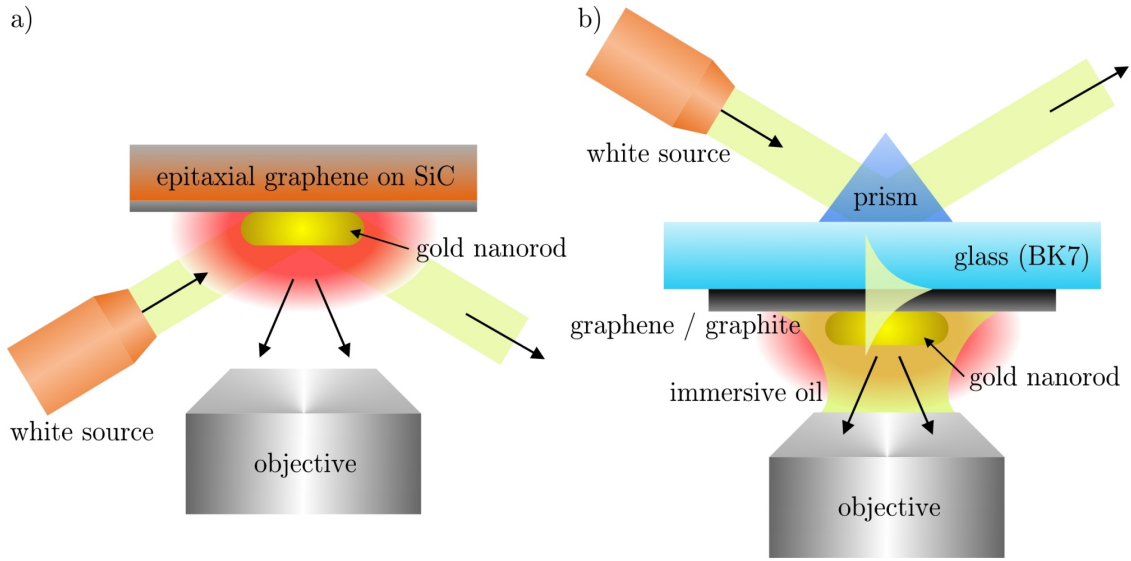


Fig. 5.4: Schematic of a single particle white-light scattering microscopy setups used in this work. a) The dark-field configuration was applied in experiments with a group of samples representing by gold nanorod placed on epitaxial graphene on SiC (Section 5.3). b) The total internal reflection configuration. These approach was utilized for samples consisting of gold nanorods placed on exfoliated graphene flakes on borosilicate glass (Section 5.4). Images are not to scale.

the glass substrate and is refracted into the prism. Here, at the interface between the prism and the glass substrate the total internal reflection occurs, creating a non-propagating evanescent field. This field tunnels through the glass towards the second interface where decays exponentially from the interface and thus penetrates into the surroundings to a depth of approximately 100 nm.

The largest gold nanorods used in this thesis are the NR-40-650 with a diameter of 40 nm, therefore, the whole nanoparticle is successfully surrounded by the evanescent field providing efficient excitation of particle plasmons. The excited particles then scatter the light which is collected by an objective. The high ratio between the signal and the noise is reached in TIRM due to the exponential decay of the excitation evanescent field which is thus not collected by the objective.

The single particle white-light scattering experiments realized in the TIR configuration were performed within the oil-immersion objective *Plan Fluor 100x Oil Iris DIC H N2* with the adjustable numerical aperture. The refractive index of the immersion oil was  $n = 1.515$  and the  $NA$  of the objective was set to 1.3. Unlike the dark-field configuration experiments, the microscope was not set to give twice higher magnification and, therefore, the magnification was determined only by the objective giving a value of 100 times.

### 5.3 Gold nanorod interaction with epitaxial graphene

After the description of single particle scattering spectroscopy and related experimental setup the experiments on single particles will be discussed in detail. The suggested experiments consist of two steps. First, the single particle scattering spectroscopy will be performed with gold nanorods placed on pure epitaxial graphene on silicon carbide and other substrates (SiC, BK7 glass and HOPG). Then in the second step, the spectroscopic measurements will be performed with nanorods separated from the surface of these substrates by an insulating layer with varying thickness. This spacing layer should ensure the stopping of potential injection of hot carriers generated by a nanorod into graphene, providing thus the quenching of a potential channel for nanorod conductive coupling damping. The measured dependence of the plasmon linewidths on the insulating spacer thickness should allow us to distinguish between the electric field coupling interaction and the hot carrier injection from a gold nanoparticle and to underlying graphene.

The samples were prepared according to the procedures described in chapter 3, the gold nanorods (NR-40-650) were deposited onto glass slides using spin-coating, then the nanorods were transferred using PMMA wet transfer on four different substrates: BK7 glass, silicon carbide, epitaxial graphene on silicon carbide and HOPG. It is worth noting, that in the case of the BK7 glass substrate the nanorods were only deposited onto glass and the transfer onto another glass coverslip was skipped. Moreover, the prepared samples did not undergo the post UV/ozone treatment and the salt solution bath, so that the CTAB bilayer surrounding the gold nanorods could not be fully disrupted and thus influence the measured results.

The scattering spectras were sucessfully recorded for the nanorods placed on the BK7 glass, silicon carbide and epitaxial graphene on SiC. However, the spectras corresponding to gold nanorods on HOPG could not be measured due to both the high reflections from the substrate and the huge broadening of gold nanorod plasmon peak caused by the HOPG substrate. Single-particle scattering spectras of 20 nanorods deposited on each selected substrate were acquired within the dark-field configuration and the averaged peak positions and linewidths of their peaks statistically processed (Fig. 5.5). The error bars for all binned data correspond to standard deviation in the linewidth and resonance wavelength.

The silicon carbide substrate red-shifts the gold nanorod longitudinal plasmon peak significantly in comparison with the BK7 glass. For the BK7 glass substrate the peak position was  $\lambda_0^{\text{BK7}} = 610.3 \pm 6.2$  nm and for silicon carbide  $\lambda_0^{\text{SiC}} = 713.2 \pm 9.5$  nm. The red-shift of the peak position compared to glass

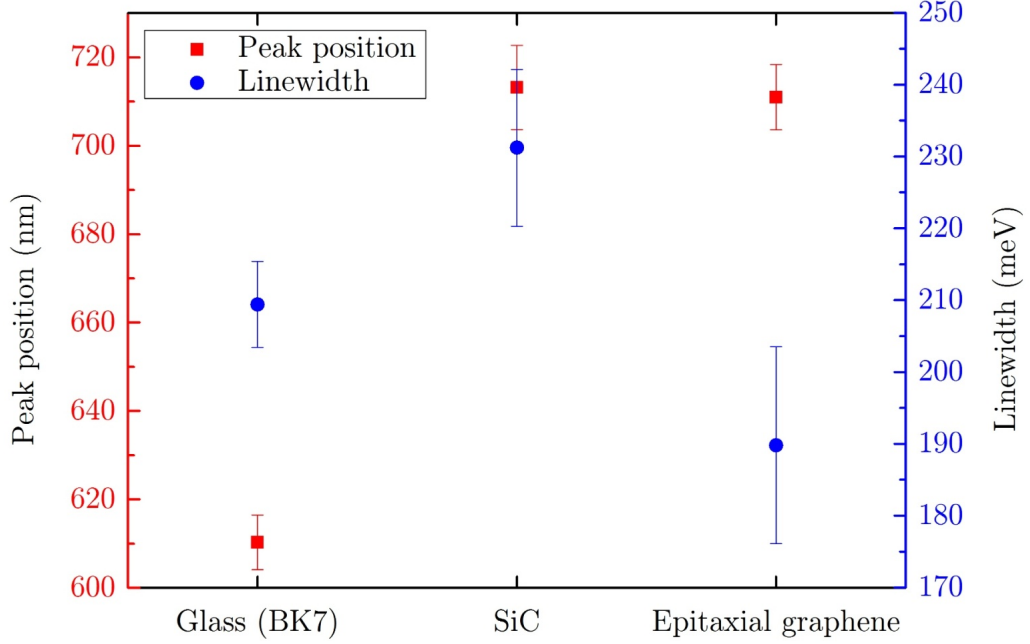


Fig. 5.5: Peak positions (red squares) and corresponding linewidths (blue circles) of a gold nanorod longitudinal plasmonic peak on the BK7 glass ( $\lambda_0^{\text{BK7}} = 610.3 \pm 6.2$  nm,  $\Gamma_{\text{BK7}} = 209.4 \pm 6.0$  meV), silicon carbide ( $\lambda_0^{\text{SiC}} = 713.2 \pm 9.5$  nm,  $\Gamma_{\text{SiC}} = 231.2 \pm 10.9$  meV) and epitaxial graphene on SiC ( $\lambda_0^{\text{EG}} = 711.0 \pm 7.4$  nm,  $\Gamma_{\text{EG}} = 189.8 \pm 13.7$  meV). The error bars correspond to standard deviations.

also occurs for epitaxial graphene on SiC, but less than for silicon carbide only, giving a value of  $\lambda_0^{\text{EG}} = 711.0 \pm 7.4$  nm. This behavior can be attributed to the higher values of the real part of SiC refractive index comparing to that of the BK7 glass. By adding the epitaxial graphene interlayer the nanorod gets further from silicon carbide causing a less efficient coupling with it resulting in a slight blue-shift of plasmon peak in comparison with the bare SiC.

Surprisingly, the similar behavior occurs also for the particle plasmon linewidth. Here, the plasmon damping is big for bare silicon carbide giving a value of the peak linewidth  $\Gamma_{\text{SiC}} = 231.2 \pm 10.9$  meV and a significantly lower value of  $\Gamma_{\text{EG}} = 189.8 \pm 13.7$  meV for the epitaxial graphene on SiC. This behavior is in stark contrast with the measurements reported in literature [69], where an additional broadening of the particle plasmon peak caused by presence of graphene was found. However, the measurements done in the paper by Hoggard *et al.* [69]

were not performed using the epitaxial graphene grown on silicon carbide.

Nevertheless, there are few features present in our experiments which should be taken into account while discussing the obtained results. Unlike the epitaxial graphene substrate, the silicon carbide includes a thin layer (few nanometers) of oxide on the surface possibly influencing its optical properties. On the other hand, epitaxial graphene is separated from a silicon carbide substrate by a  $\sim 3 \text{ \AA}$  thick buffer layer [86], optical properties of which are not properly determined in literature [111] and its influence on the graphene optical properties is also not clear. It is worth to note, that the linewidth corresponding to a gold nanorod placed on the BK7 glass is so large ( $\Gamma_{\text{BK7}} = 209.4 \pm 6.0 \text{ meV}$ ) due to the significant contribution of the gold interband transitions resulting from the plasmon position closer to the gold interband threshold.

Unfortunately, the damping channels of particle plasmon caused by graphene are lost in the damping channels related to the silicon carbide. Therefore, the resultant optical responses of silicon carbide and epitaxial graphene grown on SiC complicated our experiments dealing with monitoring the broadening of plasmonic peaks in dependence on thickness of an insulating spacing layer between the nanorod and the substrates. The behavior of gold nanorods placed on silicon carbide substrate was absolutely unexpected. Therefore, the next paragraph deals with the optical properties of silicon carbide to get some insight into the effects causing this unusual particle plasmon broadening.

### 5.3.1 Optical properties of silicon carbide

Silicon carbide has been a well known material since the half of the 20th century and thus intensively researched. During that time more than 200 crystallographic allotropes of SiC have been found, however, most attention was paid to these polytypes: 3C-SiC, 4H-SiC and 6H-SiC [112]. These types differ in both the crystallographic configuration and the correspondings electronic and optical properties. In this thesis, the 6H-SiC (also sometimes called  $\alpha$ -SiC) crystallographic type was used for all performed experiments including the epitaxial graphene growth.

Both for the experiments and the calculations performed in this thesis, the knowledge of wavelength dependent optical constants of 6H-SiC in the visible and near-infrared is crucial. For FDTD calculations these optical constants act as input parameters, and in the case of experiments the constants are necessary for understanding the obtained results. However, the literature dealing with measuring either the complex refractive index or the complex dielectric function of SiC is focused more on the far-infrared [113,114] and the ultraviolet [115] spectral range and in the spectral area of our interest only few data points have been measured [116].

The only work focusing on the visible part of spectrum was done by Singh *et al.* [106]. Therefore, these data are depicted in figure 5.6 and were used in FDTD calculations performed in this thesis. However, by a closer look at the 6H-SiC refractive index data (Fig. 5.6) it is clear that there is no imaginary part of this function. This fact makes the data not so reliable because the imaginary part of the complex refractive index corresponding to the light absorption should be present for every crystalline material even for energies lower than bandgap. For 6H-SiC the band gap is  $E_g = 3.21$  eV [117] giving the threshold wavelength of  $\lambda_g = 388.8$  nm.

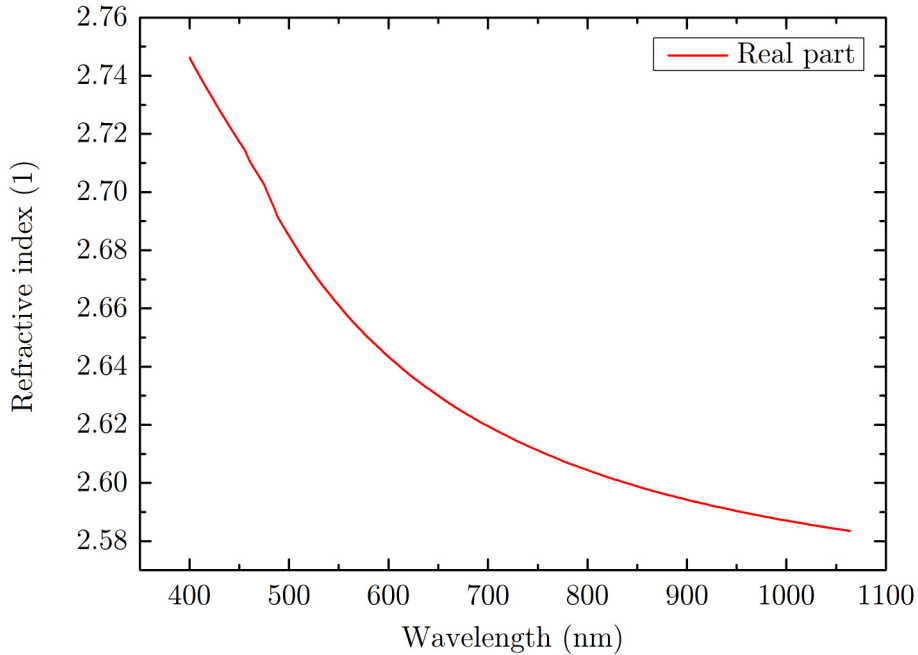


Fig. 5.6: Refractive index of silicon carbide (6H-SiC), data measured by Singh *et al.* [106].

During the work on this thesis, the relevant data for the imaginary part of the silicon carbide complex refractive index in the visible and near-infrared parts of spectrum has not been found in the literature. The complex refractive index of SiC could be measured for instance by spectroscopic ellipsometry, which might help to understand the unexpected optical response reported in section 5.3. However, this task goes beyond the scope of this thesis.

## 5.4 Layer-dependent study

To overcome the problems with silicon carbide and related epitaxial graphene in the single particle scattering experiments, a different type of graphene needs to be used. Therefore, graphene samples were prepared by mechanical exfoliation from graphite and placed on a BK7 glass substrate. However, the result of this method is not integral layer over the entire substrate surface. Instead, a lot of small (tens of micrometers) graphene pieces, called flakes, were present on the surface. The graphene exfoliation method suffers from the fact, that the only small fraction of flakes is the one-atom thick. Therefore, the flakes showing up a broad thickness distribution are found on the glass substrate. Nevertheless, this imperfection of the exfoliation method gives us an opportunity to perform scattering measurements in dependence on the thickness of underlying graphene.

Therefore, a novel design of experiment is suggested. By monitoring the behavior of the gold nanorod longitudinal plasmon peak as a function of the number of underlying graphene layers we should be able to determine the nature of energy redistribution in the gold nanorod placed on graphene/graphite flakes. Moreover, by performing the experiments with more types of nanorods, differing in their dimensions, we should be even able to evaluate the energy redistribution process.

In layer-dependent single particle scattering spectroscopy the TIR configuration (Fig. 5.4b) was used. Therefore, the measurements proceeded in the immersion oil environment described above. The experiments were performed for all types of nanorods defined in section 3.3, which differed in both the aspect ratio and diameter. In this section they are referred to their diameter. The samples were prepared according to the methods described in chapter 3. The graphene layers were peeled off from the HOPG using a *Scotch* tape and transferred onto the BK7 glass. The tape residues were dissolved by inserting the sample into a toluene bath for 5 hours. Gold nanorods were deposited on the glass coverslips by spincoating and subsequently transferred using the PMMA wet transfer onto the glass slide with already deposited graphene flakes. Then, the PMMA was dissolved in the chloroform bath overnight. Moreover two additional steps were added into the sample preparation process to thoroughly get rid of the CTAB molecules from nanorod surface: Prior to the gold nanorods transfer the UV/ozone treatment for 1 hour and during the transfer the salt solution bath were applied.

Such a sample preparation results in gold nanorods randomly distributed over the substrate surface and thus also a significant part of nanorods took place on the flakes. In general, this procedure does not give a precisely determined system wherein the nanorod of known dimensions is placed on the flake with a given number of graphene layers. Most likely the situation corresponds to gold nanorods showing

a Gaussian distribution in their dimensions placed on variety of randomly thick graphene flakes. However by measuring a big quantity of particles the statistic can be applied on both the gold nanorods and the underlying graphene / graphite flakes.

The scattering spectras of individual gold nanorods were measured separately one by one and, independently, the number of underlying graphene layers right in the place of the nanorod was determined. These recorded data points were then divided into data sets according to the number of graphene layers. The histogram showing the amount of nanorod scattering spectras corresponding to the given number of underlying graphene layers for all the used gold nanorod types is depicted in figure 5.7.

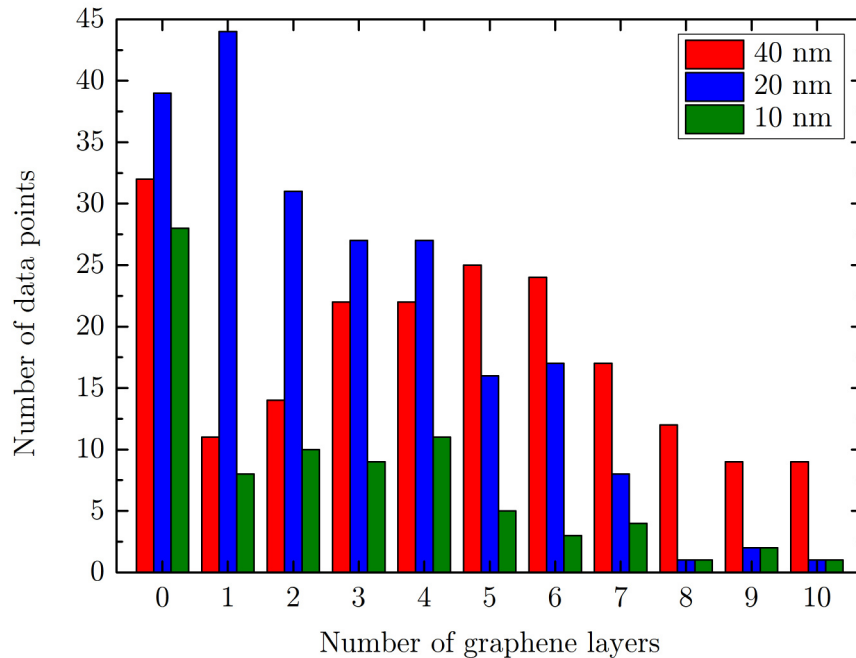


Fig. 5.7: Histogram showing the amount of the measured nanorod scattering spectras corresponding to the given number of underlying graphene layers. Three different types of gold nanorods were used in the single particle scattering experiments differing both in the aspect ratio and the diameter. Here, they are referred to their diameter and their exact dimensions and properties can be found in table 3.1.

First, let us discuss the results obtained for gold nanorods with a diameter of 10 nm. Recording of single particle scattering spectra was extremelly difficult due to low signal noise ratio for nanorods of 10 nm in diameter. Although nearly a thousand

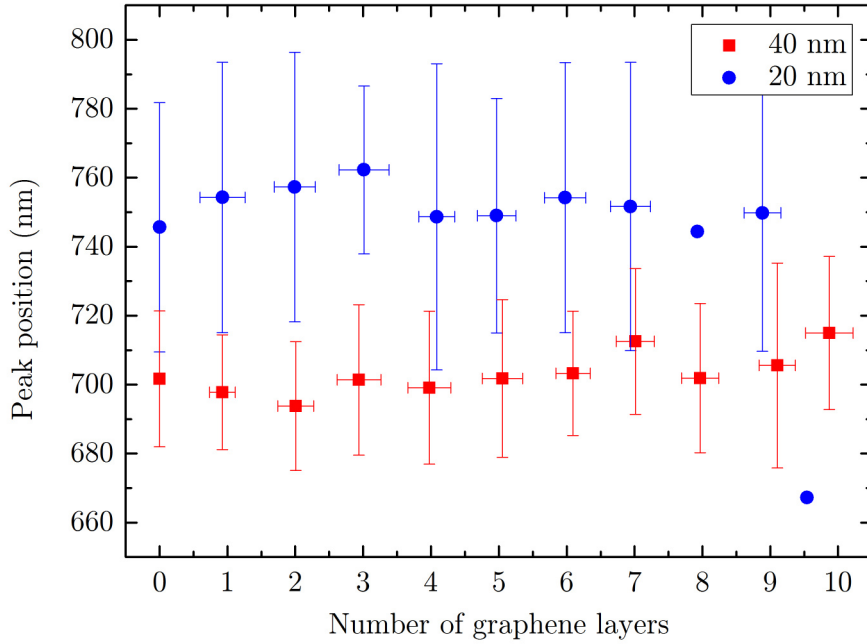


Fig. 5.8: The position of the gold nanorod longitudinal plasmonic scattering peak as a function of the number of underlying graphene layers. The error bars correspond to standard deviations of data set distributions. The histogram of the data taken into account for the shown data sets is depicted in figure 5.7.

of diffraction spots spectras was measured, only a few results were obtained (Fig. 5.7 - green color). It was even hard to find a gold nanorod on the bare glass without an underlying graphene flake. We believe that the measured data correspond only to the edge of nanorod size distribution, ergo only to the bigger particles from the ensemble. Therefore, this data set is not fully trustworthy and is not further considered.

On the other hand, the data obtained for the gold nanorods with the diameters 40 nm and 20 nm show sufficient data sets to get reliable results. Especially, in the range from zero to six graphene layers there is a sufficient quantity of data enabling to encompass almost the entire Gaussian distribution. However, in the case of the nanorods of 20 nm in diameter the single particle scattering experiment became insufficient for seven and more underlying graphene layers caused probably by a large plasmon broadening, and thus vanishing of the signal in the background. The same behavior occurred also for the gold nanorods with 40 nm in diameter when placed on flake with thickness higher than ten layers (not shown).

By plotting the gold nanorod plasmon peak positions as a function of underlying

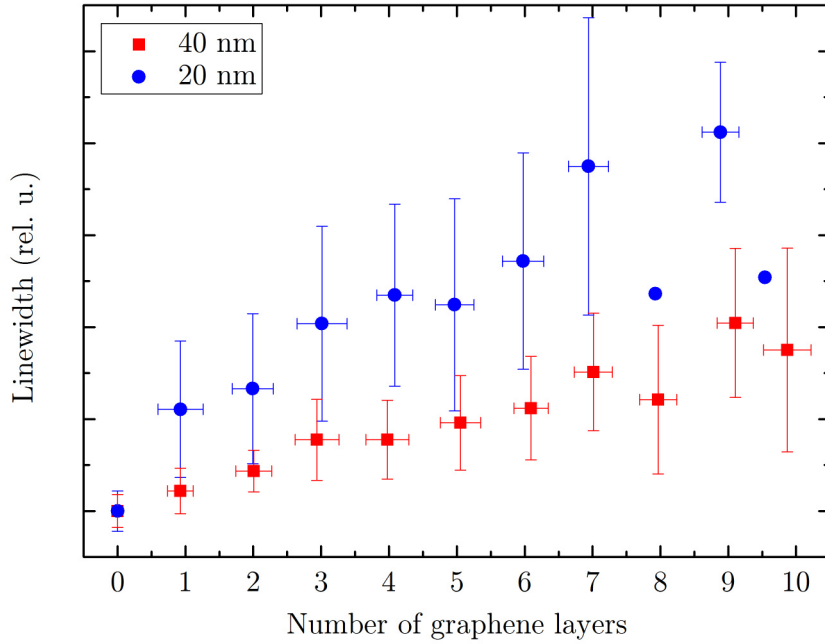


Fig. 5.9: Normalized linewidths of the gold nanorod longitudinal scattering peak as a function of the number of underlying graphene layers. The error bars correspond to standard deviations of data set distributions. The histograms of the taken data sets is depicted in figure 5.7.

graphene layers (Fig. 5.8) almost no dependence was found for both nanorod types. That suggests the underlying graphene / graphite layer is not sufficiently thick to influence the plasmon peak position even if the big mismatch in real parts of refractive indexes for graphene and the BK7 glass underneath of it is present. The real part of graphene (and also of graphite) refractive index is almost twice bigger than that of the BK7 glass in the wavelength range from 600 nm to 1000 nm.

The situation is completely different for the plasmon peak linewidth. Figure 5.9 shows the normalized plasmon linewidth as a function of the number of underlying graphene layers, wherein the strong dependence is observed. Even for one graphene layer the plasmon linewidth is significantly increased, showing the presence of a substantial damping factor, which is not present for nanorods placed only on bare glass. The linewidth then further increases by adding additional graphene layers. From figure 5.9 it is clearly seen that the damping is stronger for the smaller nanorods with a diameter of 20 nm compared to the bigger ones. In general, the small plasmonic particles are more effected by the presence of the substrate than the bigger ones [58,61] suggesting that the observed dependence can be caused by electromagnetic field

coupling of gold nanorod field with the underlaying graphene / graphite.

The gold nanorod plasmon linewidth for one graphene layer was changed compared to a zero graphene layer in the case of nanorods with the 20 nm diameter from  $\Gamma_{0L}^{20 \text{ nm}} = 111.1 \pm 12.2 \text{ meV}$  to  $\Gamma_{1L}^{20 \text{ nm}} = 172.6 \pm 41.2 \text{ meV}$  and for the nanorods with the diameter of 40 nm from  $\Gamma_{0L}^{40 \text{ nm}} = 200.0 \pm 18.1 \text{ meV}$  to  $\Gamma_{1L}^{40 \text{ nm}} = 223.0 \pm 24.8 \text{ meV}$ . Considering the atomic thickness of one graphene layer the reported extraordinary linewidth changes can not be caused only by the electromagnetic coupling. That suggests the presence of an additional damping channel. According to literature (discussed in section 2.4) we believe this plasmon extraordinary broadening is caused by injection of hot electrons from gold nanorods into graphene. The hot electrons generated by gold nanorod tunnel into the first graphene layer preferentially and the tunneling of charge carriers between graphene layers is highly unlikely [118]. It means that the possible hot carrier injection damping channel is significant especially for a low number of graphene layers (up to 3) while the plasmon damping caused by electric field penetration into underlaying graphene / graphite becomes more significant for the system consisted of more graphene layers (more than four). In this situation the thickness of the underlaying graphene / graphite substrate becomes high enough to act as an effective dielectric medium.

However, the useful information about the obtained results can be given also by the Q-factor dependence on the number of graphene layers. The Q-factor is the ratio between the position in eV and the peak linewidth in eV ( $Q = E_0 \text{ (eV)} / \Gamma \text{ (eV)}$ ). The obtained dependence is depicted in figure 5.10 in the normalized form. Due to its definition the behavior inverse to that of the linewidth is obtained. For the first graphene layer an unexpected drop compared to zero layers is found for both data sets followed by a Q-factor gradual decrease with the increasing number of graphene layers. This behavior of the Q-factor is quite expected due to the reported constant peak positions for both gold nanorod types.

By increasing the nanorod longitudinal peak linewidth with the increasing number of underlaying graphene layers, the peak intensity decreases for both measured gold nanorod types. However, in the case of bigger nanorods with the diameter of 40 nm, an interesting feature appears. By decreasing the longitudinal peak intensity another peak positioned at  $\sim 560 \text{ nm}$  appears in the measured spectras of the gold nanorods placed on graphene / graphite within the thickness higher than one graphene layer (not shown in this thesis). This peak shows no dependence on the increasing number of graphene layers giving the constant peak position  $\lambda_0 = 568 \pm 24 \text{ nm}$  and linewidth  $\Gamma = 542 \pm 120 \text{ meV}$ . Note that the big values of standard deviations are caused mainly by the used fit. The nature of this novel peak is not fully clear and thus needs to be further studied. However, we attribute this peak to the transversal mode of the

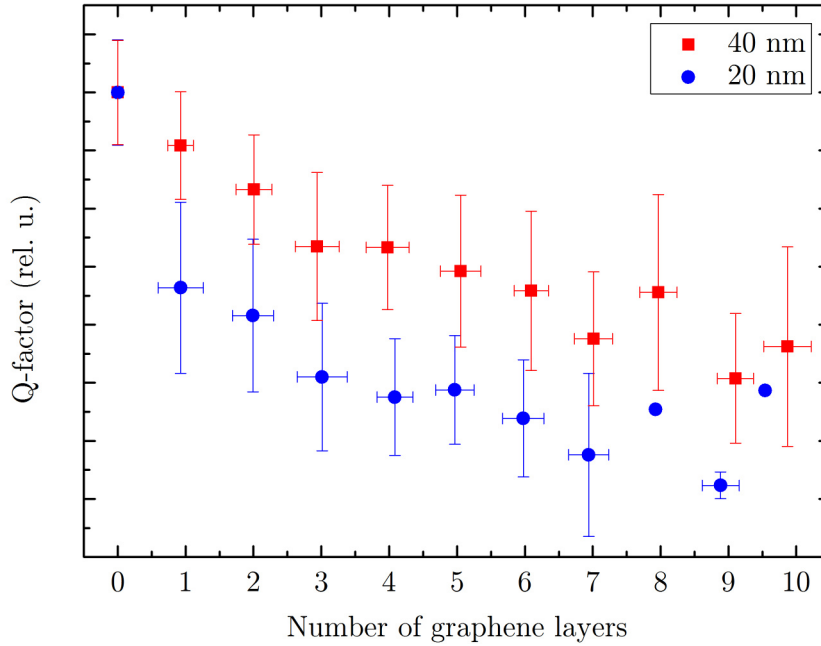


Fig. 5.10: Normalized Q-factor of the gold nanorod longitudinal scattering peak as a function of the number of underlying graphene layers. The error bars correspond to standard deviations of data set distributions. The histogram of the taken data sets is depicted in figure 5.7.

gold nanorod mainly due to its position.

In general, the obtained results show a strong influence of the gold nanorod longitudinal peak on the underlying graphene / graphite layer, significantly even on one graphene layer only. However, the transversal peak of gold nanorods seems not to be influenced. This behavior can be possibly explained by an enhancement of the electric field in the nanorod vicinity. This is huge for the gold nanorod longitudinal LSPR mode giving an enhancement factor of  $\sim 21$ , whereas for the transversal mode the electric field is enhanced by a factor of only  $\sim 4$  (Fig. 2.5). For both discussed plasmon damping channels (electromagnetic coupling and hot electron injection) the electric field acts as an important parameter [75, 76]. Thus, the plasmon damping caused by graphene should be higher for the nanorod longitudinal plasmonic mode.

The performed experiments showed the extraordinary broadening of gold nanorod longitudinal plasmon peaks when the nanorod is placed on the graphene substrate. However, from the performed experiments we can not conclude if the energy redistribution in the gold nanorod on the graphene system is caused either by the electromagnetic coupling or by the hot electron injection channels. Most likely, both

effects contribute to energy redistribution in the given system. But to directly answer this question additional experiments need to be performed in the future.

The suggested experiment should deal with inserting the insulating spacing layer into the system and then again recording the gold nanorod scattering spectras as a function of the number of underlying graphene layers. The spacing layer should prevent the potential injection of hot carriers generated by nanorod into graphene. This should provide the quenching of the potential conductive coupling damping channel in the system. However, the deposition of such a layer onto a graphene substrate would give a surface with an inhomogeneous thickness. Therefore, a different approach will be chosen to overcome this difficulty. The gold nanorods will be directly covered by a 5 nm thick insulating silica capping layer.

## 6 CONCLUSION

In this thesis we have proposed a novel hybrid photodetection device consisting of graphene and gold nanorods. In this device graphene acts as a photoactive layer and the gold nanorods placed on its top then serve as a factor causing enhancement of photoresponse and sensitivity of the proposed photodetector. Such enhancement is provided by creation of localized surface plasmon resonances in the gold nanorods and subsequent transfer of the energy of plasmons into graphene upon illumination of the device by incoming light. The channels of energy redistribution from oscillating plasmon in the nanoparticle to graphene were neatly treated to determine the exact mechanism responsible for the energy transfer. This was done by single particle white-light scattering spectroscopy showing the novel unexpected energy transfer channel present in the graphene / gold nanorod system.

We have reported bias-dependent photoresponse observations in proposed photodetector devices when the bias voltage was applied using the I-V measurement technique. The devices consisted of bare epitaxial graphene on SiC and epitaxial graphene on SiC with the gold nanorods placed on its top, both devices contacted with asymmetric metal electrodes (gold, aluminum) in the metal-graphene-metal configuration. The bias-dependent photoresponse was found even for the bare graphene photodetector. Nevertheless, the significant enhancement of photoresponse was found in the situation, where the device consisted of graphene and gold nanorods on its top.

However, the photoresponse behavior for both devices significantly differed for the different wiring configuration. The corresponding behavior was discussed and attributed to the doping profile established in graphene by the applied metallic electrodes and to the generation of hot carriers in graphene upon the illumination by incident light. The best combination of the device and corresponding wiring configuration for light detection was the graphene photodetector with gold nanorods on its surface in the configuration, where the gold electrode was grounded and the bias voltage was applied to the aluminum electrode. In this situation, the device showed a linear behavior of photoresponse in dependence on the applied bias voltage. Nevertheless, a negligible generated photocurrent was found for both devices in every wiring configuration when zero bias was applied.

The reported photoresponse enhancement due to the presence of gold nanorods is caused by the energy redistribution from the nanoparticle localized plasmon into the graphene. However, the exact responsible mechanism is not fully known and in literature there are two possible energy redistribution channels discussed: the dielectric interaction between plasmonic nanoparticles and underlying graphene and the generation of hot electrons by plasmonic particle and their subsequent injection into

graphene. The further research of this thesis then fully focused on the determination of energy transfer channels acting in the system.

These experiments were done using the white-light scattering spectroscopy of single particles monitoring the linewidth of nanorod longitudinal localized plasmon. First the gold nanorods placed on epitaxial graphene on silicon carbide were probed. However, the unexpected behavior of the gold nanorod plasmonic peak on silicon carbide was found, when the plasmon linewidth was bigger for nanorods on SiC compared to the epitaxial graphene. This unpredictable performance thus disallowed us to determine the plasmon damping channels using the epitaxial graphene grown on silicon carbide.

Therefore, these experiments were performed using the exfoliated graphene on the glass (BK7) substrate and the gold nanorod plasmon linewidth was measured as a function of the number of underlaying graphene layers. The measurements were done for two different gold nanorod types. The obtained results showed extraordinarily big particle plasmon broadening for one underlaying graphene layer compared to the bare glass substrate for both nanorod types. Considering the almost negligible thickness of graphene, such a huge reported plasmon broadening can not be caused only by the classical dielectric coupling plasmon damping channel. These results thus suggested the presence of a novel plasmon damping channel in the system attributed to the injection of hot electrons from the gold nanorod into the underlaying graphene.

By increasing the number of underlaying graphene layers in the system the plasmon peak was further broadened, but not in such a big magnitude per layer as in the case of one graphene layer. This thus suggests also the presence of dielectric interaction. The found effects were more significant for the smaller nanorods compared to the bigger ones. Moreover, in the case of bigger gold nanorods another peak in nanorod spectra attributed to the trasversal band of gold nanorods was found. This peak was not affected by the presence of graphene / graphite layers.

The reported dependence of the longitudinal plasmon linewidth on the number of underlaying graphene layers thus suggests the contribution of both possible damping channels in the gold nanorod / graphene system, the dielectric coupling between a gold nanorod and graphene and the hot electron injection from this nanoparticle into graphene. However, to directly distinguish between these two effects, the further experiments need to be performed in the future research.

## **Suggestions for future research**

The experiment suggested for distinguishing between electromagnetic coupling and hot electrons injection channels deals with inserting an insulating spacing layer be-

tween the gold nanorod and the graphene. Then the gold nanorod scattering spectras will be recorded again as a function of the number of underlaying graphene layers in this new type of sample. The spacing layer should suppress the potential injection of hot carriers generated by the nanorod into graphene and thus quench of the conductive coupling channel. Nevertheless, the deposition of such a layer onto a graphene substrate would give a surface with an inhomogeneous thickness. Therefore, a different approach will be applied to overcome this imperfection: the gold nanorods will be directly covered by a 5 nm thick insulating silica capping layer.

In addition, the unexpected optical response of silicon carbide and epitaxial graphene on SiC discussed in section 5.3 should be further investigated. First, the complex refractive index of silicon carbide should be measured using the spectroscopic ellipsometry. Based on this data the reported big broadening of the plasmonic peak of gold nanorods on SiC could be explained or a next experiment could be suggested.

The graphene photodetector performance reported in Chapter 4 should be further studied to prove the suggested explanation and to improve the properties of the fabricated devices. This could be done by performing thorough wavelength dependent I-V measurements of their photoresponse, and by determining the doping profiles in the devices.

## BIBLIOGRAPHY

- [1] R. Peierls, “Quelques propriétés typiques des corps solides,” *Annales de l’institut Henri Poincaré*, vol. 5, no. 3, pp. 177–222, 1935.
- [2] L. D. Landau and R. G., “Absorption of sound in solids,” *Phys. Z. Sowjetunion*, no. 11, pp. 177–222, 1937.
- [3] P. R. Wallace, “The band theory of graphite,” *Physical Reviews*, vol. 71, pp. 622–634, May 1947.
- [4] K. S. Novoselov, A. K. Geim, S. V. Morozov, D. Jiang, Y. Zhang, S. V. Dubonos, I. V. Grigorieva, and A. A. Firsov, “Electric field effect in atomically thin carbon films,” *Science*, vol. 306, no. 5696, pp. 666–669, 2004.
- [5] K. S. Novoselov, D. Jiang, F. Schedin, T. J. Booth, V. V. Khotkevich, S. V. Morozov, and A. K. Geim, “Two-dimensional atomic crystals,” *Proceedings of the National Academy of Sciences of the United States of America*, vol. 102, no. 30, pp. 10451–10453, 2005.
- [6] K. S. Novoselov, A. K. Geim, S. V. Morozov, D. Jiang, M. I. Katsnelson, I. V. Grigorieva, S. V. Dubonos, and A. A. Firsov, “Two-dimensional gas of massless dirac fermions in graphene,” *Nature*, vol. 438, no. 7065, pp. 197–200, 2005.
- [7] J. C. Meyer, A. K. Geim, M. I. Katsnelson, K. S. Novoselov, T. J. Booth, and S. Roth, “The structure of suspended graphene sheets,” *Nature*, vol. 446, no. 7131, pp. 60–63, 2007.
- [8] I. W. Frank, D. M. Tanenbaum, A. M. van der Zande, and P. L. McEuen, “Mechanical properties of suspended graphene sheets,” *Journal of Vacuum Science and Technology B*, vol. 25, no. 6, pp. 2558–2561, 2007.
- [9] A. H. Castro Neto, F. Guinea, N. M. R. Peres, K. S. Novoselov, and A. K. Geim, “The electronic properties of graphene,” *Rev. Mod. Phys.*, vol. 81, pp. 109–162, Jan 2009.
- [10] A. N. Grigorenko, M. Polini, and K. S. Novoselov, “Graphene plasmonics,” *Nature photonics*, vol. 6, no. 11, pp. 749–758, 2012.
- [11] F. Bonaccorso, Z. Sun, T. Hasan, and A. C. Ferrari, “Graphene photonics and optoelectronics,” *Nature photonics*, vol. 4, no. 9, pp. 611–622, 2010.

- [12] L. Pauling, “The nature of the chemical bond and the structure of molecules and crystals: an introduction to modern structural chemistry,” in *Chapter 7* (Ithaca, ed.), vol. 18, ch. 7, p. 234–235, Cornell University Press, 1960.
- [13] T. Mueller, F. Xia, M. Freitag, J. Tsang, and P. Avouris, “Role of contacts in graphene transistors: A scanning photocurrent study,” *Phys. Rev. B*, vol. 79, p. 245430, Jun 2009.
- [14] F. Xia, T. Mueller, R. Golizadeh-Mojarad, M. Freitag, Y.-m. Lin, J. Tsang, V. Perebeinos, and P. Avouris, “Photocurrent imaging and efficient photon detection in a graphene transistor,” *Nano Letters*, vol. 9, no. 3, pp. 1039–1044, 2009. PMID: 19203207.
- [15] H. Liu, Y. Liu, and D. Zhu, “Chemical doping of graphene,” *J. Mater. Chem.*, vol. 21, pp. 3335–3345, 2011.
- [16] T. O. Wehling, K. S. Novoselov, S. V. Morozov, E. E. Vdovin, M. I. Katsnelson, A. K. Geim, and A. I. Lichtenstein, “Molecular doping of graphene,” *Nano Letters*, vol. 8, no. 1, pp. 173–177, 2008. PMID: 18085811.
- [17] J.-H. Chen, C. Jang, S. Xiao, M. Ishigami, and M. S. Fuhrer, “Intrinsic and extrinsic performance limits of graphene devices on  $\text{SiO}_2$ ,” *Nature nanotechnology*, vol. 3, no. 4, pp. 206–209, 2008.
- [18] L. Liao, Y.-C. Lin, M. Bao, R. Cheng, J. Bai, Y. Liu, Y. Qu, K. L. Wang, Y. Huang, and X. Duan, “High-speed graphene transistors with a self-aligned nanowire gate,” *Nature*, vol. 467, no. 7313, pp. 305–308, 2010.
- [19] R. R. Nair, P. Blake, A. N. Grigorenko, K. S. Novoselov, T. J. Booth, T. Stauber, N. M. R. Peres, and A. K. Geim, “Fine structure constant defines visual transparency of graphene,” *Science*, vol. 320, no. 5881, pp. 1308–1308, 2008.
- [20] K. F. Mak, M. Y. Sfeir, Y. Wu, C. H. Lui, J. A. Misewich, and T. F. Heinz, “Measurement of the optical conductivity of graphene,” *Phys. Rev. Lett.*, vol. 101, p. 196405, Nov 2008.
- [21] S.-E. Zhu, S. Yuan, and G. C. A. M. Janssen, “Optical transmittance of multilayer graphene,” *EPL (Europhysics Letters)*, vol. 108, no. 1, p. 17007, 2014.
- [22] J. W. Weber, V. E. Calado, and M. C. M. Van de Sanden, “Optical constants of graphene measured by spectroscopic ellipsometry,” *Applied Physics Letters*, vol. 97, no. 9, pp. 091904–091904, 2010.

- [23] T. Winzer, A. Knorr, and E. Malic, “Carrier multiplication in graphene,” *Nano Letters*, vol. 10, no. 12, pp. 4839–4843, 2010. PMID: 21053963.
- [24] N. M. Gabor, J. C. W. Song, Q. Ma, N. L. Nair, T. Taychatanapat, K. Watanabe, T. Taniguchi, L. S. Levitov, and P. Jarillo-Herrero, “Hot carrier-assisted intrinsic photoresponse in graphene,” *Science*, vol. 334, no. 6056, pp. 648–652, 2011.
- [25] J. C. W. Song, M. S. Rudner, C. M. Marcus, and L. S. Levitov, “Hot carrier transport and photocurrent response in graphene,” *Nano Letters*, vol. 11, no. 11, pp. 4688–4692, 2011. PMID: 21936568.
- [26] K. J. Tielrooij, J. C. W. Song, S. A. Jensen, A. Centeno, A. Pesquera, A. Z. Elorza, M. Bonn, L. S. Levitov, and F. H. L. Koppens, “Photoexcitation cascade and multiple hot-carrier generation in graphene,” *Nature Physics*, vol. 9, no. 4, pp. 248–252, 2013.
- [27] T. Winzer and E. Mali, “Impact of auger processes on carrier dynamics in graphene,” *Phys. Rev. B*, vol. 85, p. 241404, Jun 2012.
- [28] A. Tomadin, D. Brida, G. Cerullo, A. C. Ferrari, and M. Polini, “Nonequilibrium dynamics of photoexcited electrons in graphene: Collinear scattering, auger processes, and the impact of screening,” *Phys. Rev. B*, vol. 88, p. 035430, Jul 2013.
- [29] R. Bistritzer and A. H. MacDonald, “Electronic cooling in graphene,” *Phys. Rev. Lett.*, vol. 102, p. 206410, May 2009.
- [30] P. A. George, J. Strait, J. Dawlaty, S. Shivaraman, M. Chandrashekar, F. Rana, and M. G. Spencer, “Ultrafast optical-pump terahertz-probe spectroscopy of the carrier relaxation and recombination dynamics in epitaxial graphene,” *Nano Letters*, vol. 8, no. 12, pp. 4248–4251, 2008. PMID: 18989983.
- [31] H. Wang, J. H. Strait, P. A. George, S. Shivaraman, V. B. Shields, M. Chandrashekar, J. Hwang, F. Rana, M. G. Spencer, C. S. Ruiz-Vargas, and J. Park, “Ultrafast relaxation dynamics of hot optical phonons in graphene,” *Applied Physics Letters*, vol. 96, no. 8, p. 081917, 2010.
- [32] S. Winnerl, M. Orlita, P. Plochocka, P. Kossacki, M. Potemski, T. Winzer, E. Malic, A. Knorr, M. Sprinkle, C. Berger, W. A. de Heer, H. Schneider, and M. Helm, “Carrier relaxation in epitaxial graphene photoexcited near the dirac point,” *Phys. Rev. Lett.*, vol. 107, p. 237401, Nov 2011.

- [33] T. Li, L. Luo, M. Hupalo, J. Zhang, M. C. Tringides, J. Schmalian, and J. Wang, “Femtosecond population inversion and stimulated emission of dense dirac fermions in graphene,” *Phys. Rev. Lett.*, vol. 108, p. 167401, Apr 2012.
- [34] S. Winnerl, F. Gottfert, M. Mittendorff, H. Schneider, M. Helm, T. Winzer, E. Malic, A. Knorr, M. Orlita, M. Potemski, M. Sprinkle, C. Berger, and W. A. de Heer, “Time-resolved spectroscopy on epitaxial graphene in the infrared spectral range: relaxation dynamics and saturation behavior,” *Journal of Physics: Condensed Matter*, vol. 25, no. 5, p. 054202, 2013.
- [35] G. Giovannetti, P. A. Khomyakov, G. Brocks, V. M. Karpan, J. van den Brink, and P. J. Kelly, “Doping graphene with metal contacts,” *Phys. Rev. Lett.*, vol. 101, p. 026803, Jul 2008.
- [36] P. A. Khomyakov, G. Giovannetti, P. C. Rusu, G. Brocks, J. van den Brink, and P. J. Kelly, “First-principles study of the interaction and charge transfer between graphene and metals,” *Phys. Rev. B*, vol. 79, p. 195425, May 2009.
- [37] E. J. Lee, K. Balasubramanian, R. T. Weitz, M. Burghard, and K. Kern, “Contact and edge effects in graphene devices,” *Nature nanotechnology*, vol. 3, no. 8, pp. 486–490, 2008.
- [38] J. Park, Y. H. Ahn, and C. Ruiz-Vargas, “Imaging of photocurrent generation and collection in single-layer graphene,” *Nano Letters*, vol. 9, no. 5, pp. 1742–1746, 2009. PMID: 19326919.
- [39] E. C. Peters, E. J. H. Lee, M. Burghard, and K. Kern, “Gate dependent photocurrents at a graphene p-n junction,” *Applied Physics Letters*, vol. 97, no. 19, p. 193102, 2010.
- [40] T. J. Echtermeyer, P. S. Nene, M. Trushin, R. V. Gorbachev, A. L. Eiden, S. Milana, Z. Sun, J. Schliemann, E. Lidorikis, K. S. Novoselov, and A. C. Ferrari, “Photothermoelectric and photoelectric contributions to light detection in metal–graphene–metal photodetectors,” *Nano Letters*, vol. 14, no. 7, pp. 3733–3742, 2014. PMID: 24884339.
- [41] D. Sun, G. Aivazian, A. M. Jones, J. S. Ross, W. Yao, D. Cobden, and X. Xu, “Ultrafast hot-carrier-dominated photocurrent in graphene,” *Nature nanotechnology*, vol. 7, no. 2, pp. 114–118, 2012.
- [42] X. Xu, N. M. Gabor, J. S. Alden, A. M. van der Zande, and P. L. McEuen, “Photo-thermoelectric effect at a graphene interface junction,” *Nano Letters*, vol. 10, no. 2, pp. 562–566, 2010. PMID: 20038087.

- [43] M. C. Lemme, F. H. L. Koppens, A. L. Falk, M. S. Rudner, H. Park, L. S. Levitov, and C. M. Marcus, “Gate-activated photoresponse in a graphene p–n junction,” *Nano Letters*, vol. 11, no. 10, pp. 4134–4137, 2011. PMID: 21879753.
- [44] S.-F. Shi, T.-T. Tang, B. Zeng, L. Ju, Q. Zhou, A. Zettl, and F. Wang, “Controlling graphene ultrafast hot carrier response from metal-like to semiconductor-like by electrostatic gating,” *Nano Letters*, vol. 14, no. 3, pp. 1578–1582, 2014. PMID: 24564302.
- [45] Q. Ma, N. M. Gabor, T. I. Andersen, N. L. Nair, K. Watanabe, T. Taniguchi, and P. Jarillo-Herrero, “Competing channels for hot-electron cooling in graphene,” *Phys. Rev. Lett.*, vol. 112, p. 247401, Jun 2014.
- [46] M. Cutler and N. F. Mott, “Observation of anderson localization in an electron gas,” *Phys. Rev.*, vol. 181, pp. 1336–1340, May 1969.
- [47] Y. M. Zuev, W. Chang, and P. Kim, “Thermoelectric and magnetothermoelectric transport measurements of graphene,” *Phys. Rev. Lett.*, vol. 102, p. 096807, Mar 2009.
- [48] M. Faraday, “The bakerian lecture: Experimental relations of gold (and other metals) to light,” *Philosophical Transactions of the Royal Society of London*, vol. 147, pp. 145–181, 1857.
- [49] P. Drude, “Zur elektronentheorie der metalle,” *Annalen der Physik*, vol. 306, no. 3, pp. 566–613, 1900.
- [50] C. Kittel, *Introduction to solid state physics*, vol. 5. Wiley New York, 1976.
- [51] C. F. Bohren and D. R. Huffman, *Absorption and scattering of light by small particles*. New York USA: John Wiley & Sons Inc., 2008.
- [52] S. A. Maier, *Plasmonics: fundamentals and applications: fundamentals and applications*. Springer Science & Business Media, 2007.
- [53] C. Sönnichsen, T. Franzl, T. Wilk, G. von Plessen, J. Feldmann, O. Wilson, and P. Mulvaney, “Drastic reduction of plasmon damping in gold nanorods,” *Physical Review Letters*, vol. 88, no. 7, pp. 077402–077402, 2002.
- [54] P. B. Johnson and R. W. Christy, “Optical constants of the noble metals,” *Phys. Rev. B*, vol. 6, pp. 4370–4379, Dec 1972.
- [55] C. Novo, D. Gomez, J. Perez-Juste, Z. Zhang, H. Petrova, M. Reismann, P. Mulvaney, and G. V. Hartland, “Contributions from radiation damping

- and surface scattering to the linewidth of the longitudinal plasmon band of gold nanorods: a single particle study,” *Phys. Chem. Chem. Phys.*, vol. 8, pp. 3540–3546, 2006.
- [56] S. Berciaud, L. Cognet, P. Tamarat, and B. Lounis, “Observation of intrinsic size effects in the optical response of individual gold nanoparticles,” *Nano Letters*, vol. 5, no. 3, pp. 515–518, 2005. PMID: 15755105.
- [57] E. A. Coronado and G. C. Schatz, “Surface plasmon broadening for arbitrary shape nanoparticles: A geometrical probability approach,” *The Journal of Chemical Physics*, vol. 119, no. 7, pp. 3926–3934, 2003.
- [58] P. Zijlstra and M. Orrit, “Single metal nanoparticles: optical detection, spectroscopy and applications,” *Reports on Progress in Physics*, vol. 74, no. 10, p. 106401, 2011.
- [59] M. Vollmer and U. Kreibig, “Optical properties of metal clusters,” *Springer Ser. Mat. Sci.*, vol. 25, 1995.
- [60] G. Mie, “Beiträge zur optik trüber medien, speziell kolloidaler metallösungen,” *Annalen der Physik*, vol. 330, no. 3, pp. 377–445, 1908.
- [61] H. Chen, L. Shao, Q. Li, and J. Wang, “Gold nanorods and their plasmonic properties,” *Chem. Soc. Rev.*, vol. 42, pp. 2679–2724, 2013.
- [62] H. Wei, A. Reyes-Coronado, P. Nordlander, J. Aizpurua, and H. Xu, “Multipolar plasmon resonances in individual ag nanorice,” *ACS Nano*, vol. 4, no. 5, pp. 2649–2654, 2010. PMID: 20397629.
- [63] W. Ni, X. Kou, Z. Yang, and J. Wang, “Tailoring longitudinal surface plasmon wavelengths, scattering and absorption cross sections of gold nanorods,” *ACS Nano*, vol. 2, no. 4, pp. 677–686, 2008.
- [64] J. Zuloaga, E. Prodan, and P. Nordlander, “Quantum plasmonics: Optical properties and tunability of metallic nanorods,” *ACS Nano*, vol. 4, no. 9, pp. 5269–5276, 2010. PMID: 20698558.
- [65] P. Zijlstra, P. M. Paulo, and M. Orrit, “Optical detection of single non-absorbing molecules using the surface plasmon resonance of a gold nanorod,” *Nature nanotechnology*, vol. 7, no. 6, pp. 379–382, 2012.
- [66] “Lumerical solutions [online], fdtd solutions reference guide,” Accessed: 2015-05-26.

- [67] K. S. Kunz and R. J. Luebbers, *The Finite Difference Time Domain Method for Electrodynamics*. CRC Press, 1993.
- [68] J. Kim, H. Son, D. J. Cho, B. Geng, W. Regan, S. Shi, K. Kim, A. Zettl, Y.-R. Shen, and F. Wang, “Electrical control of optical plasmon resonance with graphene,” *Nano Letters*, vol. 12, no. 11, pp. 5598–5602, 2012. PMID: 23025816.
- [69] A. Hoggard, L.-Y. Wang, L. Ma, Y. Fang, G. You, J. Olson, Z. Liu, W.-S. Chang, P. M. Ajayan, and S. Link, “Using the plasmon linewidth to calculate the time and efficiency of electron transfer between gold nanorods and graphene,” *ACS Nano*, vol. 7, no. 12, pp. 11209–11217, 2013. PMID: 24266755.
- [70] J. Niu, Y. Jun Shin, Y. Lee, J.-H. Ahn, and H. Yang, “Graphene induced tunability of the surface plasmon resonance,” *Applied Physics Letters*, vol. 100, no. 6, p. 061116, 2012.
- [71] D. DeJarnette and D. K. Roper, “Electron energy loss spectroscopy of gold nanoparticles on graphene,” *Journal of Applied Physics*, vol. 116, no. 5, p. 054313, 2014.
- [72] Z. Fang, Y. Wang, Z. Liu, A. Schlather, P. M. Ajayan, F. H. L. Koppens, P. Nordlander, and N. J. Halas, “Plasmon-induced doping of graphene,” *ACS Nano*, vol. 6, no. 11, pp. 10222–10228, 2012. PMID: 22998468.
- [73] Z. Fang, Z. Liu, Y. Wang, P. M. Ajayan, P. Nordlander, and N. J. Halas, “Graphene-antenna sandwich photodetector,” *Nano Letters*, vol. 12, no. 7, pp. 3808–3813, 2012. PMID: 22703522.
- [74] M. L. Brongersma, N. J. Halas, and P. Nordlander, “Plasmon-induced hot carrier science and technology,” *Nature nanotechnology*, vol. 10, no. 1, pp. 25–34, 2015.
- [75] A. Manjavacas, J. G. Liu, V. Kulkarni, and P. Nordlander, “Plasmon-induced hot carriers in metallic nanoparticles,” *ACS Nano*, vol. 8, no. 8, pp. 7630–7638, 2014. PMID: 24960573.
- [76] M. W. Knight, H. Sobhani, P. Nordlander, and N. J. Halas, “Photodetection with active optical antennas,” *Science*, vol. 332, no. 6030, pp. 702–704, 2011.
- [77] I. Goykhman, B. Desiatov, J. Khurgin, J. Shappir, and U. Levy, “Waveguide based compact silicon schottky photodetector with enhanced responsivity in the telecom spectral band,” *Optical Express*, vol. 20, pp. 28594–28602, Dec 2012.

- [78] S. Mukherjee, F. Libisch, N. Large, O. Neumann, L. V. Brown, J. Cheng, J. B. Lassiter, E. A. Carter, P. Nordlander, and N. J. Halas, “Hot electrons do the impossible: Plasmon-induced dissociation of  $\text{H}_2$  on Au,” *Nano Letters*, vol. 13, no. 1, pp. 240–247, 2013. PMID: 23194158.
- [79] G. Konstantatos, M. Badioli, L. Gaudreau, J. Osmond, M. Bernechea, F. P. G. de Arquer, F. Gatti, and F. H. Koppens, “Hybrid graphene-quantum dot phototransistors with ultrahigh gain,” *Nature nanotechnology*, vol. 7, no. 6, pp. 363–368, 2012.
- [80] M. Quintana, K. Spyrou, M. Grzelczak, W. R. Browne, P. Rudolf, and M. Prato, “Functionalization of graphene via 1,3-dipolar cycloaddition,” *ACS Nano*, vol. 4, no. 6, pp. 3527–3533, 2010.
- [81] C. Berger, Z. Song, X. Li, X. Wu, N. Brown, C. Naud, D. Mayou, T. Li, J. Hass, A. N. Marchenkov, E. H. Conrad, P. N. First, and W. A. de Heer, “Electronic confinement and coherence in patterned epitaxial graphene,” *Science*, vol. 312, no. 5777, pp. 1191–1196, 2006.
- [82] P. Procházka, “Graphene on silicon carbide,” in *Final Report TU/e*, p. 20, Eindhoven, 2011.
- [83] M. Konečný, “Hydrogenation of graphene,” in *Final Report TU/e*, p. 23, Brno, 2013.
- [84] K. V. Emtsev, A. Bostwick, K. Horn, J. Jobst, G. L. Kellogg, L. Ley, J. L. McChesney, T. Ohta, S. A. Reshanov, J. Rohrl, *et al.*, “Towards wafer-size graphene layers by atmospheric pressure graphitization of silicon carbide,” *Nature materials*, vol. 8, no. 3, pp. 203–207, 2009.
- [85] H. Hibino, S. Tanabe, S. Mizuno, and H. Kageshima, “Growth and electronic transport properties of epitaxial graphene on SiC,” *Journal of Physics D: Applied Physics*, vol. 45, no. 15, p. 154008, 2012.
- [86] F. Varchon, R. Feng, J. Hass, X. Li, B. N. Nguyen, C. Naud, P. Mallet, J.-Y. Veuillen, C. Berger, E. H. Conrad, and L. Magaud, “Electronic structure of epitaxial graphene layers on SiC: Effect of the substrate,” *Phys. Rev. Lett.*, vol. 99, p. 126805, Sep 2007.
- [87] D. S. Lee, C. Riedl, B. Krauss, K. von Klitzing, U. Starke, and J. H. Smet, “Raman spectra of epitaxial graphene on SiC and of epitaxial graphene transferred to SiO<sub>2</sub>,” *Nano Letters*, vol. 8, no. 12, pp. 4320–4325, 2008. PMID: 18989982.

- [88] A. C. Ferrari, J. C. Meyer, V. Scardaci, C. Casiraghi, M. Lazzeri, F. Mauri, S. Piscanec, D. Jiang, K. S. Novoselov, S. Roth, and A. K. Geim, “Raman spectrum of graphene and graphene layers,” *Phys. Rev. Lett.*, vol. 97, p. 187401, Oct 2006.
- [89] P. Blake, E. W. Hill, A. H. Castro Neto, K. S. Novoselov, D. Jiang, R. Yang, T. J. Booth, and A. K. Geim, “Making graphene visible,” *Applied Physics Letters*, vol. 91, no. 6, pp. –, 2007.
- [90] Z. H. Ni, H. M. Wang, J. Kasim, H. M. Fan, T. Yu, Y. H. Wu, Y. P. Feng, and Z. X. Shen, “Graphene thickness determination using reflection and contrast spectroscopy,” *Nano Letters*, vol. 7, no. 9, pp. 2758–2763, 2007. PMID: 17655269.
- [91] A. Gupta, G. Chen, P. Joshi, S. Tadigadapa, and Eklund, “Raman scattering from high-frequency phonons in supported n-graphene layer films,” *Nano Letters*, vol. 6, no. 12, pp. 2667–2673, 2006. PMID: 17163685.
- [92] H. Min and A. H. MacDonald, “Origin of universal optical conductivity and optical stacking sequence identification in multilayer graphene,” *Phys. Rev. Lett.*, vol. 103, p. 067402, Aug 2009.
- [93] A. Gole and C. J. Murphy, “Seed-mediated synthesis of gold nanorods: role of the size and nature of the seed,” *Chemistry of Materials*, vol. 16, no. 19, pp. 3633–3640, 2004.
- [94] B. Nikoobakht and M. A. El-Sayed, “Preparation and growth mechanism of gold nanorods (nrs) using seed-mediated growth method,” *Chemistry of Materials*, vol. 15, no. 10, pp. 1957–1962, 2003.
- [95] “Nanopartz [online], the gold nanoparticle for nanotechnology,” Accessed: 2015-05-15.
- [96] “Nanoseedz [online], high quality nnaomaterial supplier,” Accessed: 2015-05-15.
- [97] P. Pramod and K. G. Thomas, “Plasmon coupling in dimers of au nanorods,” *Advanced Materials*, vol. 20, no. 22, pp. 4300–4305, 2008.
- [98] Y. Wang and L. Tang, “Chemisorption assembly of au nanorods on mercaptosilanized glass substrate for label-free nanoplasmon biochip,” *Analytica chimica acta*, vol. 796, pp. 122–129, 2013.

- [99] J. C. Love, L. A. Estroff, J. K. Kriebel, R. G. Nuzzo, and G. M. Whitesides, “Self-assembled monolayers of thiolates on metals as a form of nanotechnology,” *Chemical Reviews*, vol. 105, no. 4, pp. 1103–1170, 2005.
- [100] P. Zijlstra. Interview, April 2 2014.
- [101] L. Jiao, B. Fan, X. Xian, Z. Wu, J. Zhang, and Z. Liu, “Creation of nanostructures with poly(methyl methacrylate)-mediated nanotransfer printing,” *Journal of the American Chemical Society*, vol. 130, no. 38, pp. 12612–12613, 2008. PMID: 18763767.
- [102] Z. Cheng, Q. Zhou, C. Wang, Q. Li, C. Wang, and Y. Fang, “Toward intrinsic graphene surfaces: A systematic study on thermal annealing and wet-chemical treatment of sio<sub>2</sub>-supported graphene devices,” *Nano Letters*, vol. 11, no. 2, pp. 767–771, 2011. PMID: 21218829.
- [103] T. Mueller, F. Xia, and P. Avouris, “Graphene photodetectors for high-speed optical communications,” *Nature Photonics*, vol. 4, no. 5, pp. 297–301, 2010.
- [104] A. J. M. Giesbers, P. Procházka, and C. F. J. Flipse, “Surface phonon scattering in epitaxial graphene on 6h-sic,” *Phys. Rev. B*, vol. 87, p. 195405, May 2013.
- [105] “Schott [online], optical glass: Data sheets,” Accessed: 2015-05-20.
- [106] S. Singh, J. R. Potopowicz, L. G. Van Uitert, and S. H. Wemple, “Nonlinear optical properties of hexagonal silicon carbide,” *Applied Physics Letters*, vol. 19, no. 3, pp. 53–56, 1971.
- [107] A. B. Djurišić and E. H. Li, “Optical properties of graphite,” *Journal of Applied Physics*, vol. 85, no. 10, 1999.
- [108] H. Lin, M. F. Pantoja, L. D. Angulo, J. Alvarez, R. G. Martin, and S. G. Garcia, “FDTD modeling of graphene devices using complex conjugate dispersion material model,” *Microwave and Wireless Components Letters, IEEE*, vol. 22, pp. 612–614, Dec 2012.
- [109] R. Kovács, “Graphene based plasmonic solar cell,” in *Final Report TU/e*, p. 29, Eindhoven, 2014.
- [110] L. Břínek. Interview, November 3 2014.
- [111] F. Nelson, A. Sandin, D. B. Dougherty, D. E. Aspnes, J. E. Rowe, and A. C. Diebold, “Optical and structural characterization of epitaxial graphene on

- vicinal 6h-sic(0001)-si by spectroscopic ellipsometry, auger spectroscopy, and stm,” *Journal of Vacuum Science and Technology B*, vol. 30, no. 4, p. 04E106, 2012.
- [112] U. Starke, “Non-basal plane sic surfaces: Anisotropic structures and low-dimensional electron systems,” *Physica status solidi (b)*, vol. 246, no. 7, pp. 1569–1579, 2009.
- [113] W. G. Spitzer, D. Kleinman, and D. Walsh, “Infrared properties of hexagonal silicon carbide,” *Phys. Rev.*, vol. 113, pp. 127–132, Jan 1959.
- [114] S. Logothetidis and J. Petalas, “Dielectric function and reflectivity of 3c-silicon carbide and the component perpendicular to the c axis of 6h-silicon carbide in the energy region 1.5–9.5 ev,” *Journal of Applied Physics*, vol. 80, no. 3, pp. 1768–1772, 1996.
- [115] S. G. Sridhara, R. P. Devaty, and W. J. Choyke, “Absorption coefficient of 4h silicon carbide from 3900 to 3250 ?,” *Journal of Applied Physics*, vol. 84, no. 5, pp. 2963–2964, 1998.
- [116] B. Pégourié, “Optical properties of alpha silicon carbide,” *Astronomy and Astrophysics*, vol. 194, pp. 335–339, Apr 1988.
- [117] A. S. Bakin, “Sic homoepitaxy and heteroepitaxy,” *International Journal of High Speed Electronics and Systems*, vol. 15, no. 04, pp. 747–780, 2005.
- [118] F. Zhang, B. Sahu, H. Min, and A. H. MacDonald, “Band structure of abc-stacked graphene trilayers,” *Phys. Rev. B*, vol. 82, p. 035409, Jul 2010.

## LIST OF ABBREVIATIONS

TU/e	<i>Eindhoven University of Technology</i>
M2N	<i>Molecular Materials and Nanosystems</i>
MBx	<i>Molecular Biosensing for Medical Diagnostics</i>
LSPR	<i>Localized surface plasmon resonance</i>
FWHM	<i>Full width at half maximum</i>
FDTD	<i>Finite-difference time-domain (method)</i>
HOPG	<i>Highly oriented pyrolytic graphite</i>
BK7	<i>Borosilicate glass</i>
TEM	<i>Transmission electron microscopy</i>
CTAB	<i>Cetyltrimethylammonium bromide</i>
SAM	<i>Self-assembled monolayer</i>
MPTMS	<i>(3-mercaptopropyl)trimethoxysilane</i>
PBS	<i>Phosphate buffered saline</i>
PMMA	<i>Poly(methyl methacrylate)</i>
SEM	<i>Scanning electron microscopy</i>
AFM	<i>Atomic force microscopy</i>
EMCCD	<i>Electron multiplying charge coupled device</i>
TIR	<i>Total internal reflection</i>
NA	<i>Numerical aperture</i>
TIRM	<i>Total internal reflection microscopy</i>

# APPENDIX

## Appendix A - Sample preparation: The protocols

### Mechanical exfoliation of graphene - tips & tricks

Technically, there is no general procedure protocol to perform the exfoliation of graphene from bulk graphite to yield the highest possible number of single-layer flakes. The yield is more controlled by practice and intuition of performing scientist. But there are few rules that should be followed for sufficient graphene exfoliation.

The first peeling off is realized from bulk HOPG. Then, the peeled graphite layer present on the tape surface is weakened by few peeling-off cycles again using tape until the thickness of flakes is homogeneous all around the surface (meaning no presence of thick flakes right next to thin ones). The amount of peeling cycles is at least 6.

Later on, the transfer onto substrate by sticking the tape to the substrate and subsequent peeling of the tape is realized. This final peeling step should be proceeded as slow as possible, namely within a rate of about a millimeter per second.

However, emphasis should be also placed on a substrate and its treatment. Substrate should be cleaned properly and exhibit high adhesion. The adhesion of substrate can be enhanced by oxygen plasma or UV/ozone treatment resulting in the etching-off organic impurities from the surface and the charging of substrate surface.

For single-particle scattering microscopy experiments (Chapter 5), the transparent substrate needed to be used. Therefore, as a substrate the borosilicated glass (BK7) microscopy slides  $26 \times 76 \text{ mm}^2$  (Menzel-Gläser) were used. Prior to graphene flakes transfer onto substrate the glass slides were sonicated in acetone, isopropanol and distilled water (all for 10 minutes) and treated by UV/ozone for 1 hour. Subsequently, the graphene flakes were placed on top of glass substrate and the sample was loaded into toluene bath for 5 hours to get rid of the adhesive tape residues.

## Protocol of gold nanorods deposition using spin-coating

1. Blowing glass slides ( $22 \times 22 \text{ mm}^2$ , Menzel-Gläser) with nitrogen
2. Rinsing slides with methanol
3. Sonication of coverslips in methanol for 20 minutes
4. Unloading the glass slides from methanol, blowing them dry with nitrogen
5. UV/ozone treatment of coverslips for 90 minutes
6. Blowing slides with nitrogen
  
7. Immersion of coverslips into 5 % MPTMS solution with ethanol (high purity) for 5 minutes
8. Rinsing slides with methanol
9. Sonication of coverslips in methanol for 20 minutes
10. Unloading the glass slides from methanol and blowing them dry with nitrogen
  
11. Spin-coating of gold nanorods drop (see its content in table below) onto prepared glass coverslip
  - spin speed: 2000 rpm, 1 minute

Tab. 6.1: The content of gold nanorod solution drop of volume approximately 500  $\mu\text{l}$  for different types of used gold nanorod. Values were determined experimentally.

Gold nanorods type	Gold nanorods	Liquid
NR-10-700	5 $\mu\text{l}$	495 $\mu\text{l}$ of 0.5 mM CTAB
NR-20-700	2 $\mu\text{l}$	498 $\mu\text{l}$ of 0.5 mM CTAB
NR-40-650	5 $\mu\text{l}$	495 $\mu\text{l}$ of 0.5 mM CTAB

12. Rinsing the spin-coated glass slides with PBS and distilled water properly and blowing coverslips dry with nitrogen
  
13. *In case of single-particle scattering microscopy experiments (Chapter 5):* skip the steps 7 - 10 and apply the UV/ozone treatment of coverslips with deposited gold nanorods for 1 hour

## Protocol of gold nanorods deposition from bulk solution upon coverslip immersion

1. Blowing glass slides ( $22 \times 22 \text{ mm}^2$ , Menzel-Gläser) with nitrogen
2. Rinsing slides with methanol
3. Sonication of coverslips in methanol for 20 minutes
4. Unloading the glass slides from methanol, blowing them dry with nitrogen
5. UV/ozone treatment of coverslips for 90 minutes
6. Blowing slides with nitrogen
7. Immersion of coverslips into 5 % MPTMS solution with ethanol (high purity) for 5 minutes
8. Rinsing slides with methanol
9. Sonication of coverslips in methanol for 20 minutes
10. Unloading the glass slides from methanol and blowing them dry with nitrogen
11. Loading the slides into gold nanorods colloidal solution with CTAB concentration of  $\sim 0.1 \text{ mM}$
12. Every 20 minutes: Unloading the coverslips from gold nanorods bulk solution, rinsing them with PBS and distilled water properly, blowing them dry with nitrogen and loading them back into the nanorod bulk solution
13. If needed, after 12 rinsing steps use new gold nanorods colloidal solution
14. *In case of single-particle scattering microscopy experiments (Chapter 5):* UV/ozone treatment of coverslips with deposited gold nanorods for 1 hour

## Protocol of gold nanorods transfer onto graphene

1. Blowing the gold nanorods source glass slides with nitrogen
2. Spin-coating of PMMA onto gold nanorods glass slide
  - 120k PMMA A10, spin speed: 4000 rpm  $\sim$  330 nm
3. Heating the glass slide at 50 °C for 10 minutes
4. Cutting the glass slide with PMMA into preferable sizes
5. Blowing the prepared glass slide with nitrogen
6. Peeling-off the PMMA / gold nanorods layer in the KOH solution (concentration of 0.1 M) bath for 2 hours
  
7. *In case of single-particle scattering microscopy experiments (chapter 5):* Getting rid of the remaining CTAB molecules from gold nanorods in salt solution (NaCl - 1 M) bath for 1 hour
  
8. Cleaning of the PMMA / gold nanorods layer in the distilled water bath for 1 hour
9. Unloading the PMMA / gold nanorods layer by graphene substrate
10. Gently blowing dry with nitrogen
11. Heating the PMMA / gold nanorods / graphene sample at 50 °C for 10 minutes
12. Dissolving PMMA in acetone or chloroform bath overnight
13. Loading gold nanorods / graphene sample into isopropyl alcohol bath for 1 minute
14. Loading gold nanorods / graphene sample into distilled water bath for 1 minute
15. Blowing the sample dry with nitrogen

## Appendix B - Solar spectrum

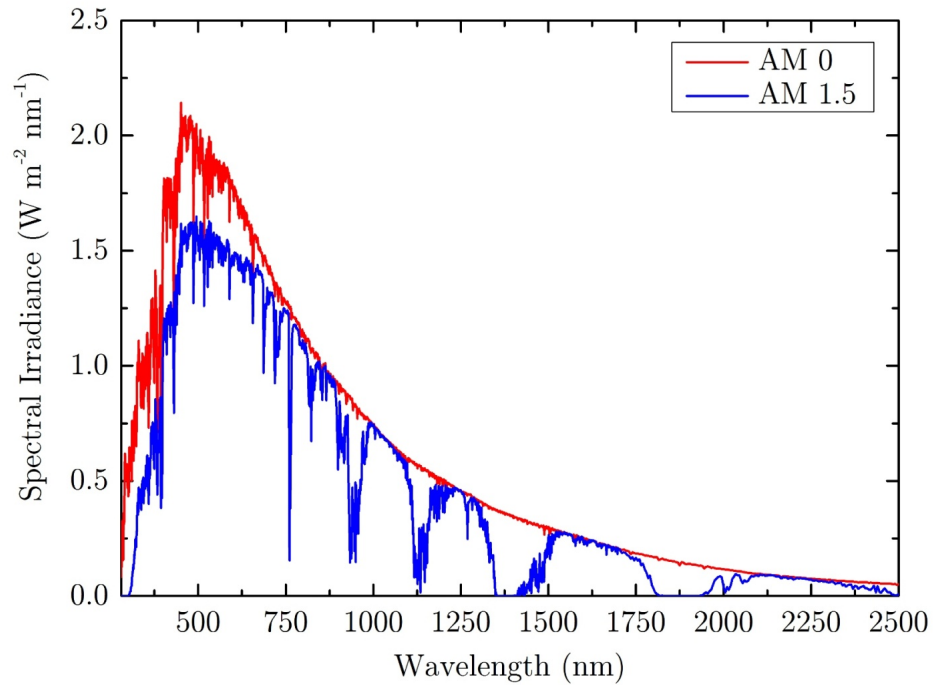


Fig. B.1: Solar irradiance spectrum: AM 0 – the solar spectrum measured in the space, AM 1.5 – the solar spectrum measured at the sea level after penetration of sunlight through the air with thickness of one and half atmosphere.

## Appendix C - The refractive index library

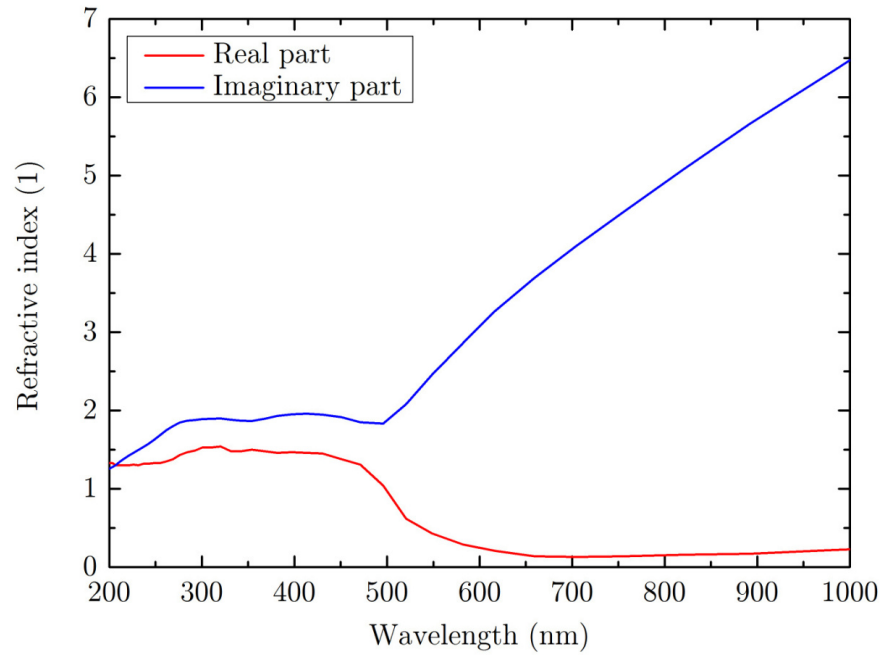


Fig. C.1: The complex refractive index of gold. Data measured by Johnson and Christy [54]. The data are depicted in the form of the dielectric function in figure 2.1.

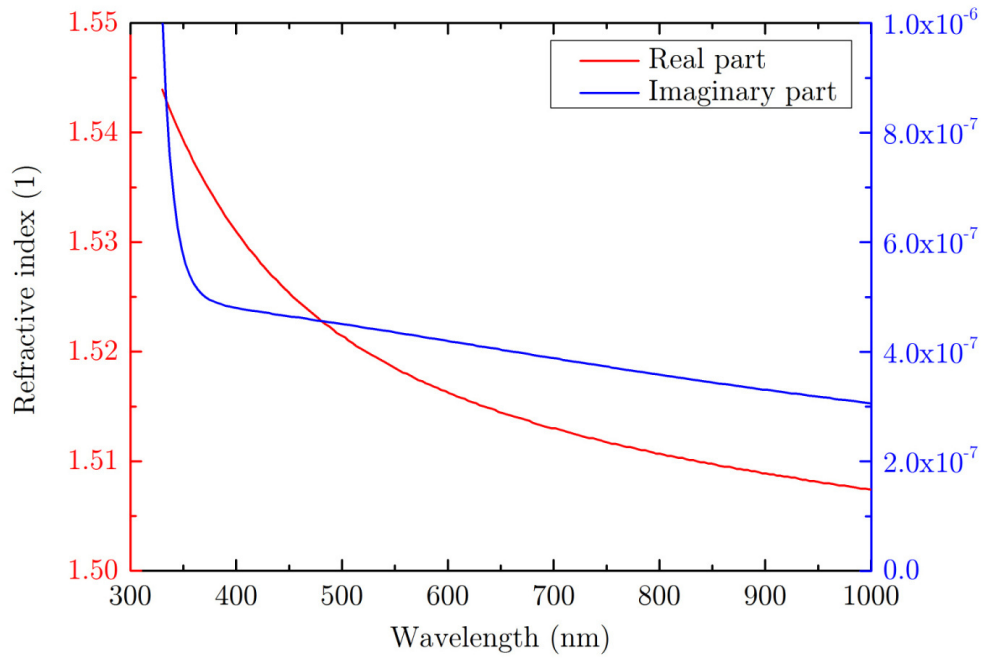


Fig. C.2: The complex refractive index of borosilicate glass (BK7). Data obtained from the company *Schott* [105].

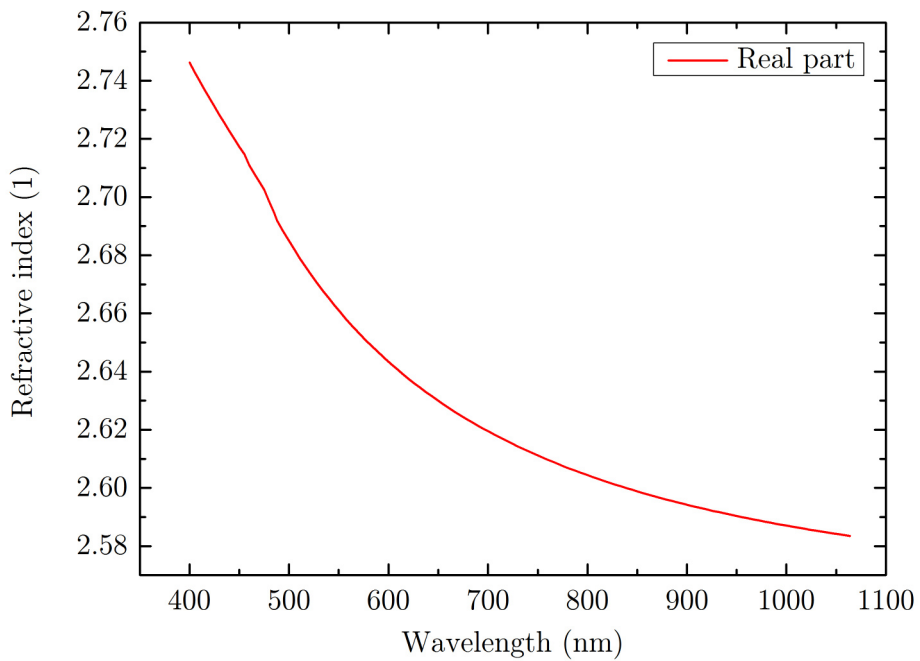


Fig. C.3: The complex refractive index of silicon carbide. Data measured by Singh *et al.* [106].

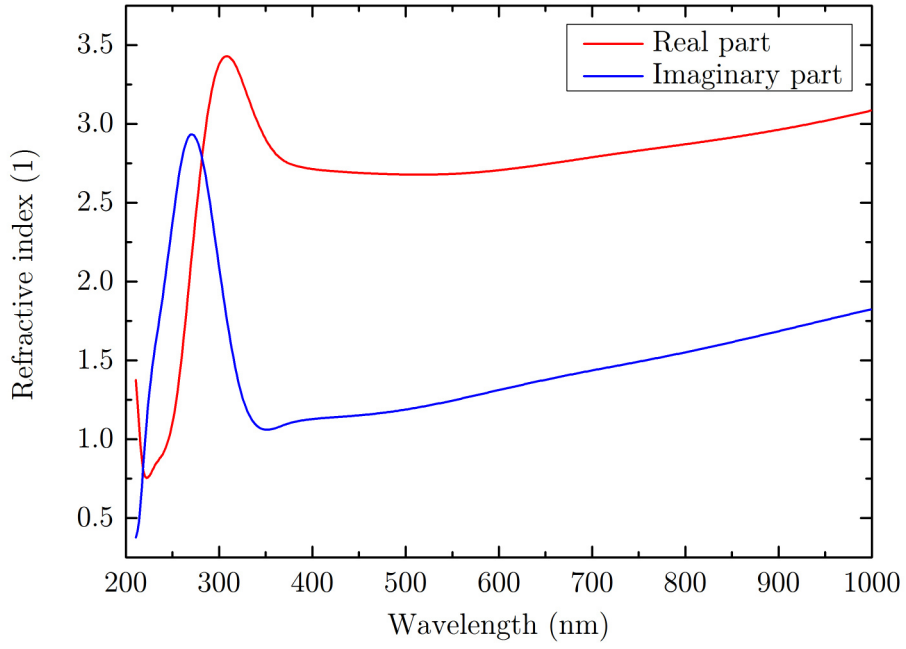


Fig. C.4: The complex refractive index of graphene. Data measured by Weber *et al.* [22]. The same plot was already used in section 1.2 as figure 1.5.

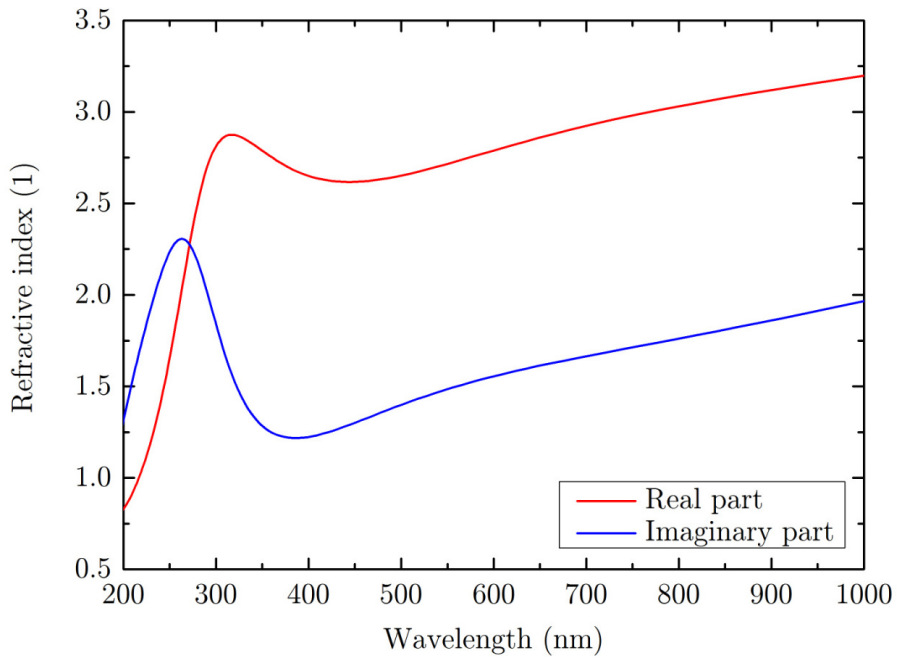


Fig. C.5: The complex refractive index of graphite. Data measured by Djurišić *et al.* [107].

## Appendix D - FDTD simulations: The computing system description

The configurations of computational systems are schematically shown in figure D.1. The gold nanorod has a shape of spherically capped cylinder. As a source of illumination the plane wave was used, represented by *total-field scattered-field source* (TFSF). This provides the illumination of the system by polarized white light pulse consisted of different wavelengths. The polarization was selected to be linear and oriented parallel to the long axis of nanorod in order to excite longitudinal LSPR of nanorod. Moreover the TFSF source enables spatially define the area to be illuminated resulting in situation that outside this defined area the incident illumination does not propagate and thus if some light leaves the area, it is the light scattered or reflected from the nanorod or substrate.

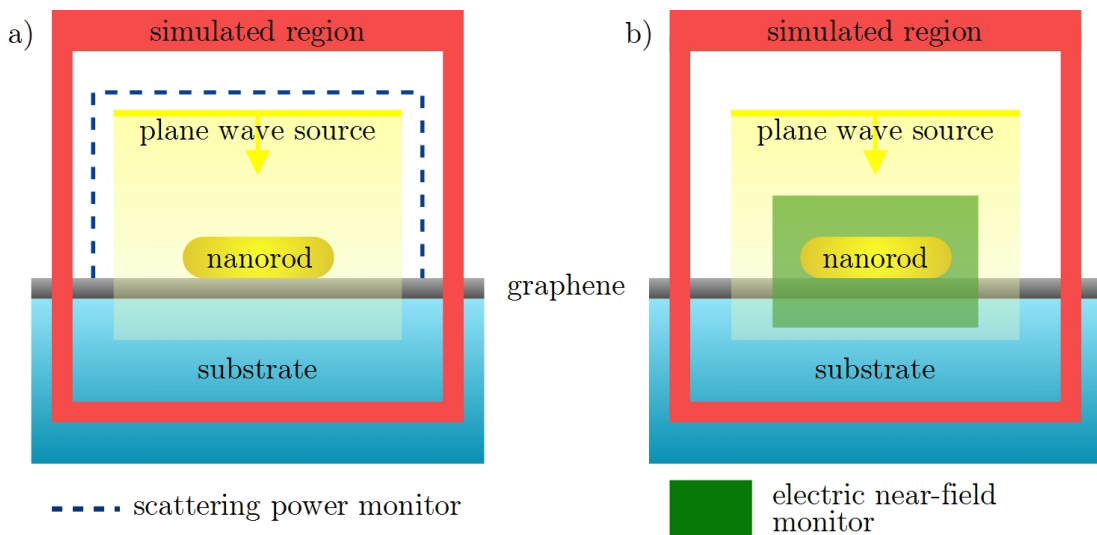


Fig. D.1: Schematic pictures of computational systems configurations (not to scale). a) The simulation system for computing of the scattering cross section of nanorod, b) the system used for nanorod electric-near fields calculations.

The calculations are carried out in whole simulated region defined by its borders, however, the data of electromagnetic field are stored only in areas where the so-called *monitors* are placed. Monitor records and then stores the electromagnetic field data in the selected wavelength range. That allows us to geometrically define the scattered light according to later performed experiments (Fig. D.1a). The scattering cross section thus corresponds to the sum of powers recorded by monitors above and around the nanoparticle divided by the intensity of the incident light. The recording of near-field enhancement in gold nanorod vicinity was then realized by placing

the power monitor at position prescribed in figure D.1b in order to visualize the penetration of electric near-field into the underlying graphene and other substrates of interest.

The boundary conditions of the simulated region are important feature for efficient calculation. Here, the *perfectly matched layers* (PML) were applied. PML are absorption boundary conditions that allowing propagation of electromagnetic waves outside the simulated region resulting in quenching of the wave and preventing its reflection back to the simulated region.